



**POLIPROPILENO MODIFICADO CON
SEMICONDUCTORES DE PLATA: COMPOSITES CON
ALTO POTENCIAL CONTRA EL SARS-CoV-2 Y OTROS
PATÓGENOS**

Lara Kelly Ribeiro da Silva

Director/a UFSCAR: Ieda Lucia Viana Rosa

Director/a UJI: Juan Andrés

Director/a UJI: Eva María Guillamón Torres

Diciembre, 2023

**POLIPROPILENO MODIFICADO CON SEMICONDUCTORES DE PLATA:
COMPOSITES CON ALTO POTENCIAL CONTRA EL SARS-CoV-2 Y OTROS
PATÓGENOS**

**Memoria presentada por Lara Kelly Ribeiro da Silva para optar al grado de
doctor/a en régimen de cotutela por la Universitat Jaume I y por la
Universidade Federal de São Carlos**



**UNIVERSITAT
JAUME·I**

Programa de Doctorado em Ciências

Escuela de Doctorado de la Universitat Jaume I

**Tese apresentada como parte dos requisitos para obtenção do título de
DOUTOR(A) EM CIÊNCIAS, área de concentração: QUÍMICA INORGÂNICA.**



Programa de Pós-graduação em Química

Juan Andrés Bort

Lara Kelly Ribeiro da Silva

Ieda Lucia Viana Rosa

Eva Maria Guillamón Torres

Castelló de la Plana, diciembre 2023.

-Licencia CC Reconocimiento - Compartir igual (BY-SA).



Financiación recibida

Agencias financiadoras del doctorando/a

Coordenação de Aperfeiçoamento de Pessoal de Nível Superior (CAPES) em
Brasil (grant n° 88887.353710/2019-00).



UNIVERSIDADE FEDERAL DE SÃO CARLOS

Centro de Ciências Exatas e de Tecnologia
Programa de Pós-Graduação em Química

Folha de Aprovação

Defesa de Tese de Doutorado da candidata Lara Kelly Ribeiro da Silva, realizada em 30/03/2023.

Defesa de Dissertação de Mestrado
Parceria de Membros de Outras Instituições

Comissão Julgadora:

Profa. Dra. Ieda Lucia Viana Rosa (UFSCar)

Prof. Dr. Elson Longo da Silva (UFSCar)

Profa. Dra. Camila Cristina de Foggi (UFRGS)

Profa. Dra. Sandra Andrea Cruz (UFSCar)

Profa. Dra. Tatiana Martelli Mazzo (UNIFESP)

O Relatório de Defesa assinado pelos membros da Comissão Julgadora encontra-se arquivado junto ao Programa de Pós-Graduação em Química.

Dedicatória

Eu dedico essa tese aos sobreviventes e aos entes queridos do caos, que foi a pandemia da COVID-19. Não há nada mais doloroso do que perder alguém que amamos, e por isso me solidarizo aos que sofreram durante a pandemia. O desenvolvimento dessa pesquisa aconteceu porque sofriamos, porque precisávamos de soluções rápidas, que nos dessem meios para acreditar que os químicos também podiam combater um vírus. Uma pena que muitas soluções só são notadas quando a humanidade sofre.

Além da saudosa dedicatória acima, eu dedico essa tese a minha mãe, Luísa Ribeiro, que “perdeu” sua filha para viver um sonho de ser pesquisadora. Sua perca não foi em vão.

Ribeiro, L. K.

“Conversa no WhatsApp”

Maria Tereza: Nunca te falei isso, mas um dia me falaram que devia ser difícil ser sua irmã. Porque você era tão extraordinária...

Mas não é difícil, porque sei o quanto dói ser extraordinária.

Lara Kelly: Então, você sofre?

Maria Tereza: Não sinto nada além de orgulho.

[...] O medo se vai quando ouço a voz do alto a me dizer: Sê valente, sê valente;
Eu posso ouvir o som, ouço a voz do alto a me dizer: Sê valente, sê valente [...]

Sê Valente
Marcos Almeida

Agradecimentos

Devo deixar registrado esse momento que escrevo essas palavras: são exatamente, dia 06 de março de 2023 às 18:35 h. Hoje é uma segunda-feira e estou no LIEC, na verdade, estou chorando na minha sala (minha sorte é que todos já foram descansar). Caro leitor, eu sou a pessoa mais fácil para chorar. Então, saiba que para cada agradecimento escrito nessa tese teci um rio de lágrimas, lembrando de tudo que vivi até aqui.

Agradeço a Deus,

eu confio em Ti, então sempre soube que, se portas se abrissem, o Senhor me faria digna de adentra-las;

Agradeço aos meus pais, Luisa Ribeiro e João Rodrigues, que me apoiaram na grande decisão de sair da minha zona de conforto e conquistar o mundo fora dos limites do meu estado natal,

Luisa e João me ajudaram no meu maior sonho que era ser doutora e, além disso, me deram todo suporte para ser doutora em uma universidade europeia, não foi fácil conseguir esse diploma. Mas como minha mãe me disse: “você vai!”; eu fui!

Agradeço a minha irmã, Maria Tereza, que é uma inspiração para mim, sempre quis melhorar por ela e me tornar uma mulher forte por ela. Obrigada por cuidar da mamãe e do tio quando eu decidi ir pra longe, espero um dia retribuir essa dedicação e esse amor;

Agradeço aos meus tios, Francisco Ribeiro e Jeane Santos, que se transformaram em meus pais. Os conselhos do meu tio e os abraços de minha tia foram o que me sustentaram longe de casa, lembro de cada abraço e cada palavra ditas até aqui;

Agradeço aos meus primos/irmãos, Andressa Ribeiro e Eduardo Ribeiro, que me amaram quando eu precisava e me acolheram em um lar de amor;

Agradeço a Amanda Fernandes Gouveia, que pra mim, é como uma irmã. Ela foi a primeira pessoa que conheci quando cheguei em São Carlos e nossos corações se encontraram, como um encontro de almas. Amanda sempre me apoiou e me ensinou na pesquisa. Quem dera eu fosse metade da pesquisadora que ela é. Minha inspiração diária. Amanda foi meu porto seguro quando mais precisei, por isso ela é minha família também;

Agradeço a Alissandra, meu afilhado Gabriel Aver e ao Américo, que é uma família que tenho apreço e carinho. A Alissandra viveu todos meus sonhos comigo, embora estivéssemos longe durante o doutorado, esse sonho foi muito aplaudido por ela, muito obrigada por tudo;

Agradeço a minha vó, Maria dos Santos, que me acompanhou durante a infância. Nunca esqueço o pesar que foi quando te disse que ia embora. Você parecia não gostar. Mas, ao invés de me desencorajar, você me disse que ia estudar (algo como a primeira série), e perguntou o que eu achava. E, ainda me disse “quero aprender, pelo menos, um pouco do que você sabe”. Estou terminado meu doutorado, vó, mas a verdade, é que não vivi o suficiente para saber mais que a senhora, talvez mesmo que viva, não sei se serei capaz de aprender, porque você veio da pobreza e a pobreza ensina demais;

Agradeço a todos meus familiares que torcem por mim, eu sou imensamente grata;

Agradeço a Roberta Yonara, uma grande amiga que a vida me entregou, e também faz parte da minha família de São Carlos. Uma pessoa que me descobriu e que me acompanhou em dias difíceis da minha vida. Obrigada por estar lá, você era pessoa certa para me acordar e me libertar;

Agradeço ao Marcelo Assis, além de um grande amigo foi um grande mentor. A verdade é que fui muito bem treinada por você. Obrigada por esses 4 anos de laboratório e vida;

Agradeço a minha família de São Carlos, Antônio Neto, Maciel Lima e Ana Gabriele. Morar com vocês é uma aventura. Foi a experiência mais completa que pude viver durante esses anos de minha vida. Obrigada por me abraçarem quando estou em uma crise de ansiedade por causa do doutorado, obrigada por me ouvirem e obrigada por me corrigirem quando cometo racismo estrutural. Vocês são responsáveis pela pessoa que estou me tornando- uma pessoa melhor;

Agradeço aos meus alunos de IC, Laura Libero, Mayra Luisa, Vitor, Giovani, Gabriel Yamakawa, Giovanna Grasser, Matheus Cipriano e Gustavo Bellucci por me deixarem experimentar o sabor que é treinar pesquisadores, e, exercer minha profissão. Vocês fazem parte da minha formação;

Agradeço aos amigos de laboratório, em especial Priscila, Katiana e Fábio Pires pela convivência e pelas boas experiências;

Agradeço aos pesquisadores e aos colaboradores do CDMF/LIEC que pude conviver nesses 4 anos. Em especial, Ricas Tranquillin, Rori Camargo, Dani Caceta e Luma Garcia.

Agradeço aos professores do CDMF/LIEC que me inspiraram durante todo meu doutorado. Em especial, Professora Dr. Lucia Helena Mascaró, Professor Dr.

Elton Sitta e Professor Dr. Elson Longo. Professor Dr. Elson Longo foi quem alimentou o sonho de viver e estudar em São Carlos. Obrigada, professor Elson, por me aceitar e me receber no LIEC;

Agradeço aos amigos que deixei na Espanha, durante meu intercâmbio, em especial, Samantha Custodio, Emerson Veiga, Jean Colombari, Marci Zanatta, María Gutiérrez, Ferran Esteves, Thaís Almeida e Victor Batista. Foi um momento de muito amadurecimento na minha vida, e, na companhia de vocês eu me tornei uma pessoa melhor;

Agradeço aos meus companheiros de “*almuerzo*” na cantina da *Universitat de Jaume I* e aos amigos de vôlei, embora eu nunca joguei vôlei. Eu torcia fervorosamente por eles, digo que ainda estou na torcida;

Agradeço ao Professor Juan Andrés e Eva Guillamon que compõem a minha orientação na *Universitat de Jaume I*, na Espanha;

Agradeço minha orientadora, Dr. Ieda Lucia Viana Rosa, que me orientou e se tornou uma pessoa que vai muito além de orientadora, uma amiga;

Agradeço a FAPESP e ao PPGQ-UFSCAR pelo apoio e financiamento da minha participação no 71º Encontro de Prêmios Nobel de Lindau. Este evento mudou minha carreira profissional;

Agradeço a CAPES pela bolsa de estudo;

Agradeço aos coautores dos trabalhos publicados pela permissão concedida para defesa da tese. Vale ressaltar que, essa tese é fruto de esforços de uma equipe de pesquisadores. Muito obrigada pela parceira;

Agradeço a você, caro leitor, que me leu até aqui. Mas, veja bem, foram inúmeras as pessoas que passaram pela minha vida e acredito que sempre levamos um pouco de cada uma dessas pessoas em nós. Essas poucas palavras que escrevi não podem e nem vão expressar toda minha gratidão. Portanto, te digo que a prova maior da minha gratidão é viver intensamente os meus dias e aproveitar cada momento com aqueles que se fazem presente.

Muito obrigada!

Lista de Tabelas

Table 3.1. Comparative results of inactivation pathogenic microbes (fungi and bacteria) in studies with polymeric materials modified with semiconductors ..	50
Table 3.2. Determination of percentage of inactivation of SARS-CoV-2 and reduction based on \log_{10} TCID ₅₀ method for 5 consecutive days.....	53
Table A.1. Experimental band gap values for the samples	83
Table B.1. Digital images for the PP, PPAW, PPAM and PPAC samples	92

Lista de Figuras

Figura 1.1. Mecanismo de adsorção da água e do oxigênio na superfície dos compósitos Ag_3PO_4 /polipropileno revelando também sua atividade anti-SARS-CoV-2 a longo prazo. Este compósito apresenta superior atividade antibacteriana (contra <i>Staphylococcus aureus</i> e <i>Escherichia coli</i>) e antifúngica (contra <i>Candida albicans</i>)	4
Figura 1.2. Semicondutores do tipo Ag_2XO_4 (X = W, Mo e Cr) encapsulados em polipropileno e testados contra microrganismos patogênicos.....	7
Figure 2.1. (A) Complex viscosity as a function of frequency; (B) storage modulus (G') and loss modulus (G'') of the samples; and cross-section SEM images of (C) PP, (D) PP/05AP, (E) PP/1AP and (F) PP/3AP.....	16
Figure 2.2. Contact angle results of pristine PP, PP/05AP, PP/1AP and PP/3AP	17
Figure 2.3. Time-kill curves for (A) <i>S. aureus</i> , (B) <i>E. coli</i> , and (C) <i>C. albicans</i> using PP, PP/05AP, PP/1AP and PP/3AP samples.....	19
Figure 2.4. Microscopic images of cell cultures incubated with viral dilutions in contact with (A) PP, (B) PP/05AP, (C) PP/1AP and (D) PP/3AP samples	21
Figure 2.5. (A) Side views of the relaxed clean Ag_3PO_4 (110) surface. The Ag cation where H_2O and O_2 adsorb is highlighted in black color; (B) side and top views of the H_2O adsorption system. O, P and Ag atoms on the surface are represented by red, violet and grey balls, respectively. For clarity, the O and H atoms of the H_2O are indicated in blue and white colors, respectively.	23
Figure 2.6. Side (A) and top (B) views of one O_2 molecule adsorbed on the Ag_3PO_4 (110) surface. O, P and Ag atoms on the surface are represented by red, violet and grey balls, respectively. For clarity, the Ag adsorption site and the water O are colored in black and blue, respectively	25
Figure 3.1. Diffractograms of the semiconductors/polypropylene. The PPAW (A), PPAM (B) and PPAC (C)	39
Figure 3.2. FTIR of the PPAW (α - Ag_2WO_4 (a); PP (b); PPAW05 (c); PPAW1 (d); PPAW3 (e)) (A), PPAM (β - Ag_2MoO_4 (a); PP (b); PPAM05 (c); PPAM1 (d); PPAM3 (e)) (B) and PPAC (Ag_2CrO_4 (a); PP (b); PPAC05 (c); PPAC1 (d); PPAC3 (e)) (C).....	41
Figure 3.4. Tensile strength, tensile modulus (MPa), strain at Break (%) and glass-transition temperature (T_g) ($^\circ\text{C}$) for (a) PPAW, (b) PPAM and (c) PPAC samples	43

- Figure 3.4.** Tensile strength, tensile modulus (MPa), strain at Break (%) and glass-transition temperature (T_g) ($^{\circ}\text{C}$) for (a) PPAW, (b) PPAM and (c) PPAC samples 45
- Figure 3.5.** Time Kill tests for *S. aureus* using the (A) PPAW, (B) PPAM and (C) PPAC composites, for *E. coli* using the (D) PPAW, (E) PPAM and (F) PPAC composites and for *C. albicans* using the (G) PPAW, (H) PPAM and (I) PPAC composites 48
- Figure 3.6.** (A) Determination of viral titer (\log_{10} TCID₅₀) after 10 minutes of contact of treated plastic film samples in relation to the positive viral control, comparing the mean of the replicates between the values arising from different exposures of the material. (B) Stability of anti-SARS-CoV-2 activity for 5 consecutive days 52
- Figure 3.7.** Mechanisms of antimicrobial action of semiconductors encapsulated in polymeric matrix (CB and VB represent the conduction band and valence band, respectively) 55
- Figure A.1.** Topological electronic density analysis of free H₂O molecule. Values of electron density (ρ) and Laplacian ($\nabla^2\rho$) in atomic units at the Bond Critical Points (BCPs) are reported. Contour lines are represented by dashed lines and gradient field by solid lines 73
- Figure A.2.** Topological electronic density analysis of the interaction between the H₂O molecule and a surface Ag atom. Values of electron density (ρ) and Laplacian ($\nabla^2\rho$) in atomic units at the Bond Critical Points (BCPs) are reported. Contour lines are represented by dashed lines and gradient field by solid lines 74
- Figure A.3.** Topological electronic density analysis of the interaction between the H₂O molecule and a surface O atom. Values of electron density (ρ) and Laplacian ($\nabla^2\rho$) in atomic units at the Bond Critical Points (BCPs) are reported. Contour lines are represented by dashed lines and gradient field by solid lines 74
- Figure A.4.** X-ray diffractograms of (A) AP, (B) PP, (C) PP/05AP, (D) PP/1AP and (E) PP/3AP samples 76
- Figure A.5.** Micro-Raman spectra of (A) AP, (B) PP, (C) PP/05AP, (D) PP/1AP and (E) PP/3AP samples 78
- Figure A.6.** FTIR spectra of (A) AP, (B) PP, (C) PP/05AP, (D) PP/1AP and (E) PP/3AP samples 79
- Figure A.7.** AFM images of the (A) PP, (B) PP/05AP, (C) PP/1AP and (D) PP/3AP films 81
- Figure A.8.** (A) Diffuse reflectance spectrum and (B) Tauc plot for the (a) AP, (b) PP, (c) PP/05AP, (d) PP/1AP and (e) PP/3AP samples considering indirect allowed transition. The arrows indicate the band gap energy 83

- Figure A.9.** Halo of inhibition tests for the microorganisms A) *S. aureus*, B) *E. coli*, and C) *C. albicans*..... 84
- Figure B.1.** Diffuse reflectance spectrum to the silver based ternary oxides, pristine PP and PP modified with (A) α -Ag₂WO₄, (B) β -Ag₂MoO₄, and (C) Ag₂CrO₄..... 86
- Figure B.2.** Tauc plot to the (A) PP, (B) PPAW, (C) PPAM, and (D) PPAC. The arrows indicate the band gap energy in the materials with indirect band gap, while the band gap for direct transitions is the linear extrapolation crossing the X axis 94
- Figure B.3.** Storage (G') and loss modulus (G'') of PPAW (A), PPAM (B) and PPAC (C) samples at 190° C as a function of frequency..... 95
- Figure B.4.** AFM images of the (A) PP and PPAW containing (B) 0.5, (C) 1.0, and (D) 3.0% wt. of the α -Ag₂WO₄ 96
- Figure B.5.** AFM images of the (A) PP and PPAM containing (B) 0.5, (C) 1.0, and (D) 3.0% wt. of the β -Ag₂MoO₄ 97
- Figure B.6.** AFM images of the (A) PP and PPAC containing (B) 0.5, (C) 1.0, and (D) 3.0% wt. of the Ag₂CrO₄ 98
- Figure B.7.** Contact angle result of PPAW, PPAM and PPAC and their oxide concentrations 0% (PP pristine), 0.5%, 1% and 3% 99

Resumo

POLIPROPILENO MODIFICADO COM SEMICONDUTORES A BASE DE PRATA: COMPÓSITOS COM ALTA POTENCIALIDADE CONTRA SARS-CoV-2 E OUTROS PATÓGENOS

O surto mundial da pandemia de coronavírus (COVID-19) e outras infecções emergentes são difíceis e às vezes impossíveis de tratar, tornando-as um dos principais problemas de saúde pública dos últimos tempos. Vale ressaltar que os semicondutores baseados em Ag podem ajudar a orquestrar várias estratégias para combater este grave problema social. Neste trabalho de tese, apresentamos a síntese de Ag_3PO_4 , $\alpha\text{-Ag}_2\text{WO}_4$, $\beta\text{-Ag}_2\text{MoO}_4$ e Ag_2CrO_4 e sua imobilização em polipropileno (PP) nas quantidades de 0,5, 1,0 e 3,0% em peso, respectivamente. Os materiais fabricados foram caracterizados por DRX, espectroscopia Raman, espectroscopia FTIR, AFM, espectroscopia UV-vis, reologia, MEV e ângulo de contato para confirmar sua integridade estrutural. A atividade dos compósitos foi investigada contra a bactéria Gram-negativa *Escherichia coli*, a bactéria Gram-positiva *Staphylococcus aureus* e o fungo *Candida albicans*. A melhor eficiência antimicrobiana foi obtida pelo compósito com $\alpha\text{-Ag}_2\text{WO}_4$, que eliminou completamente os microrganismos em até 4 h de exposição. Os compósitos foram também testados para a inibição do vírus SARS-CoV-2, mostrando eficiência antiviral superior à 98% em apenas 10 min. Além disso, foi proposto com base nos resultados dos cálculos DFT um mecanismo de reação plausível para os eventos iniciais associados à geração de ambos os radicais hidroxila $\bullet\text{OH}$ e ânion radical superóxido $\bullet\text{O}^{2-}$ na superfície mais reativa (110) do semicondutor Ag_3PO_4 . Foram avaliadas a estabilidade da atividade antimicrobiana, resultando em inibição constante, mesmo após o envelhecimento do material. A atividade antimicrobiana dos compostos foi atribuída à produção de espécies reativas de oxigênio pelos semicondutores, que podem induzir alto estresse oxidativo local, causando a morte desses microrganismos. Os compósitos semicondutores/PP provaram ser uma saída atraente para fornecer aos seres humanos um amplo espectro de atividade biocida.

Palavras-Chaves: compósitos, prata, polipropileno, biocida, SARS-CoV-2

Abstract

POLYPROPYLENE MODIFIED WITH SILVER-BASED SEMICONDUCTORS: COMPOSITES WITH HIGH POTENTIAL AGAINST SARS-CoV-2 AND OTHER PATHOGENS

The worldwide outbreak of the coronavirus (COVID-19) pandemic and other emerging infections is difficult and sometimes impossible to treat, making them one of the major public health issues of recent times. It is noteworthy that Ag-based semiconductors can help to orchestrate several strategies to combat this serious social problem. In this thesis, we present the synthesis of Ag_3PO_4 , $\alpha\text{-Ag}_2\text{WO}_4$, $\beta\text{-Ag}_2\text{MoO}_4$ and Ag_2CrO_4 and their immobilization in polypropylene in amounts of 0.5, 1.0 and 3.0% (w/w), respectively. Synthesized materials were characterized by XRD, Raman spectroscopy, FTIR spectroscopy, AFM, UV-vis spectroscopy, rheology, SEM and contact angle to confirm their structural integrity. The activity of the composites was investigated against the Gram-negative bacteria *Escherichia coli*, the Gram-positive bacteria *Staphylococcus aureus* and the fungus *Candida albicans*. The best antimicrobial efficiency was obtained by the composite with $\alpha\text{-Ag}_2\text{WO}_4$, which completely eliminated microorganisms within 4 h of exposure. The composites were also tested for inhibition of the SARS-CoV-2 virus, showing antiviral efficiency greater than 98% in just 10 min. Furthermore, based on the results of first principles calculations at the density functional level, a plausible reaction mechanism for the initial events associated with the generation of both hydroxyl radicals $\bullet\text{OH}$ and superoxide radical anion $\bullet\text{O}_2^-$ on the more reactive surface (110) of the Ag_3PO_4 semiconductor. The stability of the antimicrobial activity was evaluated, resulting in constant inhibition, even after the aging of the material. The antimicrobial activity of the compounds was attributed to the production of reactive oxygen species by semiconductors, which can induce high local oxidative stress, causing the death of these microorganisms. Ag/PP-based semiconductor composites have proven to be an attractive outlet for providing humans with a broad spectrum of biocidal activity.

Keywords: composites, silver, polypropylene, biocide, SARS-CoV-2

Resumen

POLIPROPILENO MODIFICADO CON SEMICONDUCTORES DE PLATA: COMPOSITES CON ALTO POTENCIAL CONTRA EL SARS-CoV-2 Y OTROS PATÓGENOS

El brote mundial de la pandemia de coronavirus (COVID-19) y otras infecciones emergentes son difíciles y, a veces, imposibles de tratar, lo que las convierte en uno de los principales problemas de salud pública de los últimos tiempos. Cabe señalar que los semiconductores basados en Ag pueden ayudar a orquestar varias estrategias para combatir este grave problema social. En esta tesis doctoral presentamos la síntesis de Ag_3PO_4 , $\alpha\text{-Ag}_2\text{WO}_4$, $\beta\text{-Ag}_2\text{MoO}_4$ y Ag_2CrO_4 y su inmovilización en polipropileno en cantidades de 0.5, 1.0 y 3.0% en peso, respectivamente. Los materiales fabricados se caracterizaron por XRD, espectroscopia Raman, espectroscopia FTIR, AFM, espectroscopia UV-vis, reología, SEM y ángulo de contacto para confirmar su integridad estructural. La actividad de los compuestos se investigó contra la bacteria Gram-negativa *Escherichia coli*, la bacteria Gram-positiva *Staphylococcus aureus* y el hongo *Candida albicans*. La mejor eficacia antimicrobiana se obtuvo para el composite $\alpha\text{-Ag}_2\text{WO}_4$, que eliminó por completo los microorganismos a las 4 h de exposición. Los composites también se probaron para la inhibición del virus SARS-CoV-2, mostrando una eficacia antiviral superior al 98 % en solo 10 minutos. Además, en base a los resultados de los cálculos DFT (teoría de funcional de densidad), se ha propuesto un mecanismo de reacción plausible para los eventos iniciales asociados con la generación de radicales hidroxilos $\bullet\text{OH}$ y anión radical superóxido $\bullet\text{O}_2^-$ en la superficie más reactiva (110) del semiconductor Ag_3PO_4 . Se evaluó la estabilidad de la actividad antimicrobiana, resultando en una inhibición constante, incluso después del envejecimiento del material. La actividad antimicrobiana de los compuestos se atribuyó a la producción de especies reactivas de oxígeno por parte de los semiconductores, que pueden inducir un elevado estrés oxidativo local, provocando la muerte de estos microorganismos. Los compuestos semiconductores basados en Ag/PP han demostrado ser una alternativa atractiva para proporcionar a los seres humanos un amplio espectro de actividad biocida.

Keywords: composites, plata, polipropileno, biocida, SARS-CoV-2

Sumário

1. Introdução	1
1.1. Organização Estrutural da Tese	2
1.2. Semicondutor como um material biocida	3
1.3. Polímeros como protagonista na sociedade	5
1.4. Publicações	7
1.4.1. Publicações da tese	7
1.4.2. Outras Publicações	8
1.4.3. Transferência de tecnologia	8
1.5. Referências	9
2. Bioactive Ag₃PO₄/Polypropylene Composites for Inactivation of SARS-CoV-2 and Other Important Public Health Pathogens	11
2.1. Introduction	12
2.2. Methods	14
2.3. Results and Discussion	15
2.4. Conclusions	25
2.5. References	26
3. Polypropylene modified with Ag-based semiconductors as potential material against SARS-CoV-2 and other pathogens	33
3.1. Introduction	34
3.2. Experimental section	36
3.3. Results and discussion	37
3.4. Conclusions	55
3.5. References	56
4. Conclusões	64
5. Perspectivas futuras	65
Apêndice A. Supplementary Information for “Bioactive Ag₃PO₄/Polypropylene Composites for Inactivation of SARS-CoV-2 and Other Important Public Health Pathogens”	66
A.1 Characterizations	66
A.2. Evaluation of Bactericidal and Fungicidal Activity	68
A.3. Evaluation of Antiviral Activity	69
A.4. Computational methods	71

A.5. Structural Analysis	75
A.6. References	84
Apêndice B. Supplementary Information for “Polypropylene modified with Ag-based semiconductors as potential material against SARS-CoV-2 and other pathogens”	85
B.1. Synthesis of Ag-based Semiconductors	85
B.2. Characterizations of Semiconductors/PP Composite Materials	86
B.3. Evaluation of Microbicidal Activity	87
B.4. Optical Analyses of Semiconductors/PP Composite Materials	90
B.5. References	99

Capítulo 1

Introdução

A presente tese teve como motivação uma série de intervenções para reduzir a transmissão de um vírus, o SARS-CoV-2, mundialmente conhecido. Iniciei meu doutorado em 2019, ano em que o mundo se deparou com a COVID-19. No início daquele ano, o meu projeto de pesquisa previa o desenvolvimento de materiais semicondutores com propriedades óticas que poderiam ser aplicados em sistemas biológicos, fotocatalíticos, luminescentes, e, até mesmo, catalíticos. Com a chegada da COVID-19 no Brasil, em 2020, o Laboratório Interdisciplinar de Eletroquímica e Cerâmica (LIEC), situado no Centro de Desenvolvimento de Materiais Funcionais (CDMF) financiado pela Fundação de Amparo à Pesquisa do Estado de São Paulo (FAPESP), não mediu esforços para direcionar suas pesquisas a fim de diminuir o contágio do SARS-CoV-2. Era o mínimo que poderíamos fazer para proteger nossa espécie diante da revolta que a natureza havia preparado para os anos seguintes — não sei dizer se é uma revolta, ou apenas a natureza fazendo seu papel. Diante do cenário que presenciávamos, a atitude mais viável seria direcionar os estudos dos materiais semicondutores às aplicações biocidas. O CDMF possui experiência há mais de 10 anos em materiais para aplicações biológicas. Portanto, a mudança do meu projeto de doutorado abriu uma nova linha de pesquisa, dentro do CDMF, que alinha não só a pesquisa, como também, a transferência de tecnologia para a sociedade. Vale ressaltar que os resultados das pesquisas apresentados são esforços de uma equipe formada por biólogos, químicos experimentais, químicos teóricos, físicos e engenheiros. Portanto, uma pesquisa multidisciplinar.

1.1. Organização Estrutural da Tese

Os resultados das pesquisas serão apresentados nessa tese e estão organizados de acordo com as publicações realizadas durante o doutorado. A organização estrutural dessa tese é apresentada nos parágrafos seguintes.

Capítulo 1 apresenta a fundamentação teórica e a justificativa para o desenvolvimento da tese. O Capítulo 2 aborda os primeiros resultados sobre a síntese do compósito de polipropileno com o Ag_3PO_4 e a potencialidade desse compósito sobre a inativação de bactérias, fungos e vírus. O Capítulo 3 é a continuidade dos resultados promissores obtidos no Capítulo 2, na formação de compósitos a partir de semicondutores com polipropileno. Nessa etapa, foram testados mais 3 semicondutores na produção do compósito. Os resultados apresentados neste capítulo demonstram que excelentes propriedades podem ser modeladas a partir da escolha do semicondutor. Os Apêndices A e B fornecem informações complementares aos capítulos 2 e 3, respectivamente.

O capítulo 4 apresenta as conclusões da tese e o capítulo 5 apresenta as considerações finais relacionadas aos impactos causados pelas novas investigações em aberto e novas perspectivas.

1.2. Semicondutor como um material biocida

Quando fornecido energia, os semicondutores podem conduzir eletricidade igual ou superior ao *band gap*. Nestas condições, a condutividade elétrica ocorre devido à excitação dos elétrons (e^-) da banda de valência (BV) para a banda de condução (BC). Uma vez transferidos para a BC, estes elétrons agora estão livres para se locomoverem. A remoção dos elétrons da BV resulta na formação de buracos (h^+) com carga positiva (DUTTA et al., 2014). Além dos elétrons, os buracos também podem se mover; isto ocorre quando os elétrons, vizinho ao buraco gerado, são transferidos para o buraco adjacente, gerando assim o buraco no local onde o elétron foi transferido. Este processo contribui para a formação de espécies reativas de oxigênio (EROs), com a oxidação da

H₂O e redução do O₂ (TRENCH et al., 2018). As EROs estão envolvidas em uma reação em cadeia com a formação de outros oxidantes altamente reativos, por exemplo, oxigênio singlete (¹O₂), radical hidroperoxila (\bullet O₂) ou peróxido de hidrogênio (H₂O₂) para iniciar as reações de oxidação associadas à atividade biocida.

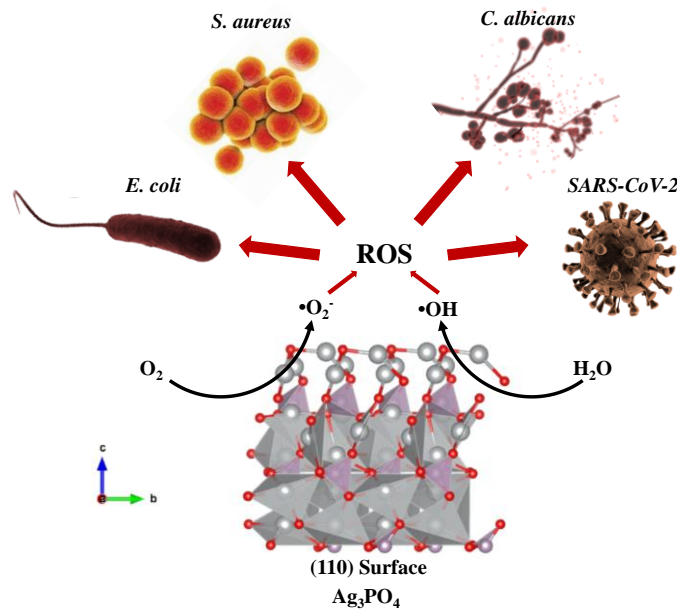
Thiyagarajan et al. (2016) sintetizou nanopartículas de Ag₃PO₄ para a aplicação na degradação de corantes orgânicos e atividade antimicrobiana. Através de microscopia de fluorescência os autores sugeriram a geração de EROs intracelular na *Escherichia coli* levando a completa inibição do patógeno após 15 minutos de tempo de incubação (THIYAGARAJAN; SINGH; BAHADUR, 2016). Em 2017 Foggi et al. (2017) testou a eficácia antimicrobiana dos microcristais de α -Ag₂WO₄ contra a bactérias resistentes à meticilina e em 2020 Foggi et al. (2020) testou a eficácia antimicrobiana dos microcristais de β -Ag₂MoO₄ também contra bactérias resistentes à meticilina. Os resultados obtidos por Foggi et al. tanto em 2017 e 2020 evidenciaram que existem uma correlação entre morfologia, energia superficial e desempenho antibacteriano (FOGGI et al., 2017; FOGGI et al., 2020). Pinatti et al. (2020) relataram uma síntese de Ag₂CrO₄ com a dopagem de zinco pela primeira vez em um método de síntese através da troca iônica da prata pelo zinco. A aplicação antimicrobiana é realizada com a bactéria *Staphylococcus aureus* e o fungo *Candida albicans*. Esses resultados confirmam que os semicondutores podem ser aplicados em sistema biocida, uma vez que, não precisa, necessariamente, de um fornecimento de energia para geração dos EROs, sendo um fenômeno que ocorre na superfície do semicondutor.

Com a chegada da pandemia de SARS-CoV-2 e a rápida disseminação do vírus, houve uma crescente necessidade de um material com a capacidade de inativar não só bactérias e fungos, mas também vírus. Nesse sentido, os semicondutores poderiam se encaixar como uma luva na aplicação relacionadas com problemas de saúde globais associados a infecções por microrganismos. Algumas vantagens podem ser citadas: processo fácil de

obtenção de variados semicondutores, boas propriedades eletrônicas, óticas, morfológicas e magnéticas únicas, que são responsáveis por sua atividade biocida aprimorada (PINATTI et al., 2020; RIBEIRO et al., 2022).

A **Figura 1.1** é o resumo gráfico dos resultados publicados no Capítulo 2, que visa entender a formação e evolução das EROs a partir da nova perspectiva dos processos de transferência de energia e carga, por meio de cálculos teóricos, para investigar a adsorção de O_2 e H_2O na superfície do semicondutor.

Figura 1.1. Mecanismo de adsorção da água e do oxigênio na superfície dos compósitos Ag_3PO_4 /polipropileno revelando também sua atividade anti-SARS-CoV-2 a longo prazo. Este compósito apresenta superior atividade antibacteriana (contra *Staphylococcus aureus* e *Escherichia coli*) e antifúngica (contra *Candida albicans*).



Fonte: RIBEIRO et al., 2021.

1.3. Polímero como protagonistas na sociedade

Os polímeros possuem alta durabilidade e são sinônimos de praticidade, essas características garantem uma via de mão dupla para as suas aplicações, pois, apresentam propriedades interessantes para comercialização, mas, podem apresentar riscos para a sustentabilidade devido à falta de legislação para reciclagem concomitante ao uso desses materiais plásticos. Um marco na utilização de plásticos, se deu a partir de 1909 com o uso de copos descartáveis com objetivo de diminuir a disseminação de doenças por conta do uso de utensílios, como xícaras, que eram comunitários. Em abril de 2020, no Brasil, as máscaras descartáveis foram utilizadas como medida de prevenção na disseminação da COVID-19. É perceptível, nessa linha do tempo, que os plásticos atuam como materiais aliados a sociedade, sendo protagonista de defesa de uma população em massa, por exemplo.

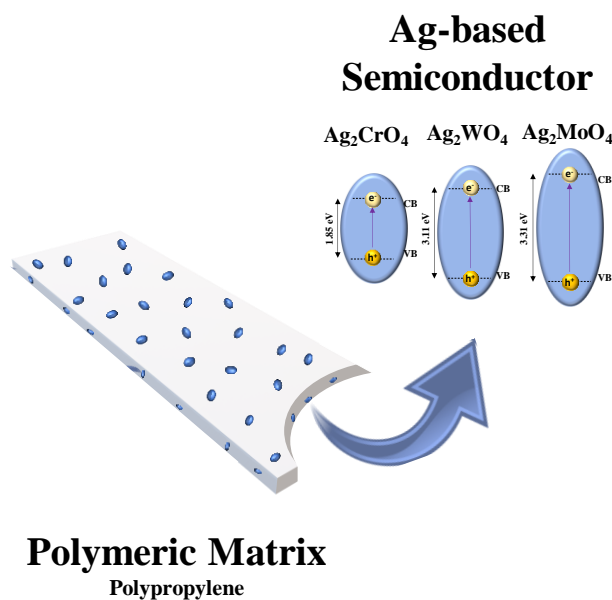
O polipropileno (PP) foi descoberto em 1954 e ganhou forte popularidade muito rapidamente devido ao fato de que PP tem a menor densidade entre os plásticos. PP tem uma excelente resistência química e pode ser processado através muitos métodos de conversão, como moldagem por injeção e extrusão. O PP é um polímero preparado cataliticamente de propileno. Como um material polimérico fundamental, o PP tem sido intensamente utilizado em muitas áreas, abrangendo automóveis, cosméticos, têxteis e embalagens de consumo devido à grande processabilidade, resistência química e barreiras de umidade. Mais de um quarto da demanda de polímeros no mundo é de polipropileno porque apresenta uma das mais baixas densidade entre os materiais plásticos que permite o processo de fabricação em peças leves. Portanto, o PP não só encontra seu uso em inúmeras aplicações por ter menor densidade entre os polímeros, mas também porque possui várias características como rigidez superior a maioria dos plásticos, boa resistência ao impacto à temperatura ambiente, elevada resistência química, entre outras características que variam de acordo com a aplicação. O PP pode ser associado ao baixo custo de produção e possibilidade de reciclagem da matéria prima, o que torna uma excelente

escolha para avaliar na aplicação contra patógenos, devido sua alta demanda na sociedade.

Em um estudo de Bustos-Torres et al., 2017 o PP foi sintetizado como matriz para o semicondutor ZnO, para formação do compósito PP/ZnO. Os autores estudaram a influencia da morfologia do nanomaterial na estrutura do compósito. Akhmedov et al., 2011 estudou a condutividade elétrica do PP no semicondutor α -Fe₂O₃ e Dong et al., 2023 estudou compósitos de dissulfeto de molibdênio com PP para melhoras as propriedades térmicas. É perceptível que a área de compósitos formados a partir de PP e semicondutores já é estudada e bem abrangente em várias aplicações, porém, não há estudos na literatura sobre melhora da atividade viral de um compósito a base de prata e PP. O PP não apresenta atividade contra patógenos conhecida, portanto, a união de um semicondutor que forneça essa característica ao polímero seria intencionalmente vantajosa. No atual cenário de infecções por SARS-CoV-2, o desafio tecnológico reside no desenvolvimento de sistemas biocidas viáveis economicamente, reutilizáveis e capazes de inativar patógenos oportunistas, reduzindo assim o risco de infecção e transmissão. Como produto desta pesquisa, propõe-se a confecção de compósito poliméricos para a produção de superfícies biocidas seguros, que podem ser aplicadas em equipamentos de proteção individual (EPI), embalagens para alimentos, tecidos, e outros dispositivos economicamente viáveis para lutar contra o aumento de pandemias virais e riscos fatais associados a vírus, bactérias e fungos.

A **Figura 1.2** é o resumo gráfico dos resultados publicados no Capítulo 3, que visa entender como se comportam outros semicondutores sobre a matriz do PP e sua estabilidade frente a degradabilidade e sua eficiência contra patógenos.

Figura 1.2. Semicondutores do tipo Ag_2XO_4 ($\text{X} = \text{W}, \text{Mo}$ e Cr) encapsulados em polipropileno e testados contra microrganismos patogênicos.



Fonte: ASSIS et al., 2022.

1.4. Publicações

1.4.1. Publicações da Tese

Ribeiro, L. K. et al. Bioactive Ag_3PO_4 /Polypropylene Composites for Inactivation of SARS-CoV-2 and Other Important Public Health Pathogens. *The Journal of Physical Chemistry B*, 2021, 125.38: 10866-10875.

Ribeiro, L. K. et al. Polypropylene Modified with Ag-Based Semiconductors as a Potential Material against SARS-CoV-2 and Other Pathogens. *ACS Applied Polymer Materials*, 2022, 4.10: 7102-7114.

1.4.2. Outras publicações

Assis, M., Gouveia, A. F., **Ribeiro, L. K.**, Ponce, M. A., Churio, M. S., Oliveira Jr, O. N., ... & Andrés, J. (2023). Towards an efficient selective oxidation of sulfides to sulfones by NiWO₄ and α -Ag₂WO₄. *Applied Catalysis A: General*, 119038.

Assis, M., Tello, A. C., Abud, F. S., Negre, P., Ribeiro, **L. K.**, **Ribeiro**, R. A., ... & Longo, E. (2022). Bridging experiment and theory: Morphology, optical, electronic, and magnetic properties of MnWO₄. *Applied Surface Science*, 600, 154081.

Gouveia, A. F., Assis, M., **Ribeiro, L. K.**, Lima, A. E. B., de Oliveira Gomes, E., Souza, D., ... & San-Miguel, M. A. (2022). Photoluminescence emissions of Ca_{1-x}WO₄: xEu³⁺: Bridging between experiment and DFT calculations. *Journal of Rare Earths*, 40(10), 1527-1534.

Ribeiro, L. K., Gouveia, A. F., Silva, F. D. C. M., Noleto, L. F., Assis, M., Batista, A. M., ... & Luz Júnior, G. E. (2022). Tug-of-War Driven by the Structure of Carboxylic Acids: Tuning the Size, Morphology, and Photocatalytic Activity of α -Ag₂WO₄. *Nanomaterials*, 12(19), 3316.

Assis, M., Simoes, L. G. P., Tremiliosi, G. C., **Ribeiro, L. K.**, Coelho, D., Minozzi, D. T., ... & Longo, E. (2021). PVC-SiO₂-Ag composite as a powerful biocide and anti-SARS-CoV-2 material. *Journal of Polymer Research*, 28(9), 361.

Assis, M., Simoes, L. G. P., Tremiliosi, G. C., Coelho, D., Minozzi, D. T., Santos, R. I., **Ribeiro, L. K.** ... & Longo, E. (2021). SiO₂-Ag composite as a highly virucidal material: a roadmap that rapidly eliminates SARS-CoV-2. *Nanomaterials*, 11(3), 638.

1.4.3. Transferência de tecnologia

L. K. Ribeiro; M. Assis; L. R. Lima; D. Coelho; M. O. Gonçalves; R. S. Paiva; L. N. Moraes; L. F. Almeida; L. H. Mascaro; R. M. T. Grotto; C. P. Sousa; I. L. V. Rosa; S. A. Cruz; J. Andrés; E. Longo, 2021, Brazil. Patent: Innovation Privilege. Registration number: BR1020210212632, Title: "POLYOLEFIN COMPOSITES AND SILVER-BASED SEMICONDUCTORS WITH HIGH BIOCIDAL ACTIVITY", Institution of registration: INPI - National Institute of Industrial Property. Deposite: 10/22/2021

1.5. Referências

AKHMEDOV, F. I. et al. A study of the electric conductivity of dielectric polypropylene (PP)-semiconductor α -(Fe₂O₃) macrosystems. **Surface Engineering and Applied Electrochemistry**, v. 47, n. 5, p. 388–389, 2011.

BUSTOS-TORRES, K. A. et al. Influence of the morphology of ZnO nanomaterials on photooxidation of polypropylene/ZnO composites. **Materials Science in Semiconductor Processing**, v. 68, p. 217–225, 2017.

DONG, H. et al. Molybdenum disulfide of modified in situ as a nanofiller for enhanced mechanical properties and thermal properties of polypropylene composites. *Polymer Composites*, v. 44, n. 2, p. 1240–1251, 21 fev. 2023.

DUTTA, D. P. et al. High Adsorption Capacity for Cationic Dye Removal and Antibacterial Properties of Sonochemically Synthesized Ag₂WO₄ Nanorods. **European Journal of Inorganic Chemistry**, v. 2014, n. 33, p. 5724–5732, nov. 2014.

FOGGI, C. C. et al. Unveiling the role of β -Ag₂MoO₄ microcrystals to the

improvement of antibacterial activity. **Materials Science and Engineering: C**, v. 111, p. 110765, 2020.

FOGGI, Camila C., et al. Synthesis and evaluation of α -Ag₂WO₄ as novel antifungal agent. **Chemical Physics Letters**, v. 674, p. 125-129, 2017.

PINATTI, I. M. et al. Zinc-substituted Ag₂CrO₄: A material with enhanced photocatalytic and biological activity. **Journal of Alloys and Compounds**, v. 835, p. 155315, 2020.

RIBEIRO, L. K. et al. Tug-of-War Driven by the Structure of Carboxylic Acids: Tuning the Size, Morphology, and Photocatalytic Activity of α -Ag₂WO₄. **Nanomaterials**, v. 12, n. 19, p. 3316, 23 set. 2022.

THIYAGARAJAN, Shankar; SINGH, Sarika; BAHADUR, D. Reusable sunlight activated photocatalyst Ag₃PO₄ and its significant antibacterial activity. **Materials Chemistry and Physics**, v. 173, p. 385-394, 2016.

TRENCH, A. B. et al. Connecting structural, optical, and electronic properties and photocatalytic activity of Ag₃PO₄:Mo complemented by DFT calculations. **Applied Catalysis B: Environmental**, v. 238, n. April, p. 198-211, 2018.

Capítulo 2

Bioactive Ag₃PO₄/Polypropylene Composites for Inactivation of SARS-CoV-2 and Other Important Public Health Pathogens

The Journal of Physical Chemistry B, 125(38), 10866-10875

Lara K. Ribeiro¹, Marcelo Assis^{1,2*}, Lais R. Lima³, Dyovani Coelho¹, Mariana O. Gonçalves⁴, Robert S. Paiva³, Leonardo N. Moraes^{5,6}, Lauana F. Almeida^{5,6}, Felipe Lipsky⁷, Miguel A. San-Miguel⁷, Lúcia H. Mascaró¹, Rejane M. T. Grotto^{5,6}, Cristina P. Sousa⁴, Ieda L. V. Rosa¹, Sandra A. Cruz³, Juan Andrés^{2*}, and Elson Longo^{1*}

¹CDMF, LIEC, Federal University of São Carlos - (UFSCar), São Carlos, SP, 13565-905 Brazil

²Department of Physical and Analytical Chemistry, University Jaume I (UJI), Castelló 12071

³Chemistry Department, Federal University of São Carlos (UFSCar), São Carlos, SP, 13565-905, Brazil.

⁴Biotechnology Graduation Program, Federal University of São Carlos (UFSCar), São Carlos, SP, 13565-905, Brazil.

⁵School of Agriculture; São Paulo State University (Unesp), Botucatu, SP, 18610-034, Brazil.

⁶Molecular Laboratory of Clinical Hospital of Botucatu, Medical School; São Paulo State University (Unesp), Botucatu, SP, 18618-687, Brazil

⁷Institute of Chemistry, State University of Campinas (Unicamp), Campinas, SP, 13083-970, Brazil.

ABSTRACT: The current unprecedented coronavirus pandemic (COVID-19) is increasingly demanding advanced materials and new technologies to protect us and inactivate the SARS-CoV-2. In this research work, we report the manufacture of Ag₃PO₄/polypropylene composites using a simple method, also revealing their long-term anti-SARS-CoV-2 activity. This composite shows superior antibacterial (against *Staphylococcus aureus* and *Escherichia coli*) and antifungal activity (against *Candida albicans*), thus having potential for a variety of technological applications. The as-manufactured materials were characterized by X-ray diffraction (XRD), Raman, Fourier transform infrared spectroscopy (FTIR), atomic force microscopy (AFM), UV-Vis, rheology, scanning electron microscopy (SEM) and contact angle to confirm their structural integrity. Based on the results of first-principles calculations at the density functional level, a plausible reaction mechanism for the initial events associated with the generation of both hydroxyl radical •OH and superoxide radical anion •O₂⁻ in the most reactive (110) surface of Ag₃PO₄ was proposed. Ag₃PO₄/polypropylene composites proved to be an attractive avenue to provide human beings with a broad spectrum of biocide activity.

KEYWORDS: Ag₃PO₄, polypropylene, biocide composites, anti-SARS-CoV-2 composite

2.1. Introduction

Currently, human beings have been facing a critical problem with the pandemic caused by the emergence of the SARS-CoV-2 virus.¹⁻³ Microorganisms (including bacteria, fungi and viruses) pose serious threats to public health. Particularly, viruses are one of the main causes of diseases worldwide, being responsible for infecting and killing a large part of the population in a given area.^{4,5} Coronaviruses, a class of viruses, are constituted

of positive single-stranded RNAs and belong to the *Coronaviridae* family.⁶ The establishment of viral tropism depends on the susceptibility and permissiveness of a particular host cell. These types of viruses usually infect animals and humans due to their incredible ability to adapt to their current host, causing respiratory problems and some flu-like symptoms.⁶⁻⁸

SARS-CoV-2 is transmitted by human body fluids and the virion can enter through nasopharyngeal and/or oropharyngeal tissues.⁹⁻¹³ Recent results have reported that these viruses can survive for several days on different surfaces.¹⁴⁻¹⁷ In view of this scenario, efforts in research, development and manufacture of materials with anti-SARS-CoV-2 activity are growing, generating potentially safe alternatives to prevent virus contamination and transmission in humans.¹⁸

Innovations often play an essential role in the acceleration of the discovery of new functional materials.¹⁹ But their success and applicability largely depend on the previous experience; our research group has been developing potent biocide materials based on complex silver-based oxides, such as Ag_2CrO_4 ,^{20,21} three polymorphs of Ag_2WO_4 ,^{22,23} Ag_3PO_4 ,^{24,25} $\alpha\text{-AgVO}_3$,²⁶ and $\alpha\text{-Ag}_2\text{MoO}_4$ ²⁷ with enhanced antifungal activity. Additionally, to provide a deeper understanding of the atomic and electronic structure and establish a correlation between the morphology and the biocide activity we conducted first-principles calculations at the density functional theory (DFT) level to complement and rationalize the experimental findings.²⁸

Silver orthophosphate, Ag_3PO_4 (AP), is an n-type semiconductor with a band gap energy value of 2.4 eV, having high quantum efficiency until 90% for O_2 evolution from H_2O splitting.²⁹⁻³⁵ Despite its high photocatalytic activities, notable drawbacks have emerged in relation to this material, i.e., it invariably displays a poor stability when forming metallic Ag ³⁶⁻⁴⁰ or dissolved in water,⁴¹ possibly leading to partial dissociation of Ag_3PO_4 into Ag^+ and PO_4^{3-} .⁴² All of these drawbacks have weakened its activity, thus reducing its broad application as a biocide agent. Very recently, Li et al.⁴³ have discussed and summarized the

progress to improve its stability and performance, as well as the barriers that should be overcome prior to practical application.

Polypropylene (PP) is a chemically and thermally stable polymer with a wide range of applications, from textile to automotive industries, and one of the most used plastics worldwide since mid-20th century.⁴⁴ PP is used as an immobilization matrix and a substrate for biocompatibility and biocide activity tests in devices of the hospital-medical field, such as masks, aprons and food trays, among other applications.^{45,46} Based on that, the strategy adopted in this work was to produce a bioactive AP/PP composite to stabilize the AP, and The inactivation of bacteria (*Staphylococcus aureus* and *Escherichia coli*), fungus (*Candida albicans*) and virus (SARS-CoV-2) have been investigated. The present composites having potential for a variety of technological applications, such as the manufacture of packaging, fabrics and protective equipment, as well as for surface treatment. The underlying technology based on this composite can be considered an innovation to protect man and avoid the contamination, transmission and proliferation of SARS-CoV-2 worldwide.

2.2. Methods

Ag₃PO₄ synthesis: Ag₃PO₄ was synthesized by the co-precipitation method in an aqueous medium. Separate solutions of NaH₂PO₄·H₂O (98%, Sigma-Aldrich) and AgNO₃ (99.8%, Cennabras) were prepared with molar ratios of 1:1, respectively. The 100 mL solution of 1 x 10⁻³ mol of NaH₂PO₄ was added to the 100 mL solution of 1 x 10⁻³ mol of AgNO₃ under constant stirring. After the addition, the suspension was kept under stirring for 20 minutes. The precipitates were washed with deionized water and centrifuged, and this process was repeated until reaching pH neutrality (\cong 7). After the washing procedure, this powder was dried at 60 °C for 10 h. The samples were labeled as AP.

Preparation of PP/AP composite: The composites were compounded using an internal mixer (Thermo Scientific – Polylab OS model) with a counter-rotating rotor connected to the Rheomix 600 OS Lab mixing chamber. The

conditions employed were a temperature of 200 °C and a rotor speed of 50 rpm for 4 min with closed and locked chamber, which operated with 70% of its capacity. The AP was added to the polymer (PP) in proportions of 0.5, 1.0, and 3.0% wt. The processing conditions, especially those concerning the thread profile and temperatures, were outlined to ensure an adequate dispersive and distributive mixture. The samples were named according to the AP content as follows: PP/05AP, PP/1AP and PP/3AP. The experimental characterizations, biological tests, and theoretical calculations are described in the Supporting Information (**Appendices A.1-A.3**).

2.3. Results and Discussion

The XRD patterns of the PP/AP composites it is possible to observe that the alpha structure of the PP was maintained, as well as the structure of the crystals of the AP, suggesting success in the formation of the PP/AP composites (see in Supporting Information, **Figure A.4**). These results corroborate with the FTIR, micro-Raman, UV-Vis and AFM analyses, showing that at long- and short-range the structure of Ag_3PO_4 is maintained within the polymeric matrix. (**Figures A.5 to A.8**). The interactions between the matrix and the AP particles, as well as their dispersion state, were evaluated by rheological measurements in the dynamic state and scanning electron microscopy (SEM) conducted on cryogenically fractured samples (see **Figure 2.1**).

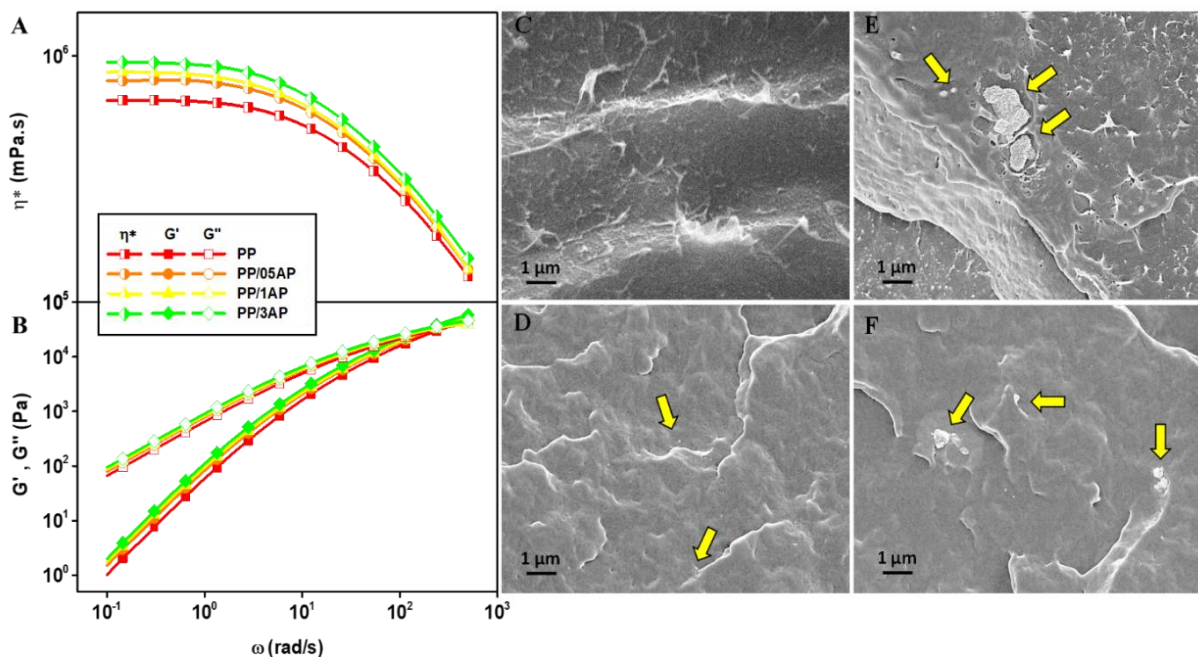


Figure 2.1. (A) Complex viscosity as a function of frequency; (B) storage modulus (G') and loss modulus (G'') of the samples; and cross-section SEM images of (C) PP, (D) PP/05AP, (E) PP/1AP and (F) PP/3AP.

PP presents a pseudoplastic flow behavior with viscosity decrease as a function of frequency. A gradual increase in the viscosity of the Newtonian plateau region can be observed with the increase of the filler content. The low-frequency region named terminal zone is in the $G' \propto \omega$ and $G'' \propto \omega^2$ regions. When the degree of dispersion increases, the powers 1 and 2 change to lower values.⁴⁷ **Figure 2.1B** presents the same inclination values, which means low dispersion between the filler and the polymer matrix since a percolation network was not observed. These results are in accordance with the SEM images (**Figures 2.1C-F**). The micrography in **Figure 2.1C** shows the cross-section of the nanocomposites, where it is possible to observe that pristine PP is a homogeneous material. As AP is added, it is possible to see the presence of spherical particles in the nanocomposites. A better dispersion is noticed for the PP/05AP sample (**Figure 1D**). As the concentration of AP increases for PP/1AP and PP/3AP samples (**Figures 1E-F**), some micron-sized agglomerates of AP are formed, corroborating the structural data.

Figure 2.2 displays the contact angle results regarding the pristine PP and PP/AP composites. The ANOVA was performed using GraphPad Prism 5.00 software. It is observed that for the PP sample this value is 86° and rises to 98, 94 and 95° for the PP/05AP, PP/1AP and PP/3AP samples. Between the samples there are statistically significant differences. Since PP is an apolar polymer with hydrophobic properties,⁴⁸ by increasing the AP semiconductor content there is a consequent increase in hydrophobicity. Kasraei et al.⁴⁹ observed the same behavior in Ag-based nanocomposites in polymeric matrices. The formation of a composite with a more hydrophobic surface may inhibit and/or decrease the activities of pathogenic microorganisms as a result of the lower interaction between the composite surface and the microorganism.^{50,51}

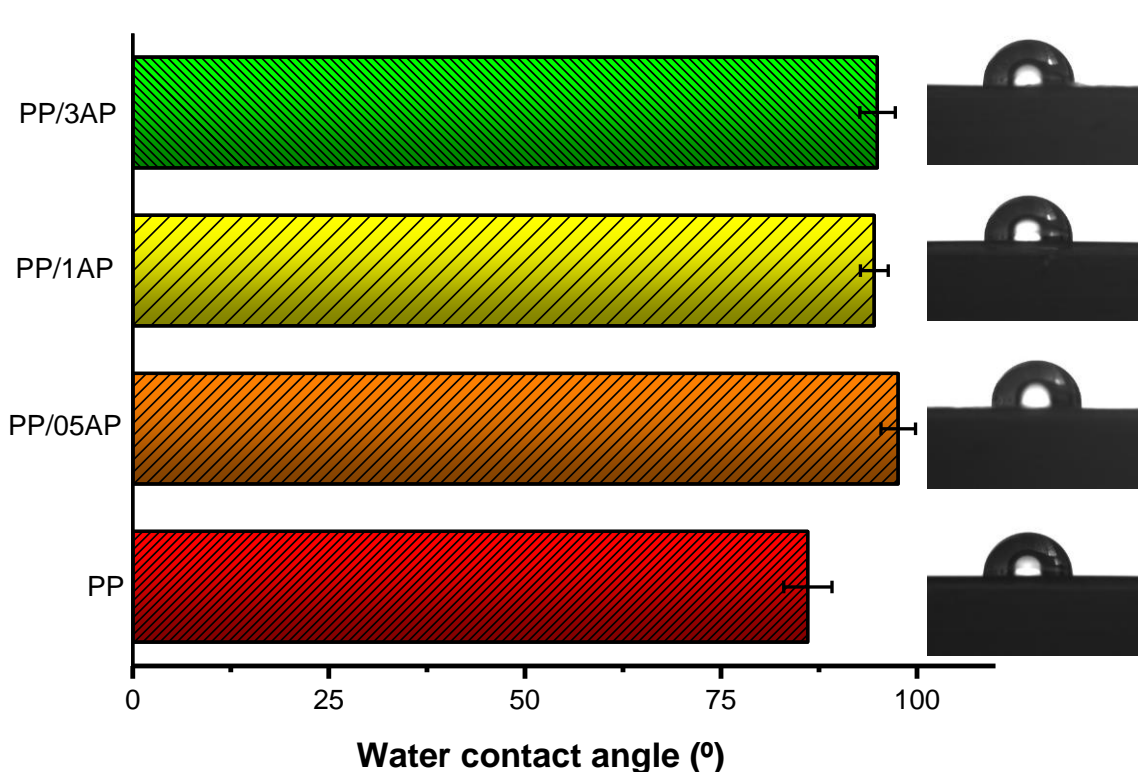


Figure 2.2. Contact angle results of pristine PP, PP/05AP, PP/1AP and PP/3AP.

Once AP was successfully incorporated into the polymeric PP matrix, contact microbicidal inhibition tests were performed. For *S. aureus* (Gram +), *E.*

coli (Gram -) and *C. albicans* (fungi). The time-kill tests (**Figure 2.3**) were carried out, following the microbicidal evolution of the obtained materials, to corroborate the halo of inhibition tests (**Figure A.9**). The analyses were performed using time variations (2, 4, 8, 16, 32, 64, 128, 256, 512, 1440 (1 day), 2880 (2 days) and 4320 min (3 days)). For *S. aureus* (**Figure 2.3A**), it was possible to note a reduction of 99.999% in CFU at the maximum time (3 days) for PP/3AP sample. In contrast, for *E. coli* (**Figure 2.3B**) there was a reduction of 99.999% at 256 min (~4.5h) for all composites. For the elimination of *C. albicans*, that is a more complex cellular constitution, the PP/3AP composite had contact elimination of 99% at the maximum time (3 days).

This difference between the elimination capacities of these tested bacteria was due to the fact that the composition of their membranes is very different, conferring greater resistance to the Gram-positive (*S. aureus*).⁵²⁻⁵⁴ The composites surfaces can interact with the main component of the bacterial cell, the peptidoglycan. Although the cell wall of bacteria is composed of peptidoglycan, Gram-negative bacteria have a much smaller amount of peptidoglycan than Gram-positive bacteria, conferring greater resistance to the Gram-positive a cell wall so dense and strong, thus preventing the particle from entering the periplasm of the bacteria⁵⁵⁻⁵⁸. For the elimination of *C. albicans*, since this fungus has a more complex cellular constitution a similar behavior to *S. aureus* was observed.

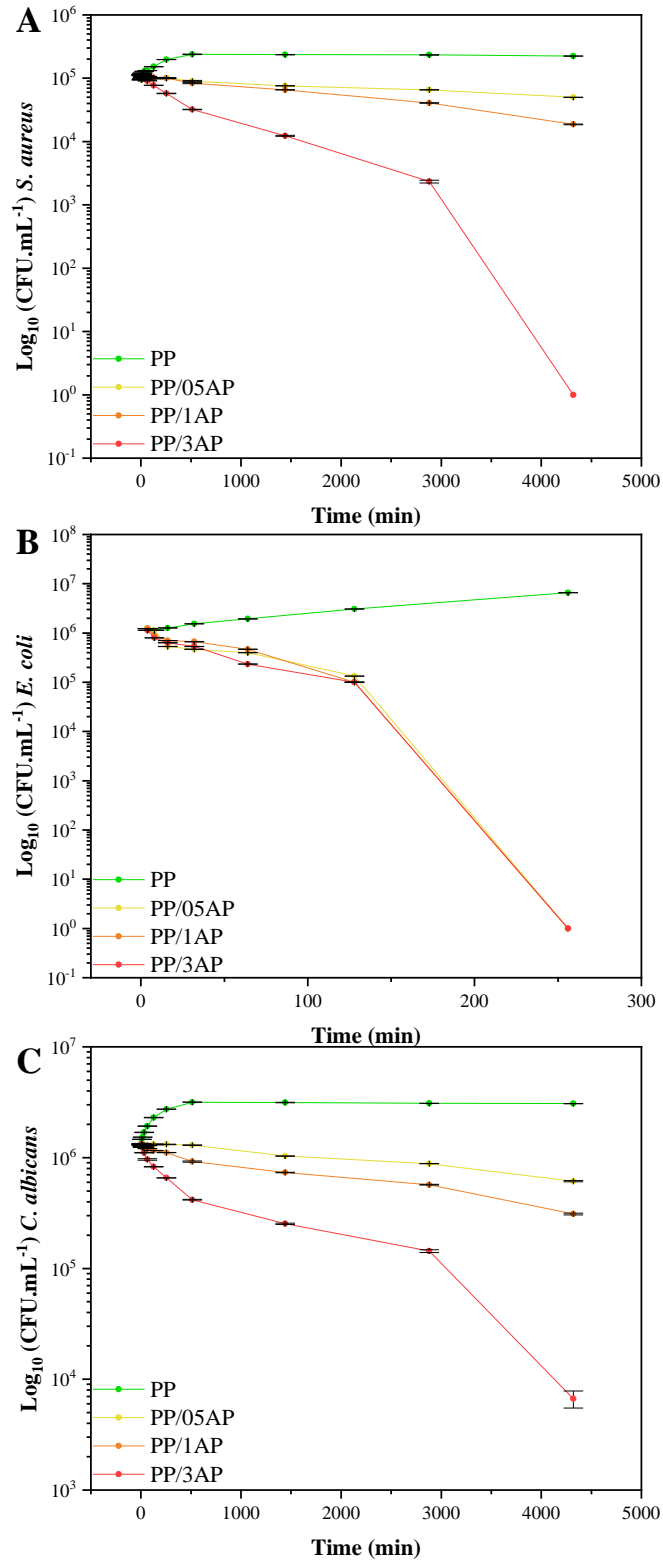


Figure 2.3. Time-kill curves for (A) *S. aureus*, (B) *E. coli*, and (C) *C. albicans* using PP, PP/05AP, PP/1AP and PP/3AP samples.

Concerning the elimination of more complex microorganisms, tests were carried out to verify the elimination of the SARS-CoV-2 virus by placing it on the surface of contact with the composite materials obtained for 5 min (see **Figure 2.4**). The result of viricidal efficacy is negative when the cytopathic effects are visualized and positive when there is no cytopathic effect detected. To determine the viral inhibition index, the logarithmic difference between the control group and group in contact with the composite samples (percentage of viral elimination, compared to viral control, viral solution and DMEN) was calculated. An analysis of the results renders that the PP and PP/05 AP samples (**Figures 2.4A-B**) do not show viral elimination, whereas the PP/1AP and PP/3AP samples (**Figures 2.4C-D**) reveal 90% viral elimination. The results regarding the increasing elimination as a function of the increase in the concentration of AP in the PP are consistent with the detections expected since the microbicidal action comes from the semiconductor.⁵⁹⁻⁶⁴ In addition, the semiconductor/polymer interaction impairs the surface fixation of pathogens in the composite, according to the contact angle results.

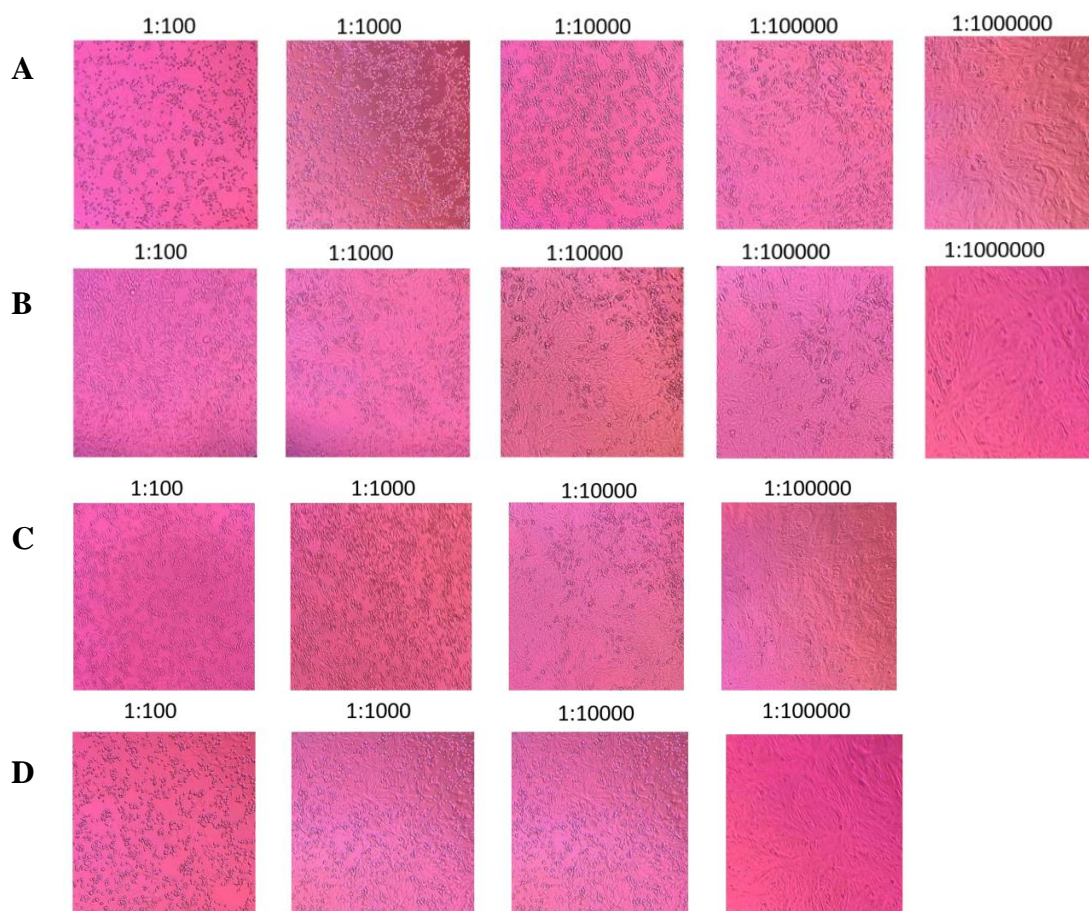


Figure 2.4. Microscopic images of cell cultures incubated with viral dilutions in contact with (A) PP, (B) PP/05AP, (C) PP/1AP and (D) PP/3AP samples.

It is well established that the photocatalytic and biocide activity of a given semiconductor is dependent on the efficient formation and separation of electrons (e^-) and holes (h^+) and the low recombination ratio of the e^-h^+ pair. It has potent antimicrobial activity, which is typically associated with the contact-induced membrane stress, are associated to the presence of reactive oxygen species (ROS), thus having potential for a variety of biomedical applications.^{18,65-68}

The activations of both molecular oxygen, O_2 , and water, H_2O , are fundamental step in almost all photocatalytic oxidation/reduction reactions and then the generation of ROS. At this point it is important to note the possible mechanism for the biocide activity is very dependent not only of the

oxidant/reduction capacity of the different ROS, but also of the nature of the radical chain reactions. Located in the valence band of the semiconductor, the h^+ reacts with H_2O to form hydroxyl radical ($\bullet OH$) and a proton (H^+), while the e^- , which is excited in the conduction band, interacts with O_2 to form $\bullet O_2^-$. Parallel reactions involving the formation of hydrogen peroxide (H_2O_2), which is developed during the disproportionation of $\bullet O_2^-$, can also occur, further transforming it into $\bullet OH$ and forming the singlet oxygen (1O_2). In summary, $\bullet OH$, H_2O_2 , $\bullet O_2^-$, and 1O_2 are generated by the stepwise oxidation of H_2O , while the stepwise reduction of O_2 generates $\bullet O_2^-$, H_2O_2 and $\bullet OH$. These free radicals and reactive species are capable of killing microorganisms by the oxidation and breaking of cellular constituents and membranes of bacteria, fungi and viruses.⁶⁹⁻⁷⁴ The ability to generate ROSs has been explored by analyzing the adsorption processes of H_2O and O_2 molecules on the Ag_3PO_4 (110) surface. This surface has been selected because several experimental⁷⁵⁻⁷⁹ and theoretical studies⁸⁰ report that this surface is responsible for the high catalytic activity of Ag_3PO_4 .

The Ag cations on the first two layers of the clean (110) surface are low 2-fold coordinated in comparison with 4-fold coordinated Ag cations in the bulk (see **Figure 2.5A**). This low coordination has already been reported as having a direct correspondence with increased biocide activity, consequently activating molecules that interact with an n-type semiconductor.⁸¹⁻⁸³ The Bader analysis of the electron density distribution⁸⁴ reveals that these Ag cations are more reduced than the innermost ones. Thus, the effective charge of the Ag_3PO_4 (110) surface from the topmost layer is $+0.50-0.52 |e|$, whereas the Ag bulk cations are $+0.41-0.44 |e|$. This fact suggests that Ag superficial cations would be preferential sites for molecular adsorption, promoting electron transfer processes to account for their lack of electron density.

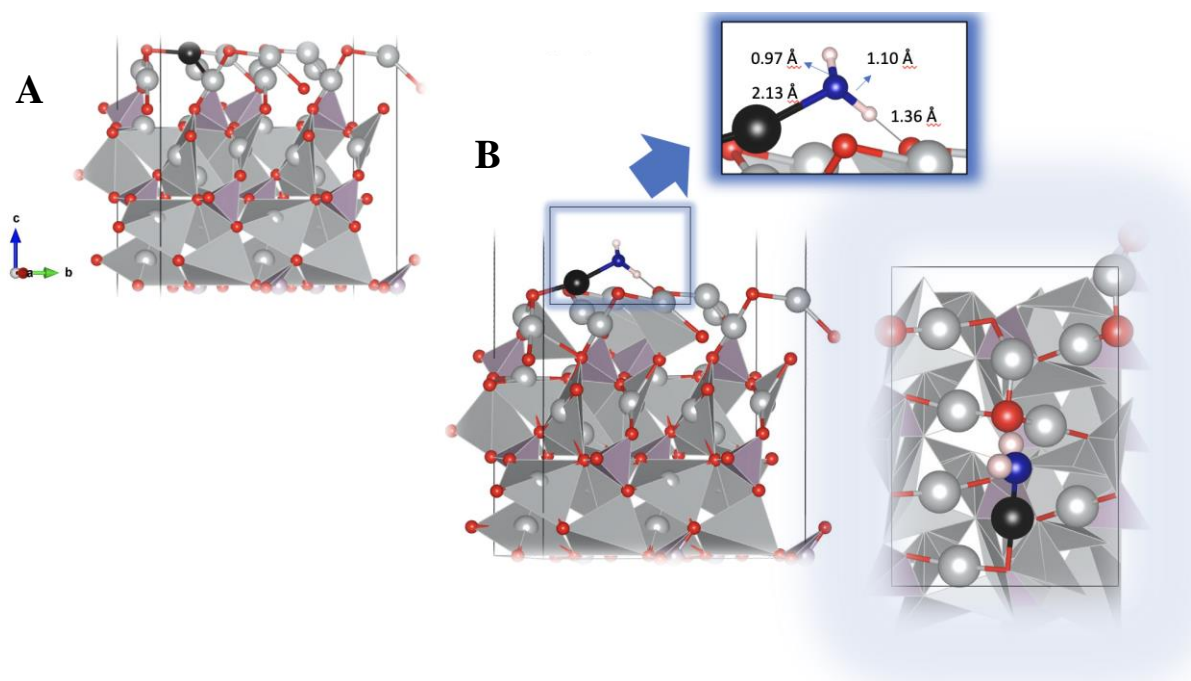


Figure 2.5. (A) Side views of the relaxed clean Ag_3PO_4 (110) surface. The Ag cation where H_2O and O_2 adsorb is highlighted in black color; (B) side and top views of the H_2O adsorption system. O, P and Ag atoms on the surface are represented by red, violet and grey balls, respectively. For clarity, the O and H atoms of the H_2O are indicated in blue and white colors, respectively.

Different superficial Ag cations were considered as potential sites for the H_2O molecule adsorption. The most favorable site with a calculated adsorption energy of -1.410 eV is depicted in **Figure 2.5B**. This adsorption process also distorts the surface with concomitant breaking bond processes between the Ag cation and the farthest O anion. The analysis of the bond critical points (BCP) demonstrates a significant weakening of the covalent bond between the O atom of H_2O and the H closer to the surface with concomitant enlargement of the bond distance from 0.97 Å to 1.10 Å. It is also shown that the H_2O molecule establishes a second bond with the surface in the form of a weak covalent bond between its H and the nearest surface O atom. The emerging Ag-O interaction between the H_2O and the surface is characterized as van der Waals-type

according to the Bader analysis. These results demonstrate that the n-type semiconductor surface activates the H₂O molecule, leading to the formation of the •OH and H⁺ species.

Ab initio molecular dynamics (AIMD) simulations at low temperatures (see Supporting Information video S1 and S2) starting from the described adsorption arrangement reveal the spontaneous breakage of the weakened O-H bond of the adsorbed H₂O molecule, corresponding to the early events associated to the formation of •OH and H⁺, which remain adsorbed on the surface. There is a O-H bond involving the nearest O atom on the second layer, whereas the •OH is linked to the Ag cation on the first layer. At a higher temperature (50 K), this process occurs more rapidly, with more intense vibrational frequencies of both newly formed H-O and Ag-O bonds (**Figure 2.5**).

Similarly, an O₂ molecule is adsorbed on the surface at the same site with calculated adsorption energy of -1.458 eV, as shown in **Figure 2.6A**. After the relaxation process, the molecule displays an increased bond length from 1.23 Å (for the free molecule) to 1.30 Å, a clear indication of bond weakening caused by the interaction with the surface (**Figure 2.6B**). Furthermore, the total spin calculated after adsorption corresponds to a doublet oxygen (S = 1/2), differently from the triplet (S = 1) for the free O₂ molecule. These results can be associated with the initial events resulting from the formation of the •O₂⁻ in the Ag₃PO₄ (110) surface.

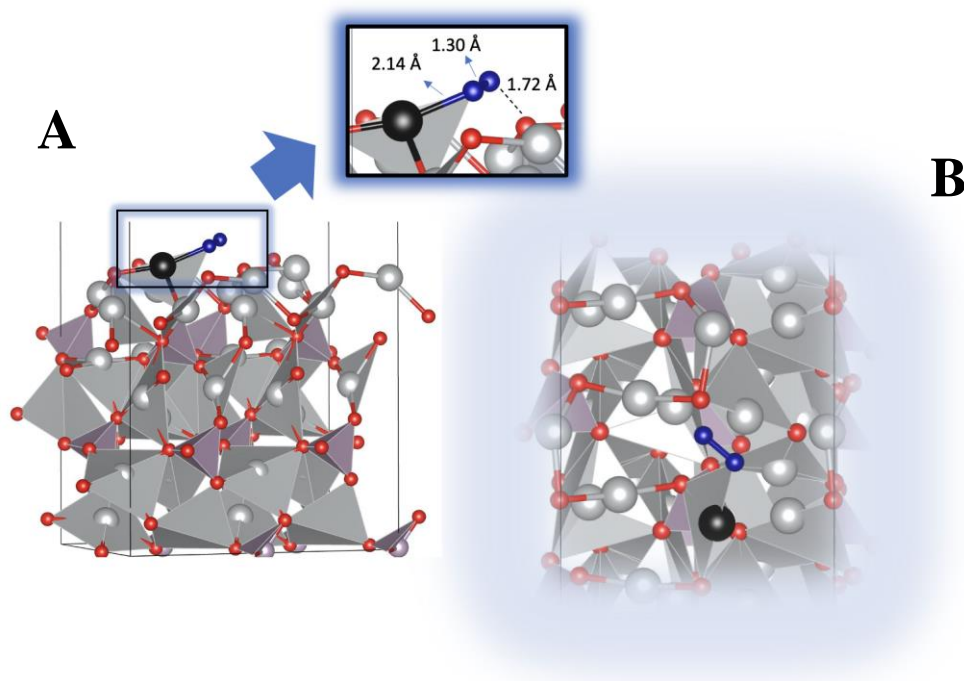


Figure 2.6. Side (A) and top (B) views of one O_2 molecule adsorbed on the Ag_3PO_4 (110) surface. O, P and Ag atoms on the surface are represented by red, violet and grey balls, respectively. For clarity, the Ag adsorption site and the water O are colored in black and blue, respectively.

2.4. Conclusions

Pathogen microorganisms (bacteria, fungi and viruses) represent a severe problem in public health. Therefore, there is great interest in developing advanced material and new technologies capable of inactivating opportunistic pathogens, thus reducing the risk of infection and transmission. In this work, an Ag_3PO_4 /polypropylene composite was developed and optimized for the first time. This composite has the physicochemical property of oxidizing bacteria (*Staphylococcus aureus* and *Escherichia coli*), fungi (*Candida albicans*) and SARS-COV-2 virus by surface contact. The adsorption processes of H_2O and O_2 molecules on the most active Ag_3PO_4 (110) surface were modeled through ab initio calculations to explain the early events of the formation of both hydroxyl

radical $\bullet\text{OH}$ and superoxide radical anion $\bullet\text{O}_2^-$ as reactive species in the biocide activity.

2.5. References

- (1) Han, Q.; Lin, Q.; Jin, S.; You, L. Coronavirus 2019-NCoV: A Brief Perspective from the Front Line. *J. Infect.* 2020, 80, 373–377.
- (2) Guan, W.-j.; Ni, Z.-y.; Hu, Y.; Liang, W.-h.; Ou, C.-q.; He, J.-x.; Liu, L.; Shan, H.; Lei, C.-l.; Hui, D. S. C.; et al. Clinical Characteristics of Coronavirus Disease 2019 in China. *N. Engl. J. Med.* 2020, 382, 1708–1720.
- (3) Rothan, H. A.; Byrareddy, S. N. The Epidemiology and Pathogenesis of Coronavirus Disease (COVID-19) Outbreak. *J. Autoimmun.* 2020, 109, 102433.
- (4) Chan, J. F.-W.; Kok, K.-H.; Zhu, Z.; Chu, H.; To, K. K.-W.; Yuan, S.; Yuen, K.-Y. Genomic Characterization of the 2019 Novel Human-Pathogenic Coronavirus Isolated from a Patient with Atypical Pneumonia after Visiting Wuhan. *Emerging Microbes Infect.* 2020, 9, 221–236.
- (5) Okba, N. M. A.; Müller, M. A.; Li, W.; Wang, C.; GeurtsvanKessel, C. H.; Corman, V. M.; Lamers, M. M.; Sikkema, R. S.; de Bruin, E.; Chandler, F. D.; et al. Severe Acute Respiratory Syndrome Coronavirus 2-Specific Antibody Responses in Corona- virus Disease Patients. *Emerging Infect. Dis.* 2020, 26, 1478–1488.
- (6) Su, S.; Wong, G.; Shi, W.; Liu, J.; Lai, A. C. K.; Zhou, J.; Liu, W.; Bi, Y.; Gao, G. F. Epidemiology, Genetic Recombination, and Pathogenesis of Coronaviruses. *Trends Microbiol.* 2016, 24, 490–502.
- (7) Shi, J.; Wen, Z.; Zhong, G.; Yang, H.; Wang, C.; Huang, B.; Liu, R.; He, X.; Shuai, L.; Sun, Z.; et al. Susceptibility of Ferrets, Cats, Dogs, and Other Domesticated Animals to SARS-Coronavirus 2. *Science* 2020, 368, 1016–1020.
- (8) Li, G.; Fan, Y.; Lai, Y.; Han, T.; Li, Z.; Zhou, P.; Pan, P.; Wang, W.; Hu, D.; Liu, X.; et al. Coronavirus Infections and Immune Responses. *J. Med. Virol.* 2020, 92, 424–432.
- (9) Aw, J. The Non-Contact Handheld Cutaneous Infra-Red Thermometer for Fever Screening during the COVID-19 Global Emergency. *J. Hosp. Infect.* 2020, 104, 451.
- (10) Chen, H.; Guo, J.; Wang, C.; Luo, F.; Yu, X.; Zhang, W.; Li, J.; Zhao, D.; Xu, D.; Gong, Q.; et al. Clinical Characteristics and Intrauterine Vertical Transmission Potential of COVID-19 Infection in Nine Pregnant Women: A Retrospective Review of Medical Records. *Lancet* 2020, 395, 809–815.
- (11) Shereen, M. A.; Khan, S.; Kazmi, A.; Bashir, N.; Siddique, R. COVID-19 infection: Emergence, transmission, and characteristics of human coronaviruses. *J. Adv. Res.* 2020, 24, 91–98.
- (12) Qiu, L.; Liu, X.; Xiao, M.; Xie, J.; Cao, W.; Liu, Z.; Morse, A.; Xie, Y.; Li, T.; Zhu, L. SARS-CoV-2 Is Not Detectable in the Vaginal Fluid of Women with Severe COVID-19 Infection. *Clin. Infect. Dis.* 2020, 71, 813–817.

- (13) Seminara, G.; Carli, B.; Forni, G.; Fuzzi, S.; Mazzino, A.; Rinaldo, A. Biological Fluid Dynamics of Airborne COVID-19 Infection. *Rend. Lincei* 2020, 31, 505–537.
- (14) Razzini, K.; Castrica, M.; Menchetti, L.; Maggi, L.; Negroni, L.; Orfeo, N. V.; Pizzoccheri, A.; Stocco, M.; Muttini, S.; Balzaretto, C. M. SARS-CoV-2 RNA detection in the air and on surfaces in the COVID-19 ward of a hospital in Milan, Italy. *Sci. Total Environ.* 2020, 742, 140540.
- (15) Wu, S.; Wang, Y.; Jin, X.; Tian, J.; Liu, J.; Mao, Y. Environmental Contamination by SARS-CoV-2 in a Designated Hospital for Coronavirus Disease 2019. *Am. J. Infect. Control* 2020, 48, 910–914.
- (16) Vardoulakis, S.; Sheel, M.; Lal, A.; Gray, D. COVID-19 environmental transmission and preventive public health measures. *Aust. N. Z. J. Public Health* 2020, 44, 333–335.
- (17) Tremiliosi, G. C.; Simoes, L. G. P.; Minozzi, D. T.; Santos, R. I.; Vilela, D. C. B.; Durigon, E. L.; Machado, R. R. G.; Medina, D. S.; Ribeiro, L. K.; Rosa, I. L. V.; et al. Ag Nanoparticles-Based Antimicrobial Polycotton Fabrics to Prevent the Transmission and Spread of SARS-CoV-2. *bioRxiv*: 2020.06.26.152520, 2020.
- (18) Gupta, A.; Mumtaz, S.; Li, C.-H.; Hussain, I.; Rotello, V. M. Combatting Antibiotic-Resistant Bacteria Using Nanomaterials. *Chem. Soc. Rev.* 2019, 48, 415–427.
- (19) Assis, M.; de Foggi, C. C.; Teodoro, V.; de Campos da Costa, J. P.; Silva, C. E.; Robeldo, T.; Caperucci, P. F.; Vergani, C. E.; Borra, R. C.; Sorribes, I.; et al. Surface-Dependent Photocatalytic and Biological Activities of Ag₂CrO₄: Integration of Experiment and Simulation. *Appl. Surf. Sci.* 2021, 545, 148964.
- (20) Pinatti, I. M.; Tello, A. C. M.; Trench, A. B.; de Foggi, C. C.; Pereira, P. F. S.; Teixeira, M. M.; Jacomaci, N.; Andrés, J.; Longo, E. Zinc-Substituted Ag₂CrO₄: A Material with Enhanced Photocatalytic and Biological Activity. *J. Alloys Compd.* 2020, 835, 155315.
- (21) Alvarez-Roca, R.; Gouveia, A. F.; de Foggi, C. C.; Lemos, P. S.; Gracia, L.; da Silva, L. F.; Vergani, C. E.; San-Miguel, M.; Longo, E.; Andrés, J. Selective Synthesis of α -, β -, and γ -Ag₂WO₄ Polymorphs: Promising Platforms for Photocatalytic and Antibacterial Materials. *Inorg. Chem.* 2021, 60, 1062–1079.
- (22) Foggi, C. C.; Fabbro, M. T.; Santos, L. P. S.; de Santana, Y. V. B.; Machado, A. L.; Cordoncillo, E.; Andrés, J.; Longo, E.; Longo, E. Synthesis and Evaluation of α -Ag₂WO₄ as Novel Antifungal Agent. *Chem. Phys. Lett.* 2017, 674, 125–129.
- (23) Cruz-Filho, J. F.; Costa, T. M. S.; Lima, M. S.; Noleto, L. F. G.; ^Bandeira, C. C. S.; Lima, F. L.; Luz, G. E. Microorganisms Photocatalytic Inactivation on Ag₃PO₄ Sub-Microcrystals Under WLEDs Light Source. *J. Inorg. Organomet. Polym. Mater.* 2021, 31, 2233.
- (24) de Foggi, C. C.; de Oliveira, R. C.; Fabbro, M. T.; Vergani, C. E.; Andres, J.; Longo, E.; Machado, A. L. Tuning the Morphological, Optical, and Antimicrobial Properties of α -Ag₂WO₄ Microcrystals Using Different Solvents. *Cryst. Growth Des.* 2017, 17, 6239–6246.

- (25) de Oliveira, R. C.; de Foggi, C. C.; Teixeira, M. M.; da Silva, M. D. P.; Assis, M.; Francisco, E. M.; Pimentel, B. N. A. d. S.; Pereira, P. F. d. S.; Vergani, C. E.; Machado, A. L.; et al. Mechanism of Antibacterial Activity via Morphology Change of α -AgVO₃: Theoretical and Experimental Insights. *ACS Appl. Mater. Interfaces* 2017, 9, 11472–11481.
- (26) De Foggi, C. C.; De Oliveira, R. C.; Assis, M.; Fabbro, M. T.; Mastelaro, V. R.; Vergani, C. E.; Gracia, L.; Andrés, J.; Longo, E.; Machado, A. L. Unveiling the Role of β -Ag₂MoO₄ Microcrystals to the Improvement of Antibacterial Activity. *Mater. Sci. Eng., C* 2020, 111, 110765.
- (27) Gouveia, A. F.; Gracia, L.; Longo, E.; San-Miguel, M. A.; Andrés, J. Modulating the Properties of Multifunctional Semi- conductors by Means of Morphology: Theory Meets Experiments. *Comput. Mater. Sci.* 2021, 188, 110217.
- (28) Yi, Z.; Ye, J.; Kikugawa, N.; Kako, T.; Ouyang, S.; Stuart- Williams, H.; Yang, H.; Cao, J.; Luo, W.; Li, Z.; et al. An Orthophosphate Semiconductor with Photooxidation Properties under Visible-Light Irradiation. *Nat. Mater.* 2010, 9, 559–564.
- (29) Zhang, H.; Huang, H.; Ming, H.; Li, H.; Zhang, L.; Liu, Y.; Kang, Z. Carbon Quantum Dots/Ag₃PO₄ Complex Photocatalysts with Enhanced Photocatalytic Activity and Stability under Visible Light. *J. Mater. Chem.* 2012, 22, 10501–10506.
- (30) Botelho, G.; Andres, J.; Gracia, L.; Matos, L. S.; Longo, E. Photoluminescence and Photocatalytic Properties of Ag₃PO₄ Micro- crystals: An Experimental and Theoretical Investigation. *Chemplu- schem* 2016, 81, 202–212.
- (31) Trench, A. B.; Machado, T. R.; Gouveia, A. F.; Foggi, C. C.; Teodoro, V.; Sánchez-Montes, I.; Teixeira, M. M.; Da Trindade, L. G.; Jacomaci, N.; Perrin, A.; et al. Rational Design of W-Doped Ag₃PO₄ as an Efficient Antibacterial Agent and Photocatalyst for Organic Pollutant Degradation. *ACS Omega* 2020, 5, 23808–23821.
- (32) Rakibuddin, M.; Ananthakrishnan, R. A Novel Ag Deposited Nanocoordination Polymer Derived Porous SnO₂/NiO Heteronanos- tructure for the Enhanced Photocatalytic Reduction of Cr(VI) under Visible Light. *New J. Chem.* 2016, 40, 3385–3394.
- (33) Dinh, C.-T.; Nguyen, T.-D.; Kleitz, F.; Do, T.-O. Large-Scale Synthesis of Uniform Silver Orthophosphate Colloidal Nanocrystals Exhibiting High Visible Light Photocatalytic Activity. *Chem. Commun.* 2011, 47, 7797–7799.
- (34) Huang, K.; Lv, Y.; Zhang, W.; Sun, S.; Yang, B.; Chi, F.; Ran, S.; Liu, X. One-Step Synthesis of Ag₃PO₄/Ag Photocatalyst with Visible- Light Photocatalytic Activity. *Mater. Res.* 2015, 18, 939–945.
- (35) Costa, T. M. S.; Lima, M. S.; Cruz Filho, J. F.; Silva, L. J.; Santos, R. S.; Luz, G. E. Synthesis, Characterization, and Photo- catalytic Activity of Ag₃PO₄/SBA-15 in Ciprofloxacin Degradation under Polychromatic Irradiation. *J. Photochem. Photobiol., A* 2018, 364, 461–471.
- (36) Cruz-Filho, J. F.; Costa, T. M. S.; Lima, M. S.; Silva, L. J.; Santos, R. S.; Cavalcante, L. S.; Longo, E.; Luz, G. E. Effect of Different Synthesis Methods on

the Morphology, Optical Behavior, and Superior Photocatalytic Performances of Ag₃PO₄ Sub-Micro- crystals Using White-Light-Emitting Diodes. *J. Photochem. Photobiol., A* 2019, 377, 14–25.

(37) de Costa, J. P. C.; Assis, M.; Teodoro, V.; Rodrigues, A.; Cristina de Foggi, C.; San-Miguel, M. A.; Pereira do Carmo, J. P.; Andrés, J.; Longo, E. Electron Beam Irradiation for the Formation of Thick Ag Film on Ag₃PO₄. *RSC Adv.* 2020, 10, 21745–21753.

(38) dos Santos, C. C.; Assis, M.; Machado, T. R.; dos Santos Pereira, P. F.; Minguez-Vega, G.; Cordoncillo, E.; Beltran-Mir, H.; Doñate-Buendía, C.; Andrés, J.; Longo, E. Proof-of-Concept Studies Directed toward the Formation of Metallic Ag Nanostructures from Ag₃PO₄ Induced by Electron Beam and Femtosecond Laser. *Part. Part. Syst. Charact.* 2019, 36, 1800533.

(39) Botelho, G.; Sczancoski, J. C.; Andres, J.; Gracia, L.; Longo, E. Experimental and Theoretical Study on the Structure, Optical Properties, and Growth of Metallic Silver Nanostructures in Ag₃PO₄. *J. Phys. Chem. C* 2015, 119, 6293–6306.

(40) Guo, R.; Wu, J.; Xu, A.; Huang, X.; Zhu, H.; Jiang, R.; Lin, Y.; Guo, F. ZnWO₄/Ag₃PO₄ Composites with an Enhanced Photo- catalytic Activity and Stability under Visible Light. *RSC Adv.* 2016, 6, 114818–114824.

(41) Hsieh, M.-S.; Su, H.-J.; Hsieh, P.-L.; Chiang, Y.-W.; Huang, M. H. Synthesis of Ag₃PO₄ Crystals with Tunable Shapes for Facet- Dependent Optical Property, Photocatalytic Activity, and Electrical Conductivity Examinations. *ACS Appl. Mater. Interfaces* 2017, 9, 39086–39093.

(42) Li, X.; Xu, P.; Chen, M.; Zeng, G.; Wang, D.; Chen, F.; Tang, W.; Chen, C.; Zhang, C.; Tan, X. Application of Silver Phosphate- Based Photocatalysts: Barriers and Solutions. *Chem. Eng. J.* 2019, 366, 339–357. (43) Kamal, M. M.; Safan, M. A.; Etman, Z. A.; Kasem, B. M. Mechanical Properties of Self- Compacted Fiber Concrete Mixes. *HBRC J.* 2014, 10, 25–34.

(44) Ghaffari, M.; Mollazadeh-Bajestani, M.; Moztafzadeh, F.; Uludağ, H.; Hardy, J. G.; Mozafari, M. An Overview of the Use of Biomaterials, Nanotechnology, and Stem Cells for Detection and Treatment of COVID-19: Towards a Framework to Address Future Global Pandemics. *Emergent Mater.* 2021, 4, 19–34.

(45) Martí, M.; Tuñón-Molina, A.; Aachmann, F.; Muramoto, Y.; Noda, T.; Takayama, K.; Serrano-Aroca, Á. Protective Face Mask Filter Capable of Inactivating SARS-CoV-2, and Methicillin-Resistant Staphylococcus Aureus and Staphylococcus Epidermidis. *Polymers* 2021, 13, 207.

(46) Abraham, J.; Sharika, T.; George, S. C.; Thomas, S. Rheology: Open Access Rheological Percolation in Thermoplastic Polymer Nanocomposites. *Rheol. Open access* 2017, 1, 1–15.

(47) Terpilowski, K.; Rymuszka, D.; Holysz, L.; Chibowski, E. Changes in Wettability of Polycarbonate and Polypropylene Pre- treated With Oxygen and Argon Plasma. *Proceedings of the 8th International Conference MMT-20142*, Ariel, Israel, 2014; Vol. 4, pp 155–165.

- (48) Kasraei, S.; Azarsina, M. Addition of Silver Nanoparticles Reduces the Wettability of Methacrylate and Silorane-Based Composites. *Braz. Oral Res.* 2012, 26, 505–510.
- (49) Liu, Q.; Brookbank, L.; Ho, A.; Coffey, J.; Brennan, A. B.; Jones, C. J. Surface Texture Limits Transfer of *S. Aureus*, T4 Bacteriophage, Influenza B Virus and Human Coronavirus. *PLoS One* 2021, 15, No. e0244518.
- (50) Hosseini, M.; Chin, A. W. H.; Behzadinasab, S.; Poon, L. L. M.; Ducker, W. A. Cupric Oxide Coating That Rapidly Reduces Infection by SARS-CoV-2 via Solids. *ACS Appl. Mater. Interfaces* 2021, 13, 5919.
- (51) Piccirillo, C.; Pinto, R. A.; Tobaldi, D. M.; Pullar, R. C.; Labrincha, J. A.; Pintado, M. M. E.; Castro, P. M. L. Light Induced Antibacterial Activity and Photocatalytic Properties of Ag₃PO₄-Based Material of Marine Origin. *J. Photochem. Photobiol., A* 2015, 296, 40–47.
- (52) Gherasim, O.; Puiu, R. A.; Birca, A. C.; Burdus̃el, A.-C.; Grumezescu, A. M. An Updated Review on Silver Nanoparticles in Biomedicine. *Nanomaterials* 2020, 10, 2318–44.
- (53) Liou, J.-W.; Chang, H.-H. Bactericidal Effects and Mechanisms of Visible Light-Responsive Titanium Dioxide Photocatalysts on Pathogenic Bacteria. *Arch. Immunol. Ther. Exp* 2012, 60, 267–275.
- (54) Macedo, N. G.; Machado, T. R.; Roca, R. A.; Assis, M.; Foggi, C. C.; Puerto-Belda, V.; Mínguez-Vega, G.; Rodrigues, A.; San-Miguel, M. A.; Cordoncillo, E.; et al. Tailoring the Bactericidal Activity of Ag Nanoparticles/ α -Ag₂WO₄ Composite Induced by Electron Beam and Femtosecond Laser Irradiation: Integration of Experiment and Computational Modeling. *ACS Appl. Bio Mater.* 2019, 2, 824–837.
- (55) Roca, R. A.; Sczancoski, J. C.; Nogueira, I. C.; Fabbro, M. T.; Alves, H. C.; Gracia, L.; Santos, L. P. S.; De Sousa, C. P.; Andrés, J.; Luz, G. E.; et al. Facet-Dependent Photocatalytic and Antibacterial Properties of α -Ag₂WO₄ Crystals: Combining Experimental Data and Theoretical Insights. *Catal. Sci. Technol.* 2015, 5, 4091–4107.
- (56) Abram, S. L.; Fromm, K. M. Handling (Nano)Silver as Antimicrobial Agent: Therapeutic Window, Dissolution Dynamics, Detection Methods and Molecular Interactions. *Chem.Eur. J.* 2020, 26, 10948–10971.
- (57) Choi, Y.; Kim, H.-A.; Kim, K.-W.; Lee, B.-T. Comparative Toxicity of Silver Nanoparticles and Silver Ions to *Escherichia Coli*. *J. Environ. Sci.* 2018, 66, 50–60.
- (58) Berlanga, M.; Montero, M. T.; Hernández-Borrell, J.; Viñas, M. Influence of the Cell Wall on Ciprofloxacin Susceptibility in Selected Wild-Type Gram-Negative and Gram-Positive Bacteria. *Int. J. Antimicrob. Agents* 2004, 23, 627–630.
- (59) Barzegar, H.; Zahed, M. A.; Vatanpour, V. Antibacterial and Antifouling Properties of Ag₃PO₄/GO Nanocomposite Blended Polyethersulfone Membrane Applied in Dye Separation. *J. Water Process Eng.* 2020, 38, 101638.
- (60) Tamiyakul, H.; Roytrakul, S.; Jaresitthikunchai, J.; Phaonakrop, N.; Tanasupawat, S.; Warisnoicharoen, W. Changes in Protein Patterns of *Staphylococcus Aureus* and *Escherichia Coli* by Silver Nanoparticles Capped

with Poly (4-Styrenesulfonic Acid-Co-Maleic Acid) Polymer. *Asian Biomed.* 2019, 13, 39–47.

(61) Salleh, A.; Naomi, R.; Utami, N. D.; Mohammad, A. W.; Mahmoudi, E.; Mustafa, N.; Fauzi, M. B. The Potential of Silver Nanoparticles for Antiviral and Antibacterial Applications: A Mechanism of Action. *Nanomaterials* 2020, 10, 1566.

(62) Nakamura, S.; Sato, M.; Sato, Y.; Ando, N.; Takayama, T.; Fujita, M.; Ishihara, M. Synthesis and Application of Silver Nanoparticles (Ag NPs) for the Prevention of Infection in Healthcare Workers. *Int. J. Mol. Sci.* 2019, 20, 3620.

(63) Kubo, A.-L.; Capjak, I.; Vrcek, I. V.; Bondarenko, O. M.; Kurvet, I.; Vija, H.; Ivask, A.; Kasemets, K.; Kahru, A. Antimicrobial Potency of Differently Coated 10 and 50 Nm Silver Nanoparticles against Clinically Relevant Bacteria *Escherichia Coli* and *Staphylococcus Aureus*. *Colloids Surf., B* 2018, 170, 401–410.

(64) Chang, B.-M.; Pan, L.; Lin, H.-H.; Chang, H.-C. Nano- diamond-Supported Silver Nanoparticles as Potent and Safe Antibacterial Agents. *Sci. Rep.* 2019, 9, 1–11.

(65) Basak, S.; Packirisamy, G. Nano-Based Antiviral Coatings to Combat Viral Infections. *Nano-Struct. Nano-Objects* 2020, 24, 100620.

(66) Mukherjee, S.; Mazumder, P.; Joshi, M.; Joshi, C.; Dalvi, S. V.; Kumar, M. Biomedical Application, Drug Delivery and Metabolic Pathway of Antiviral Nanotherapeutics for Combating Viral Pandemic: A Review. *Environ. Res.* 2020, 191, 110119.

(67) Jeremiah, S. S.; Miyakawa, K.; Morita, T.; Yamaoka, Y.; Ryo, A. Potent Antiviral Effect of Silver Nanoparticles on SARS-CoV-2. *Biochem. Biophys. Res. Commun.* 2020, 533, 195–200.

(68) Assis, M.; Simoes, L. G. P.; Tremiliosi, G. C.; Coelho, D.; Minozzi, D. T.; Santos, R. I.; Vilela, D. C. B.; Santos, J. R. d.; Ribeiro, L. K.; Rosa, I. L. V.; et al. SiO₂-Ag Composite as a Highly Virucidal Material : A Roadmap That Rapidly Eliminates SARS-CoV-2. *Nanomaterials* 2021, 11, 638.

(69) Lakshmi Prasanna, V.; Vijayaraghavan, R. Insight into the Mechanism of Antibacterial Activity of ZnO: Surface Defects Mediated Reactive Oxygen Species Even in the Dark. *Langmuir* 2015, 31, 9155–9162.

(70) Zhang, W.; Li, Y.; Niu, J.; Chen, Y. Photogeneration of Reactive Oxygen Species on Uncoated Silver, Gold, Nickel, and Silicon Nanoparticles and Their Antibacterial Effects. *Langmuir* 2013, 29, 4647–4651.

(71) Li, Y.; Zhang, W.; Niu, J.; Chen, Y. Mechanism of Photogenerated Reactive Oxygen Species and Correlation with the Antibacterial Properties of Engineered Metal-Oxide Nanoparticles. *ACS Nano* 2012, 6, 5164–5173.

(72) Fujii, M.; Usui, M.; Hayashi, S.; Gross, E.; Kovalev, D.; Künzner, N.; Diener, J.; Timoshenko, V. Y. Chemical reaction mediated by excited states of Si nanocrystals-Singlet oxygen formation in solution. *J. Appl. Phys.* 2004, 95, 3689–3693.

(73) Du, J.; Gebicki, J. M. Proteins Are Major Initial Cell Targets of Hydroxyl Free Radicals. *Int. J. Biochem. Cell Biol.* 2004, 36, 2334– 2343.

- (74) Tian, Z.; Li, X.; Ma, Y.; Chen, T.; Xu, D.; Wang, B.; Qu, Y.; Gao, Y. Quantitatively Intrinsic Biomimetic Catalytic Activity of Nanocerias as Radical Scavengers and Their Ability against H₂O₂ and Doxorubicin-Induced Oxidative Stress. *ACS Appl. Mater. Interfaces* 2017, 9, 23342–23352.
- (75) Guo, R.; Fan, Y.; Tang, Y. Interesting Ag₃PO₄ Concave Rhombic Dodecahedra: The Same Face with Different Morphologies and Photocatalytic Properties. *RSC Adv.* 2017, 7, 23977–23981.
- (76) Wang, H.; He, L.; Wang, L.; Hu, P.; Guo, L.; Han, X.; Li, J. Facile Synthesis of Ag₃PO₄ Tetrapod Microcrystals with an Increased Percentage of Exposed {110} Facets and Highly Efficient Photo- catalytic Properties. *CrystEngComm* 2012, 14, 8342–8344.
- (77) Wang, J.; Teng, F.; Chen, M.; Xu, J.; Song, Y.; Zhou, X. Facile Synthesis of Novel Ag₃PO₄ Tetrapods and the {110} Facets- Dominated Photocatalytic Activity. *CrystEngComm* 2013, 15, 39–42.
- (78) Li, M.; Chen, M.; Wang, J.; Teng, F. Branching Growth of Novel Silver Phosphate Dendrites and the Greatly Improved Photocatalytic Activity by the Active {110} Facets. *CrystEngComm* 2014, 16, 1237–1240.
- (79) Batvandi, M.; Haghighatzadeh, A.; Mazinani, B. Synthesis of Ag₃PO₄ Microstructures with Morphology-Dependent Optical and Photocatalytic Behaviors. *Appl. Phys. A* 2020, 126, 571.
- (80) Lipsky, F.; Lacerda, L. H. D. S.; De Lazaro, S. R.; Longo, E.; Andrés, J.; San-Miguel, M. A. Unraveling the Relationship between Exposed Surfaces and the Photocatalytic Activity of Ag₃PO₄: An in- Depth Theoretical Investigation. *RSC Adv.* 2020, 10, 30640–30649.
- (81) Bi, Y.; Ouyang, S.; Umezawa, N.; Cao, J.; Ye, J. Facet Effect of Single-Crystalline Ag₃PO₄ Sub-Microcrystals on Photocatalytic Properties. *J. Am. Chem. Soc.* 2011, 133, 6490–6492.
- (82) Bomio, M. R. D.; Tranquilin, R. L.; Motta, F. V.; Paskocimas, C. A.; Nascimento, R. M.; Gracia, L.; Andres, J.; Longo, E. Toward Understanding the Photocatalytic Activity of PbMoO₄ Powders with Predominant (111), (100), (011), and (110) Facets. A Combined Experimental and Theoretical Study. *J. Phys. Chem. C* 2013, 117, 21382–21395.
- (83) Lazzeri, M.; Vittadini, A.; Selloni, A. Structure and Energetics of Stoichiometric TiO₂ Anatase Surfaces. *Phys. Rev. B: Condens. Matter Mater. Phys.* 2001, 63, 155409.
- (84) Eugen Schwarz, W. H.; Bader, W. H. R. F. Richard F. Bader: Atoms in Molecules (A Quantum Theory) Clarendon Press 1990.

Capítulo 3

Polypropylene modified with Ag-based semiconductors as potential material against SARS-CoV-2 and other pathogens

ACS Applied Polymer Materials, 4(10), 7102-7114

**Marcelo Assis^a, Lara K. Ribeiro^{a,b}, Mariana O. Gonçalves^c, Lucas H. Staffa^d,
Robert S. Paiva^d, Lais R. Lima^d, Dyovani Coelho^b, Lauana F. Almeida^{e,f},
Leonardo N. Moraes^{e,f}, Ieda L. V. Rosa^b, Lucia H. Mascaro^b, Rejane M. T.
Grotto^{e,f}, Cristina P. Sousa^c, Juan Andrés^a, Elson Longo^b, Sandra A. Cruz^d**

^aDepartment of Physical and Analytical Chemistry, University Jaume I (UJI), Castelló 12071.

^bCDMF, LIEC, Federal University of São Carlos - (UFSCar), São Carlos, SP, 13565-905 Brazil.

^cBiomolecules and Microbiology Laboratory (LaMiB), Biotechnology Graduation Program (PPGBiotec), Federal University of São Carlos (UFSCar), São Carlos, SP, 13565-905, Brazil.

^dChemistry Department, Federal University of São Carlos (UFSCar), São Carlos, SP, 13565-905, Brazil.

^eSchool of Agriculture, São Paulo State University (Unesp), Botucatu, SP, 18610-034, Brazil.

^fMolecular Laboratory of Clinical Hospital of Botucatu, Medical School, São Paulo State University (Unesp), Botucatu, SP, 18618-687, Brazil.

ABSTRACT. The worldwide outbreak of the coronavirus pandemic (COVID-19) and other emerging infections are difficult and some-times impossible to treat, making them one of the major public health problems of our time. It is noteworthy that Ag-based semiconductors can orchestrate several strategies to fight this serious societal issue. In this work, we present the synthesis of α - Ag_2WO_4 , β - Ag_2MoO_4 and Ag_2CrO_4 and their immobilization in polypropylene in the amounts of 0.5, 1.0 and 3.0% wt., respectively. The antimicrobial activity of the composites was investigated against the Gram-negative bacterium *Escherichia coli*, the Gram-positive bacterium *Staphylococcus aureus* and the fungus *Candida albicans*. The best antimicrobial efficiency was achieved by the composite with α - Ag_2WO_4 , which completely eliminated the microorganisms in up to 4 hours of exposure. The composites were also tested for the inhibition of SARS-CoV-2 virus, showing antiviral efficiency higher than 98% in just 10 min. Additionally, we evaluated the maintenance of the antimicrobial activity, resulting in constant inhibition, even after material aging. The antimicrobial activity of the compounds was attributed to the production of reactive oxygen species by the semiconductors, which can induce high local oxidative stress, causing the death of these microorganisms.

KEYWORDS. Composites, α - Ag_2WO_4 , β - Ag_2MoO_4 , Ag_2CrO_4 , antimicrobial material, anti-SARS-CoV-2 material.

3.1 Introduction

The recent outbreak of a new coronavirus disease (COVID-19) caused by SARS-CoV-2 has severely impacted life worldwide.^{1,2} This virus can be easily transmitted by human body fluids through airborne aerosol droplets (direct form) or contamination of infected surfaces (indirect form).³ Contagion by contaminated surfaces is responsible for a significant portion of infections, and recent research has suggested that these viruses can survive for several days on different surfaces after being expelled by human fluids and that their

viability is determined by the nature of the surface.⁴ Therapeutic strategies based on materials represent a promising approach to overcome the limitations found in the prevention, diagnosis and therapies against SARS-CoV-2.⁵ In particular, materials with antimicrobial properties can be used in personal protective equipment and disinfection protocols to prevent contamination by SARS-CoV-2.^{5,6}

Many diseases can be spread to humans by fomite transmission, being them fungal, bacterial or viral.^{7,8} Thus, the factors that contribute to the survival of enveloped viruses, fungi and bacteria on surfaces are of societal interest. One way to reduce the transmission of COVID-19 via surfaces is to design coatings based on functional nanoparticles that eliminate SARS-CoV-2 and apply them on common surfaces, such as door handles, bus supports, etc., continuously reducing the elimination period from weeks to minutes or hours.⁹ Additionally, polypropylene (PP) is currently one of the most consumed polymers for the manufacture of nonwoven surgical masks and aprons utilized in clinics and hospitals, besides being widely used as a packaging material. Despite the importance of this polymer in preventing and spreading the disease, a recent study indicated that the virus can be active for up to three days in surgical masks.¹⁰

Materials based on metals and semiconductor oxides are of particular industrial and biotechnological interest due to their unique properties and applications.¹¹ In this context, Behzadinasab et al. and Hosseini et al. observed that coatings based on copper oxides can eliminate copies of the genetic material of SARS-CoV-2 when in contact with these surfaces as a result of the production of ROS, which are capable to degrade the constituent proteins of the virus.^{12,13} Promising results were also obtained using other semiconductors, such as ZnO, TiO₂ and Fe₂O₃/Fe₃O₄.¹⁴⁻¹⁶ Noble metal particles such as Au and Ag were also reported as anti-SARS-CoV-2 materials since they can interact with various functional groups that compose the virus, preventing its replication processes or destroying it.¹⁷⁻¹⁹ Carbon-based materials, e.g.,

graphene and chitosan, were also found to be effective against the virus, as these particles interact permanently with the RNA strands.^{20,21} An interesting advantage to using inorganic materials to fight viruses in general is that the virus is less likely to develop resistance than in conventional therapies.²²⁻²⁴ Our research group has made some progress towards the development of materials with anti-SARS-CoV-2 properties. First, we effectively incorporated Ag nanoparticles into polycotton.²⁵ We observed that in just 2 min it was possible to reduce 99.60% of the genetic viral copies when in contact with this tissue. In addition, this material proved to be particularly effective against the pathogenic microorganisms tested, without causing any type of dermatitis to its user. In another works, we were able to immobilize SiO₂-Ag particles in different polymers, reaching over 99% of viral clearance in just 15 min.^{3,26} Very recently, we reported that the incorporation of Ag₃PO₄ into a polymer matrix leads to a composite with antimicrobial action against SARS-CoV-2 and other opportunistic and potential pathogens.²⁷

In this work we discuss how the immobilization of silver-based semiconductors such as α -Ag₂WO₄, β -Ag₂MoO₄ and Ag₂CrO₄ on PP renders a composite with improved antimicrobial activity. The antimicrobial activities were evaluated against Gram-positive (*Staphylococcus aureus*) and Gram-negative (*Escherichia coli*) bacteria, fungus (*Candida albicans*) and SARS-CoV-2 virus. The structural evaluation of the composites was carried out by obtaining correlations between their antimicrobial activity and structure.

3.2. Experimental section

PP was purchased from Braskem (Prism 2400), São Paulo, Brazil. PP presents a melt flow index (MFI) of 20 g/10 min (ASTM 1238, 230 °C, 2.16 kg) and a density of 0.902 g/cm³ (ASTM D 792). Silver tungstate (α -Ag₂WO₄), silver molybdate (β -Ag₂MoO₄) and silver chromate (Ag₂CrO₄) particles were synthesized by the co-precipitation method (see Supporting Information for details about the synthesis of semiconductors).

The composites were compounded using a Thermo Scientific internal mixer model Polylab OS equipped with a counter-rotating rotor connected to a Rheomix 600 OS Lab mixing chamber. The conditions employed were temperature of 200 °C and rotor speed of 50 rpm for 4 min with closed and locked chamber. The chamber operated with 70% of its capacity. The semiconductor was incorporated into the polymer (PP) in proportions of 0.5, 1.0, and 3.0% wt. The processing conditions, especially regarding the profile and temperatures, was outlined to ensure an adequate dispersive and distributive total mixture. The samples were named according to the semiconductor content as follows: PPAW05, PPAW1 and PPAW3 for α -Ag₂WO₄; PPAM05, PPAM1 and PPAM3 for β -Ag₂MoO₄; and PPAC05, PPAC1 and PPAC3 for Ag₂CrO₄.

Details about antimicrobial tests and materials characterizations can be found in the *Appendices' B*.

3.3. Results and discussion

The XRD patterns were obtained to evaluate the crystallinities of the pure PP, the metal oxides (α -Ag₂WO₄, β -Ag₂MoO₄ and Ag₂CrO₄) and the composites samples. **Figure 3.1A** exhibit the diffraction peaks characteristic of the α -Ag₂WO₄ attributed to diffraction planes according to JCPDS No. 70-1719, the results can be well indexed as orthorhombic structure. **Figure 3.1B** exhibit the diffraction peaks characteristic of the β -Ag₂MoO₄ attributed to diffraction planes according to JCPDS No. 08-0473, the results can be well indexed as cubic structure. **Figure 3.1C** exhibit the diffraction peaks characteristic of the Ag₂CrO₄ attributed to diffraction planes according to JCPDS No. 26-0952. These diffraction peaks show that the phase can be indexed to the orthorhombic structure of Ag₂CrO₄. **Figure 3.1** revealed the presence of the diffraction peaks (110), (040), (130) and (131) + (041) approximate $2\theta = 15^\circ$, 17° , 19° and 22° , respectively, for all the polymeric samples. These crystalline planes show that PP samples presents the alpha phase of PP, with a monoclinic

unit cell.²⁸ The presence of the plane (130) indicates the polymorphism of PP, a common phenomenon in crystalline polymers.²⁹ These diffractograms exhibit all the peaks of the PP, suggesting that the structure of the PP was maintained during the process of obtaining the composite.³⁰ In addition, it is possible to verify the appearance of the semiconductor peaks, in the composite's samples with 3% of the semiconductors. The appearance of these peaks suggests that the structure of the semiconductors was also maintained during the process of obtaining the composite.

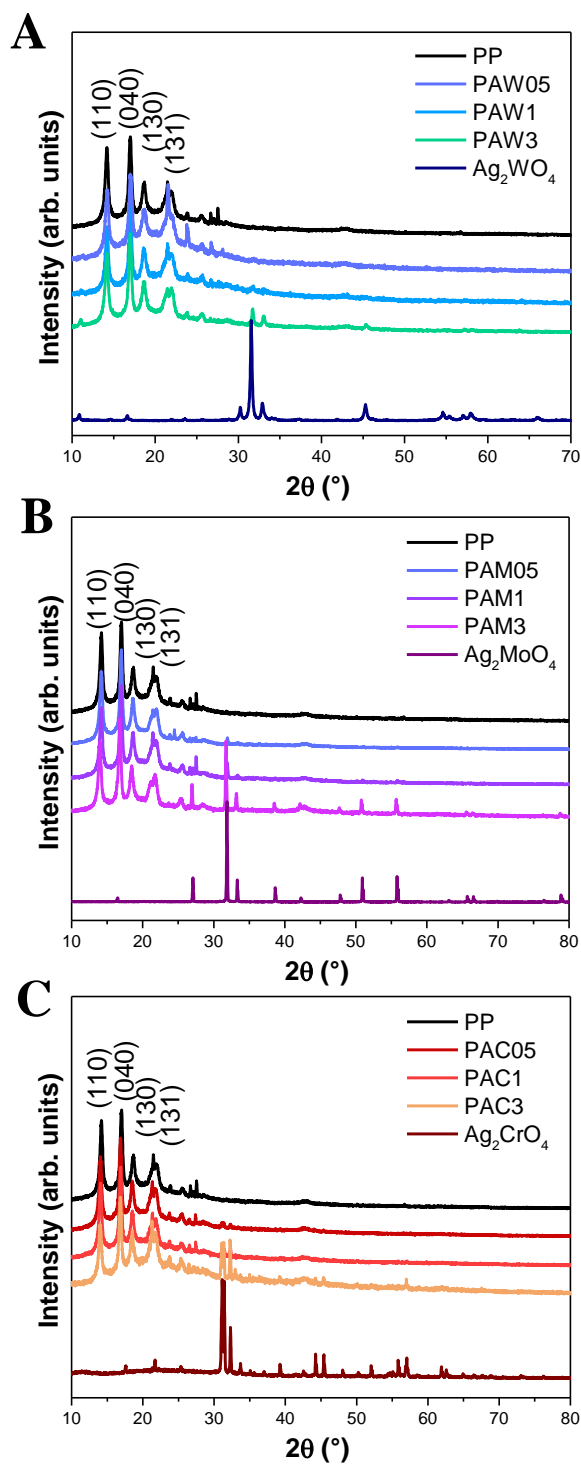


Figure 3.1. Diffractograms of the semiconductors/polypropylene. The PPAW (A), PPAM (B) and PPAC (C).

The samples were characterized by FTIR for to check the new interactions at short-range between the PP and the semiconductors ($\alpha\text{-Ag}_2\text{WO}_4$, $\beta\text{-Ag}_2\text{MoO}_4$

and Ag_2CrO_4) (**Figure 3.2**). The changes in C–C vibrations of symmetrical deformation, asymmetric deformations in C–H₃ and shear vibrations of C–H₂, carbonyl species (CO), C–H vibrations were observed by FTIR peaks at approximately: 1160, 1800-1600, 2800-2900 cm^{-1} , respectively.^{31,32} These changes may represent the modifications created in the PP with the insertion of the different semiconductors. For all composites formed with $\alpha\text{-Ag}_2\text{WO}_4$, $\beta\text{-Ag}_2\text{MoO}_4$ and Ag_2CrO_4 , there is a clear difference in the peak located at 600-900 cm^{-1} , which widens with the increase in the percentage of semiconductor in the polymer matrix. This widening indicates the overlapping of the absorption band of the clusters lattice former of the semiconductor, which occurs around ~600-1000 cm^{-1} .³³ For the $\alpha\text{-Ag}_2\text{WO}_4$ (**Figure 3.2A**), the peak of the $[\text{WO}_6]$ clusters occur at 847 cm^{-1} , in addition to this difference between the spectra of PP and semiconductor/PP composites in materials with $\alpha\text{-Ag}_2\text{WO}_4$, another change in the range of 749 cm^{-1} can be seen due to the vibrations of the W–O bonds. The $\beta\text{-Ag}_2\text{MoO}_4$ (**Figure 3.2B**) showed peak of the $[\text{MoO}_4]$ clusters at 842 cm^{-1} , showing another difference between the spectra in the range of 638 cm^{-1} due to the vibrations of the Mo–O bonds. The Ag_2CrO_4 (**Figure 3.2C**), the peak of the $[\text{CrO}_4]$ clusters occur at 842 cm^{-1} . These changes indicate that there is an interaction between the polymeric matrix and the semiconductor at short- and long-range. Furthermore, the DRS results presented in **Figures B.1-B.2** and **Tables B.1-B.2** (*Appendices B*) confirm these results.

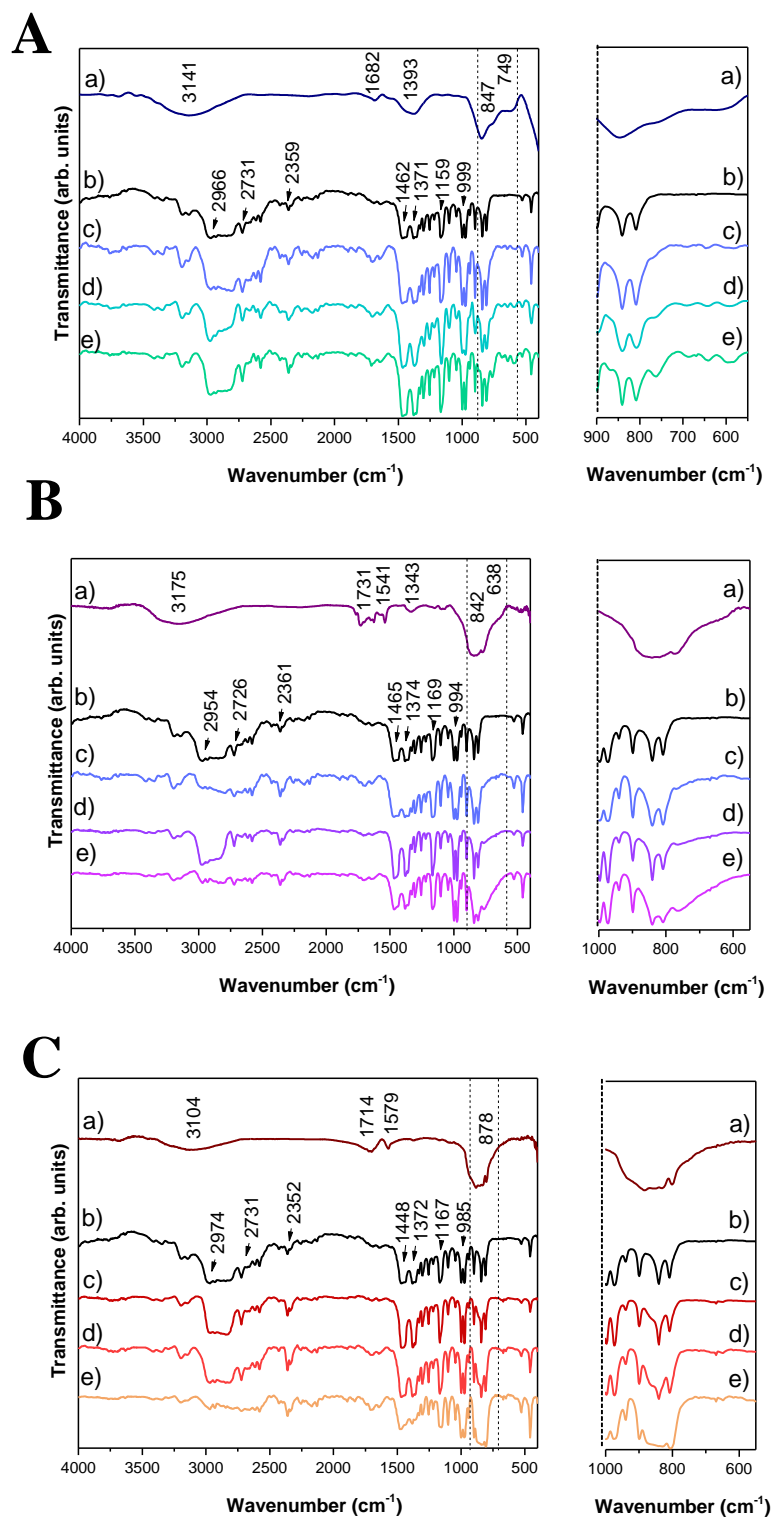


Figure 3.2. FTIR of the PPAW ($\alpha\text{-Ag}_2\text{WO}_4$) (a); PP (b); PPAW05 (c); PPAW1 (d); PPAW3 (e) (A), PPAM ($\beta\text{-Ag}_2\text{MoO}_4$) (a); PP (b); PPAM05 (c); PPAM1 (d); PPAM3 (e) (B) and PPAC (Ag_2CrO_4) (a); PP (b); PPAC05 (c); PPAC1 (d); PPAC3 (e) (C).

An analysis of the rheological properties was performed to evaluate the interactions between the PP matrix and the semiconductor oxides α -Ag₂WO₄, β -Ag₂MoO₄ and Ag₂CrO₄, as well as the flow behavior. **Figure 3.3** presents the complex viscosity as a function of frequency, whereas **Figure B.3** shows the storage and loss modulus as functions of frequency for all samples. It can be observed that the polymer and the composites have characteristic pseudoplastic flow behavior, as expected. In the region of the Newtonian plateau at low frequencies, there is an increase in complex viscosity compared to the pure PP for all composites. More specifically for the PPAW and PPAC composites, the behavior among the added concentrations (PPAW05, PPAW1 and PPAW3; PPAC05, PPAC1 and PPAC3) is very similar. Regarding the PPAM composite, there is a gradual increase in viscosity as the semiconductor concentration increases, being the viscosity of the composite with 3% of the semiconductor the most viscous (PPAM05 < PPAM1 < PPAM3). The increase in the complex viscosity of the nanocomposites might be associated with the formation of a network-type microstructure that decreases the mobility of the polymer chains.³⁴ With increasing frequency, the complex viscosity of the pure PP and the composites decreases, exhibiting non-Newtonian behavior. At higher frequencies, there is not enough time for the polymer chains to respond to applied different motions, which could justify the unchanged behavior noted.³⁵ The modules G' and G'' increase as functions of frequency, with G'' > G' over most of the present testing range as a signal of the predominant viscous response. Additionally, there is an overlap of curves with similar values for all samples, i.e., the rheological properties remain comparable with the same inclination values. These results represent a low dispersion between the fillers and the PP matrix since a percolation network cannot be observed. The low interaction corroborates the results observed by XRD and FTIR, which indicate that the structure of the PP and the semiconductors is maintained. Therefore, the increase in viscosity is confirmed by the cluster lattice formed in the polymer matrix.

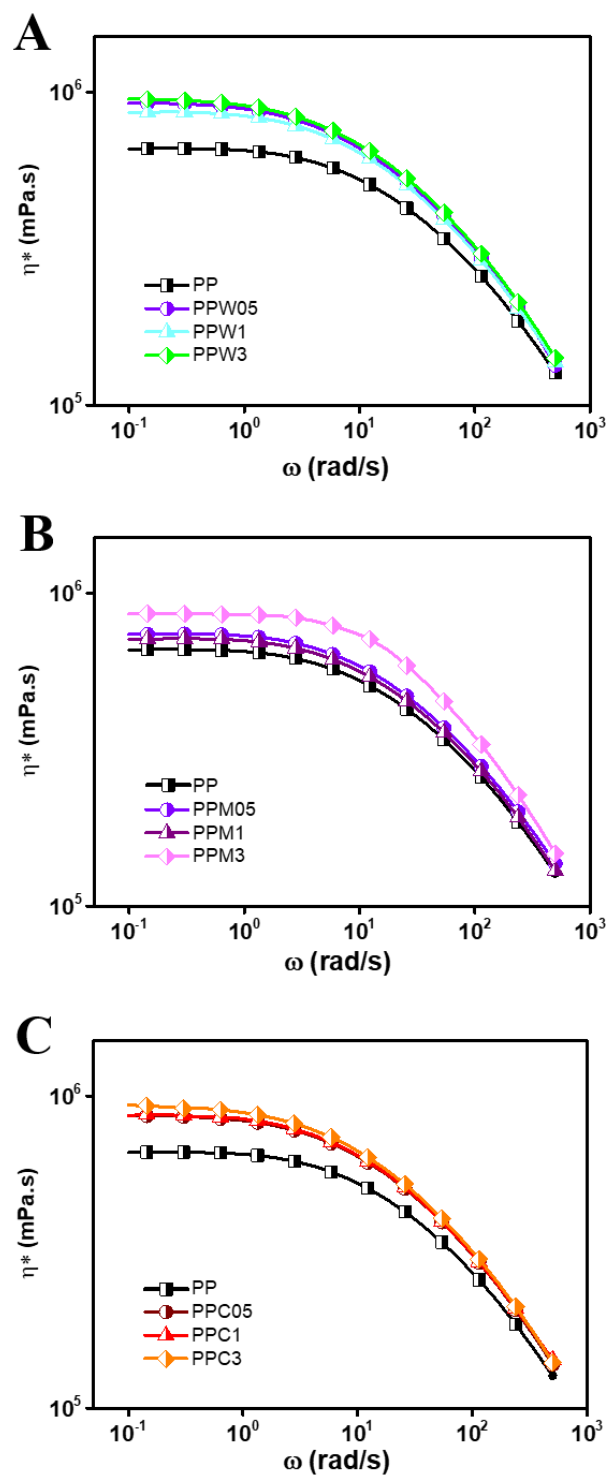


Figure 3.3. Complex viscosity at 190 °C as a function of frequency for (A) PPAW, (B) PPAM and (C) PPAC composites.

PP tensile modulus, tensile strength, strain at break, and glass-transition temperature (T_g) as a function of Ag-based semiconductors content are presented in **Figure 3.4**. In general, an increase in the Ag-particles content promotes a decrease in tensile modulus and tensile strength, and an increase in strain at break. The crystallinity content of PP was not significantly altered with the presence of particles, except for PP composite with 1 wt% of α -Ag₂WO₄. Such findings can be explained by the lack of specific interactions between Ag-particles and PP chains, as previously observed by the rheology results. An increase in strain at break was observed for all samples with Ag-particles when compare to pristine. Moreover, the most significant results are noticed at 1 wt%. In content higher than 1 wt% can occur the aggregation of the particles resulting in a decrease in this property.³⁶ In addition, the decrease in mechanical strength and an increase in strain at break with the incorporation of Ag-particles have already been described in the literature.^{36,37} DSC results also show that, regardless the Ag-based semiconductor, there is an increase in PP T_g with Ag-particles content, reaching the maximum at 1 wt% and decreasing at 3 wt%. In general, the incorporation of Ag-based semiconductors slightly influenced PP mechanical properties, except for strain at break. Nonetheless, the effect of Ag-particles on polyolefine's mechanical properties cannot be directly predicted and there is no consensus in the literature.^{36,38}

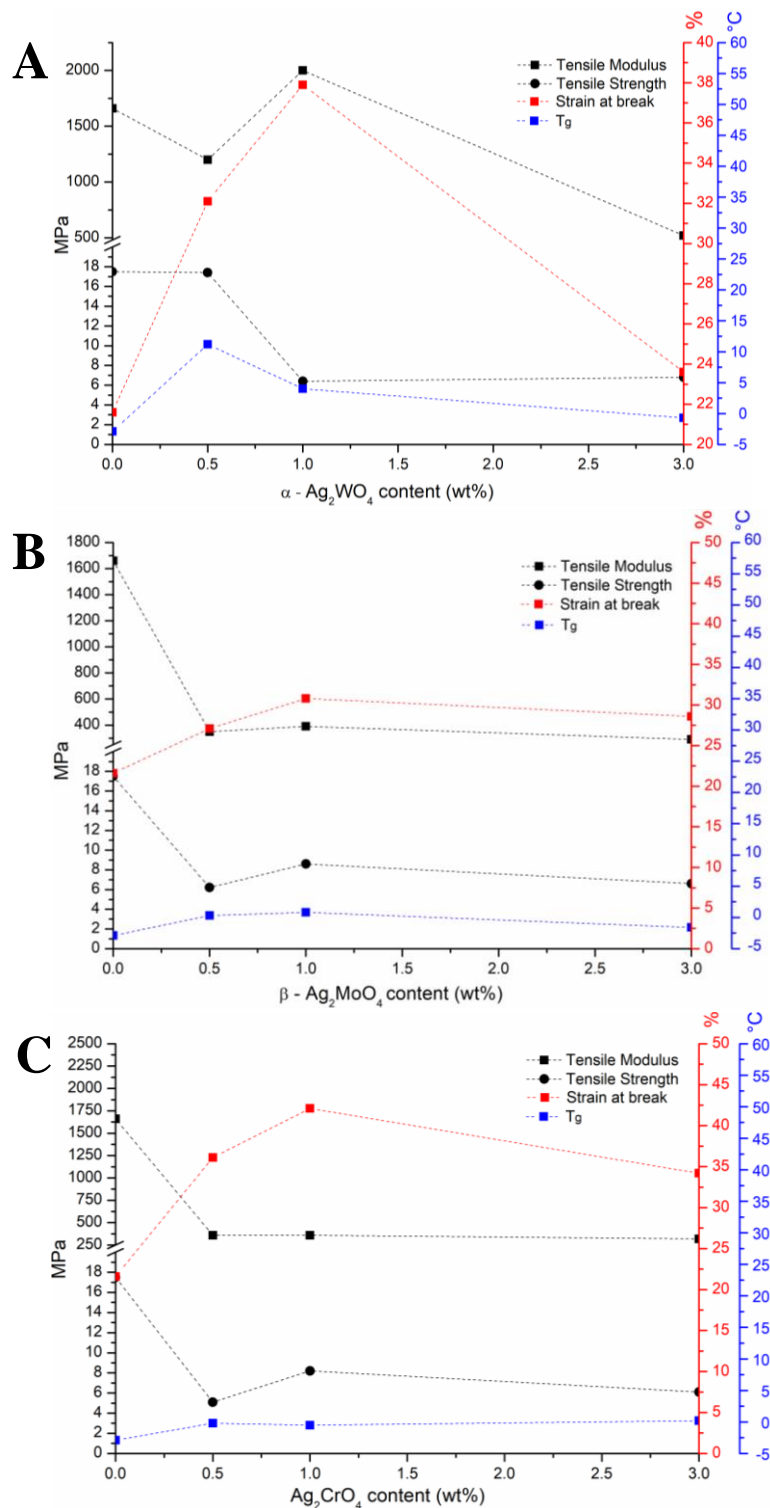


Figure 3.4. Tensile strength, tensile modulus (MPa), strain at Break (%) and glass-transition temperature (T_g) ($^{\circ}$ C) for (a) PPAW, (b) PPAM and (c) PPAC samples.

The AFM images in **Figures B.4-B.6** illustrate the changes in topography after the modification of the polymer matrix with 1% of the different silver-based metal oxides. The metal oxides are characterized by microparticles dispersed on the polymer surface, which is evidenced by the phase-contrast images. However, a uniform dispersion of these microparticles is not observed for any of the added semiconductors, in any of the concentrations. It is believed that the mixing process in the mixing chamber directly affects the uniformity and size of semiconductor particles during the composite production. Due to the presence of scratches and the weak dispersion of particles observed in the AFM analysis, it was difficult to perform an accurate analysis of the changes in the roughness factor of the samples.

Figure B.7 shows the contact angle results for the PPAW, PPAM and PPAC composites and their respective oxide concentrations. As described in the literature, PP is an apolar polymer with hydrophobic surface properties, and according to **Figure B.7** the contact angle of the PP sample is 86° . For the composites, there is an increase in the angle between the surface and the droplet, proving that the addition of the compounds influences their hydrophobic surface property. As a consequence, it becomes more difficult for the microorganisms to adhere to the composite surface.³⁹ Furthermore, there is no direct correlation between the angle and the semiconductor concentration in the PP matrix. As described by Hosseini et al., the formation of a composite with a more hydrophobic surface can inhibit and/or decrease the activities of pathogenic microorganisms due to the reduced interaction between the composite surface and the microorganism.¹²

It is reported that surface microbial encrustation can cause a series of microbial infections due to the contact of the contaminated surface with the host. Since the antimicrobial activity of these semiconductors against a number of different microorganisms is already known,⁴⁰ bacteria (*S. aureus* and *E. coli*) and fungal (*C. albicans*) inactivation tests were carried out by monitoring them from 1 to 24 h for all composites (**Figure 3.5**). For pure PP, an increase in the

number of colonies forming units per mL (CFU/mL) is observed with increasing time. This fact is expected, since once the microorganisms have the minimum conditions to grow, they will. On the other hand, all composites showed a tendency to expressively reduce the amount of CFU/mL of the microorganisms studied as a function of time, in this way, their use can minimize indirect infections arising from contact with surfaces protected with these materials. For the Gram-positive bacterium *S. aureus*, all composites with 3% wt of semiconductors (PPAW3, PPAM3 and PPAC3) showed total clearance in 16 h, while the remaining samples completely eliminated the microorganisms in 24 h of contact, with the exception of PPAM05. For the Gram-negative bacterium *E. coli*, we could observe total elimination within 4 h of exposure for samples PPAW3 and PPAC3, 8 h for sample PPAM3, 16 h for samples PPAW1 and PPAW05 and 24 h for samples PPAM 1 and PPAC1. The distinct antimicrobial activities of the composites in both Gram-positive and Gram-negative bacteria can be attributed to the different constitution of their cell membranes. For the diploid fungus *C. albicans*, only the samples PPAW3, PPAM3 and PPAC3 showed complete elimination in 16 (PPAW3 and PPAC3) and 24 h (PPAM3). The greater difficulty in eliminating the fungus can be explained by its greater cellular complexity. At lower concentrations, these semiconductors can also cause morphological changes, making this yeast assume its pseudohifal form, thus resulting in lower virulence. The antimicrobial tests with bacteria (*S. aureus* and *E. coli*) and fungus (*C. albicans*) were performed for the composites after ultraviolet irradiation y xenon-arc lamp to reproduce the effects of weathering.⁴¹ It was observed that after simulating one year of these effects (600 h of exposure), there was still a similar reduction in the elimination of these microorganisms.

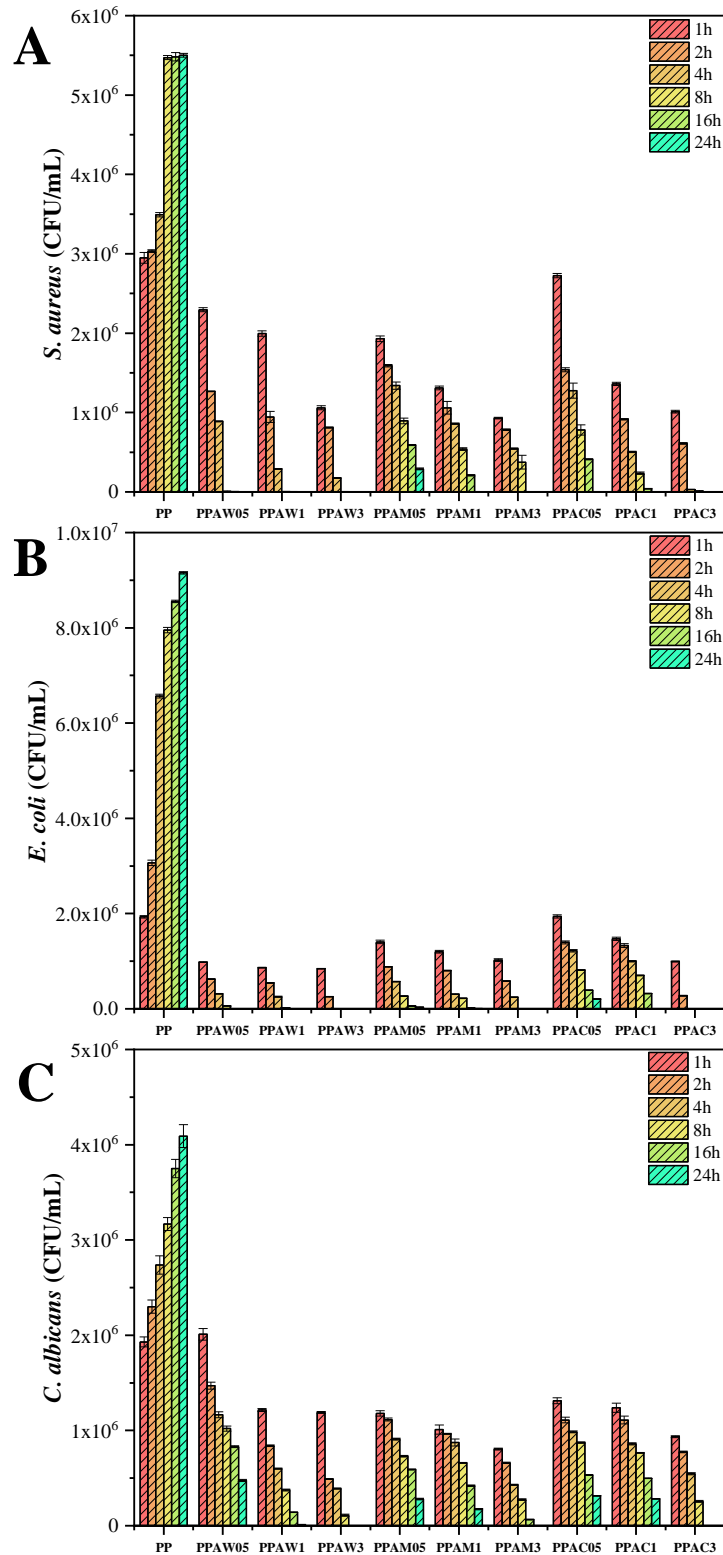


Figure 3.5. Time Kill tests for *S. aureus* using the (A) PPAW, (B) PPAM and (C) PPAC composites, for *E. coli* using the (D) PPAW, (E) PPAM and (F) PPAC

composites and for *C. albicans* using the (G) PPAW, (H) PPAM and (I) PPAC composites.

The observed behavior is due to two intrinsic factors: the chemical composition of the semiconductor and its ability to generate ROS (even in the dark, mimicking the natural conditions). All of these semiconductors are composed of Ag, which has a high oxidizing power and can be toxic in high concentrations. For α -Ag₂WO₄, the biostatic potential of W atoms is also added, which increases the effectiveness of its antimicrobial activity.⁴² α -Ag₂WO₄ still has a structural and enhanced peculiarity, as it is formed by several disordered clusters of [AgO_x] (x = 2, 4, 6 and 7) and [WO₆], providing high electronic and structural asymmetry to the semiconductor in relation to β -Ag₂MoO₄ and Ag₂CrO₄.^{43,44} **Table 3.1** compares the results presented herein with other immobilized materials (in the form of composites and/or coatings) against some fungi and bacteria. The results presented in this work are superior regarding the elimination of microorganisms when we take into account samples with higher concentrations of Ag-based semiconductors.

Table 3.1. Comparative results of inactivation pathogenic microbes (fungi and bacteria) in studies with polymeric materials modified with semiconductors.

Material Modified	Pathogenic Microbes	Percentage of Inactivation (%)	Time-dependent Antimicrobial Activity (min)	Reference
MoS ₂ /polycotton fabrics	<i>E. coli</i>	99.99	720	58
	<i>S. aureus</i>	99.99	720	
Li-TiO ₂ /LDPE Polymer	<i>S. aureus</i>	99	720	59
Ag NPs/PEG/chitosan	<i>E. coli</i>	>90	120	60
	<i>S. aureus</i>	>90	120	
TiO ₂ /conjugated microporous polymer	<i>E. coli</i>	98.14	120	61
	<i>S. aureus</i>	100	120	
Ag ₃ PO ₄ /Polypropylene	<i>E. coli</i>	99.99	250	27
	<i>S. aureus</i>	99.99	4320	
	<i>C. albicans</i>	99	4320	
ZnO/Mersilene™ Meshes	<i>E. coli</i>	63 ±3	1440	62
	<i>S. aureus</i>	72 ±3	1440	
	<i>S. epidermidis</i>	96 ±3	1440	
	<i>C. albicans</i>	85 ±3	1440	
SiO ₂ /Ag/Ethylenevinyl acetate	<i>E. coli</i>	99	1200	3
	<i>S. aureus</i>	99	1200	
SiO ₂ -Ag/ Polyvinyl chloride	<i>E. coli</i>	>99.8	1200	26
	<i>S. aureus</i>	>99.8	1200	
	<i>P. funiculosus</i>	>99.8	1200	
α-Ag ₂ WO ₄ / Polypropylene	<i>E. coli</i>	>99.999	240	
	<i>S. aureus</i>	>99.999	960	
	<i>C. albicans</i>	>99.999	960	
β-Ag ₂ MoO ₄ / Polypropylene	<i>E. coli</i>	>99.999	480	This Work
	<i>S. aureus</i>	>99.999	960	
Ag ₂ CrO ₄ / Polypropylene	<i>C. albicans</i>	>99.999	1440	
	<i>E. coli</i>	>99.999	240	
	<i>S. aureus</i>	>99.999	960	
	<i>C. albicans</i>	>99.999	960	

Once the efficiency in the elimination of more complex microorganisms such as fungi and bacteria were verified, tests for the elimination of SARS-CoV-2 were carried out after 10 min of virus exposure to the surface of the composites (**Figure 3.6A**). For all composites, there was a reduction of more than 98% of genetic copies of SARS-CoV-2, and this elimination was even higher when the semiconductor concentration in the polymer matrix was increased. For the PPAW and PPAM composites, similar antiviral activities were observed at all concentrations, while the PPAC composite showed a slightly lower elimination. The stability of the antiviral activity was tested by performing consecutive tests on the same polymeric body for 5 consecutive days (**Figure 3.6B**). On all occasions it was possible to observe values very close to the elimination of SARS-CoV-2, showing us that the antiviral activity of the composites was preserved. When the SARS-CoV-2 elimination results shown here are compared with those reported in the literature (**Table 3.2**), it can be concluded that they are comparable and often better than those already published since the elimination time is shorter (10 min) and the antiviral elimination is highly efficient.

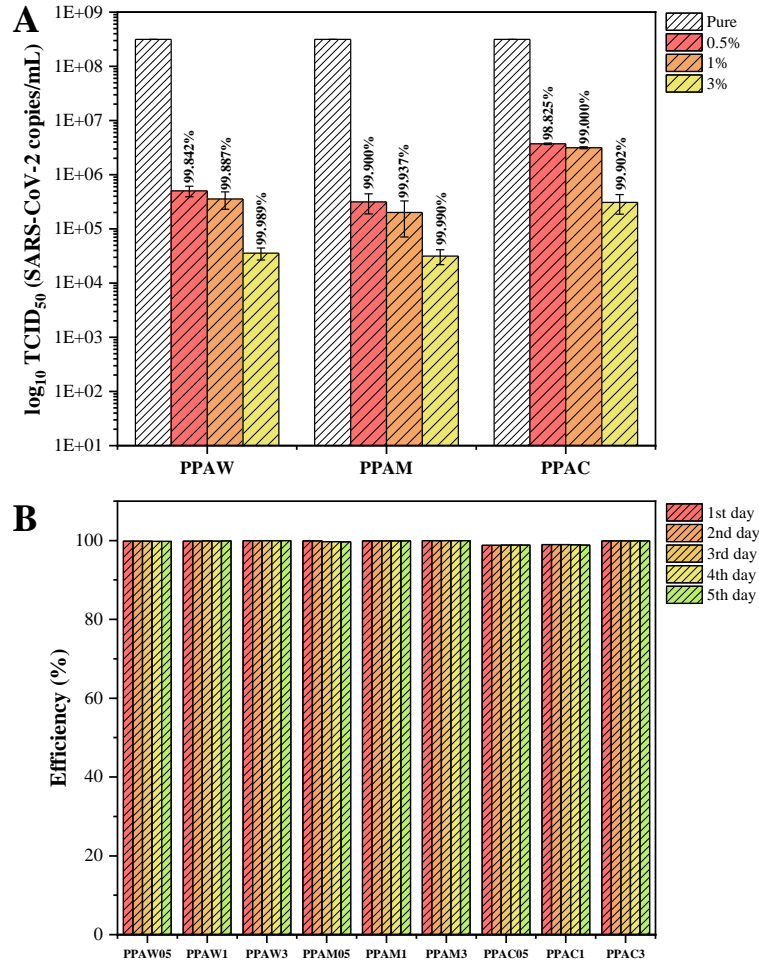


Figure 3.6. (A) Determination of viral titer (\log_{10} TCID₅₀) after 10 minutes of contact of treated plastic film samples in relation to the positive viral control, comparing the mean of the replicates between the values arising from different exposures of the material. (B) Stability of anti-SARS-CoV-2 activity for 5 consecutive days.

Table 3.2. Determination of percentage of inactivation of SARS-CoV-2 and reduction based on \log_{10} TCID₅₀ method for 5 consecutive days.

Material Modified	Percentage of Inactivation (%)	Time-dependent Virucide Activity (min)	Reference
Ag ₃ PO ₄ /Polypropylene	>90	5	27
SiO ₂ -Ag/Ethylene-vinyl acetate	99	2	3
SiO ₂ -Ag/ Polyvinyl chloride	>99.8	15	26
Cu ₂ O/ Polyurethane	99.99	120	12
TiO ₂ / Ceramic tiles	>99	300	63
CuO/ Coating	99.9	60	13
CuS/ Mask	80	5-10	64
ZnO/ Polyurethane	>99.9	60	65
α -Ag ₂ WO ₄ / Polypropylene	>99.9	10	
Ag ₂ MoO ₄ / Polypropylene	>99.99	10	This work
Ag ₂ CrO ₄ / Polypropylene	>99.9	10	

The elimination of these microorganisms (bacteria, fungi and viruses) occurs due to the generation of reactive oxygen species (ROS) in the semiconductor, even in the dark.^{3,26,27} When interacting with propylene groups, different semiconductors such as Ag₂XO₄ (X = W, Mo and Cr) can have their electronic density in the conduction band (CB) increased. This transfer of electrons (e^-) from polypropylene increases the reducing character of the semiconductor. The semiconductor interacts with O₂ exothermically in the CB, either causing the excited e^- to be located in the forbidden region of the band gap, resulting in a superoxide radical ($\bullet O_2^-$), or losing one e^- , forming a singlet oxygen (1O_2). As a result, there is the release of a hole (h^+) that interacts with

H₂O through the formation of a hydroxyl radical ($\bullet\text{OH}$) and a proton (H^+). On the other hand, the released H^+ in the valence band (VB) interacts with ($\bullet\text{O}_2^-$), which in turn reacts by forming the hydroperoxyl radical ($\bullet\text{OOH}$).²⁷ In previous works it was possible to identify through scavenger tests that these ROS are responsible for the antimicrobial and photocatalytic activity of $\alpha\text{-Ag}_2\text{WO}_4$, $\beta\text{-Ag}_2\text{MoO}_4$ and Ag_2CrO_4 .^{40,45,46} These ROS generated by Ag_2XO_4 ($\text{X} = \text{W}, \text{Mo}$ and Cr) semiconductors can interact with lipids, nucleic acids, proteins and other components, causing the death of these microorganisms.⁴⁷ In addition, ROS can interact with polyunsaturated fatty acids of the microbial membranes, initiating their lipid peroxidation.^{48,49} As a consequence, there is a decrease in their fluidity and the formation of other products (such as aldehydes), which in turn change their protein composition, contributing to microbial death.^{50,51} Another target of ROS is to induce single and double DNA/RNA strand breaks to impair and/or inactivate replication processes as expected.⁵² The action of ROS can also be combined with the effect of Ag^+ ions, which can interact with DNA phosphorus centers, resulting in replication difficulties.⁵³ Additionally, proteins that have sulfur or phosphorus in their composition can be altered, having their enzymatic functions inhibited.^{54,55} Similarly, Ag^+ ions can also alter the mitochondrial properties of these microorganisms.⁵⁶ Regarding viral activity, Ag^+ ions can interact with proteins that compose the viral envelope, preventing its interaction with new host cells, and consequently its replication processes.⁵⁷ These processes are summarized in **Figure 3.7**.

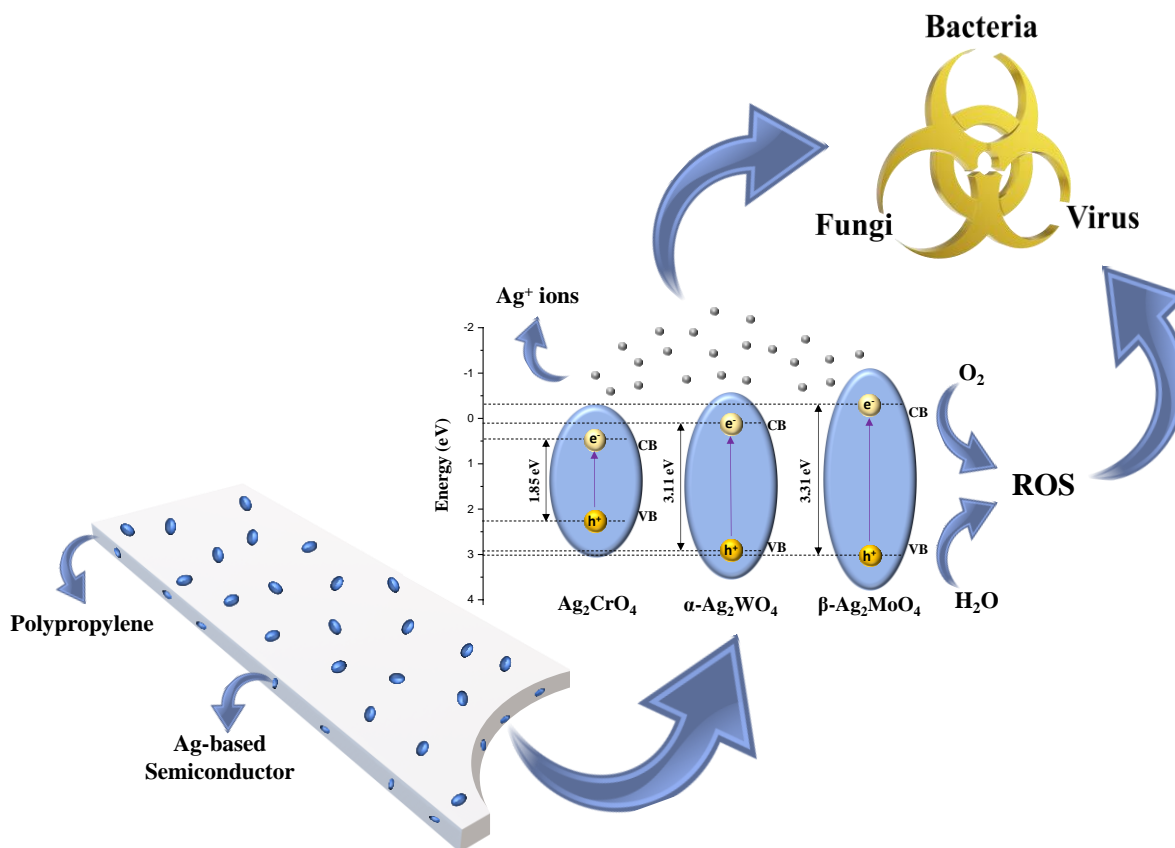


Figure 3.7. Mechanisms of antimicrobial action of semiconductors encapsulated in polymeric matrix (CB and VB represent the conduction band and valence band, respectively).

3.4. Conclusions

Infections caused by COVID-19 and other bacteria and fungi are of growing public concern. Therefore, the design and development of new antimicrobial agents with a broad spectrum of activity have become essential to combat the increasing and varied threats from microorganisms. In this work we described a method for rapidly preparing composites of $\alpha\text{-Ag}_2\text{WO}_4$, $\beta\text{-Ag}_2\text{MoO}_4$ and Ag_2CrO_4 with PP in the amounts of 0.5, 1 and 3% wt using relatively inexpensive and safe materials. These composites proved to be highly effective against important bacterial pathogens (*E. coli* and *S. aureus*) and fungus (*C. albicans*), besides successfully inactivating SARS-CoV-2. For this reason, we

suggest their application on common use objects to reduce the spread of microbial diseases. There is no doubt that these composites can play a prominent role in the fight against resistant bacteria, fungi and viruses, thereby improving the prevention of infections. The preparation of materials can create new green synthesis approaches, and their selection can be done based on tunable and durable properties. Their use depends on overall performance and economic assessment, which need further optimization in terms of robust conditions and the use of new hybrid materials for coatings. This potential to contribute to the worldwide efforts to fight emerging viral infections.

3.5. References

- (1) Prather, K. A.; Wang, C. C.; Schooley, R. T. Reducing Transmission of SARS-CoV-2. *Science* 2020, 6498, 1422–1424.
- (2) Chin, A. W. H.; Chu, J. T. S.; Perera, M. R. A.; Hui, K. P. Y.; Yen, H.-L.; Chan, M. C. W.; Peiris, M.; Poon, L. L. M. Stability of SARS-CoV-2 in Different Environmental Conditions. *Lancet Microbe* 2020, 1, No. e10.
- (3) Assis, M.; Simoes, L. G. P.; Tremiliosi, G. C.; Coelho, D.; Minozzi, D. T.; Santos, R. I.; Vilela, D. C. B.; Santos, J. R. d.; Ribeiro, L. K.; Rosa, I. L. V.; Mascaro, L. H.; Andrés, J.; Longo, E. SiO₂-Ag Composite as a Highly Virucidal Material: A Roadmap That Rapidly Eliminates SARS-CoV-2. *Nanomaterials* 2021, 11, 638.
- (4) Zhang, D. X. SARS-CoV-2: Air/Aerosols and Surfaces in Laboratory and Clinical Settings. *J. Hosp. Infect.* 2020, 105, 577–579.
- (5) Andersen, K. G.; Rambaut, A.; Lipkin, W. I.; Holmes, E. C.; Garry, R. F. The Proximal Origin of SARS-CoV-2. *Nat. Med.* 2020, 26, 450–452.
- (6) Pedersen, S. F.; Ho, Y.-C. SARS-CoV-2: A Storm Is Raging. *J. Clin. Invest.* 2020, 130, 2202–2205.
- (7) Rai, M.; Bonde, S.; Yadav, A.; Bhowmik, A.; Rathod, S.; Ingle, P.; Gade, A. Nanotechnology as a Shield against COVID-19: Current Advancement and Limitations. *Viruses* 2021, 13, 1224.
- (8) Shirvanimoghaddam, K.; Akbari, M. K.; Yadav, R.; Al-Tamimi, A. K.; Naebe, M. Fight against COVID-19: The Case of Antiviral Surfaces. *APL Mater.* 2021, 9, 31112.
- (9) van Doremalen, N.; Bushmaker, T.; Morris, D. H.; Holbrook, M. G.; Gamble, A.; Williamson, B. N.; Tamin, A.; Harcourt, J. L.; Thornburg, N. J.; Gerber, S. I.; Lloyd-Smith, J. O.; de Wit, E.; Munster, V. J. Aerosol and Surface Stability of SARS-CoV-2 as Compared with SARS-CoV-1. *Nejm* 2020, 382, 1564–1567.

- (10) Tian, F.; Chen, L.; Xu, X. Dynamical Mechanical Properties of Wood-High Density Polyethylene Composites Filled with Recycled Rubber. *J. Bioresour. Bioprod.* 2021, 6, 152–159.
- (11) de Lima, J. A.; Fitaroni, L. B.; Waldman, W. R.; Cruz, S. A. Compatibilizer Prevents the Catalytic Role of Sepiolite in the Thermal Degradation of PP/Sep Nanocomposites. *J. Therm. Anal. Calorim.* 2021, 146, 2481–2487.
- (12) Hernández-Jiménez, J. A.; Jiménez-Amezcuca, R. M.; Lomelí-Ramírez, M. G.; Silva-Guzmán, J. A.; Torres-Rendón, J. G.; García-Enriquez, S. Utilization of Wood Flour from White Oak Branches as Reinforcement in a Polypropylene Matrix: Physical and Mechanical Characterization. *J. Compos. Sci.* 2022, 6, 184.
- (13) Dixit, S.; Mishra, G.; Yadav, V. L. Optimization of Novel Bio-Composite Packaging Film Based on Alkali-Treated Hemp Fiber/ Polyethylene/Polypropylene Using Response Surface Methodology Approach. *Polym. Bull.* 2022, 79, 2559–2583.
- (14) Seo, H. Y.; Cho, K. Y.; Im, D.; Kwon, Y. J.; Shon, M.; Baek, K.- Y.; Yoon, H. G. High Mechanical Properties of Covalently Functionalized Carbon Fiber and Polypropylene Composites by Enhanced Interfacial Adhesion Derived from Rationally Designed Polymer Compatibilizers. *Compos. Part B Eng.* 2022, 228, No. 109439.
- (15) Mouritz, A. P.; Galos, J.; Linklater, D. P.; Ladani, R. B.; Kandare, E.; Crawford, R. J.; Ivanova, E. P. Towards Antiviral Polymer Composites to Combat COVID-19 Transmission. *Nano Sel.* 2021, 2, 2061–2071.
- (16) Fadare, O. O.; Okoffo, E. D. Covid-19 Face Masks: A Potential Source of Microplastic Fibers in the Environment. *Sci. Total Environ.* 2020, 737, No. 140279.
- (17) Deng, C.; Seidi, F.; Yong, Q.; Jin, X.; Li, C.; Zheng, L.; Yuan, Z.; Xiao, H. Virucidal and Biodegradable Specialty Cellulose Nonwovens as Personal Protective Equipment against COVID-19 Pandemic. *J. Adv. Res.* 2022, 39, 147–156.
- (18) Madej-Kiełbik, L.; Gzyra-Jagięła, K.; Jóźwik-Pruska, J.; Wisniewskia-Wrona, M.; Dymel, M. Biodegradable Nonwoven Materials with Antipathogenic Layer. *Environments* 2022, 9, 79.
- (19) Khan, J.; Momin, S. A.; Mariatti, M.; Vilay, V.; Todo, M. Recent Advancements in Nonwoven Bio-Degradable Facemasks to Ameliorate the Post-Pandemic Environmental Impact. *Mater. Res. Express* 2021, 8, No. 112001.
- (20) Sanghi, R.; Verma, P. Biomimetic Synthesis and Characterisation of Protein Capped Silver Nanoparticles. *Bioresour. Technol.* 2009, 100, 501–504.
- (21) Behzadinasab, S.; Chin, A.; Hosseini, M.; Poon, L.; Ducker, W. A. A Surface Coating That Rapidly Inactivates SARS-CoV-2. *ACS Appl. Mater. Interfaces* 2020, 12, 34723–34727.

- (22) Hosseini, M.; Chin, A. W. H.; Behzadinasab, S.; Poon, L. L. M.; Ducker, W. A. Cupric Oxide Coating That Rapidly Reduces Infection by SARS-CoV-2 via Solids. *ACS Appl. Mater. Interfaces* 2021, 13, 5919–5928.
- (23) Abo-zeid, Y.; Ismail, N. S. M.; McLean, G. R.; Hamdy, N. M. A Molecular Docking Study Repurposes FDA Approved Iron Oxide Nanoparticles to Treat and Control COVID-19 Infection. *Eur. J. Pharm. Sci.* 2020, 153, No. 105465.
- (24) Tavakoli, A.; Ataei-Pirkooh, A.; MM Sadeghi, G.; Bokharaei Salim, F.; Sahrapour, P.; Kiani, S. J.; Moghoofei, M.; Farahmand, M.; Javanmard, D.; Monavari, S. H. Polyethylene Glycol-Coated Zinc Oxide Nanoparticle: An Efficient Nanoweapon to Fight against Herpes Simplex Virus Type 1. *Nanomedicine* 2018, 13, 2675–2690.
- (25) Mlcochova, P.; Chadha, A.; Hesselhoj, T.; Fraternali, F.; Ramsden, J. J.; Gupta, R. K. Extended in Vitro Inactivation of SARS-CoV-2 by Titanium Dioxide Surface Coating. *bioRxiv* 2020, DOI: 10.1101/2020.12.08.415018.
- (26) Jeremiah, S. S.; Miyakawa, K.; Morita, T.; Yamaoka, Y.; Ryo, A. Potent Antiviral Effect of Silver Nanoparticles on SARS-CoV-2. *Biochem. Biophys. Res. Commun.* 2020, 533, 195–200.
- (27) Pandey, A.; Nikam, A. N.; Mutalik, S. P.; Fernandes, G.; Shreya, A. B.; Padya, B. S.; Raychaudhuri, R.; Kulkarni, S.; Prassl, R.; Subramanian, S.; Korde, A.; Mutalik, S. Architected Therapeutic and Diagnostic Nanoplatfoms for Combating SARS-CoV-2: Role of Inorganic, Organic, and Radioactive Materials. *ACS Biomater. Sci. Eng.* 2021, 7, 31–54.
- (28) Bui, T. Q.; Phuong Loan, H. T.; Ai My, T. T.; Quang, D. T.; Phuong Thuy, B. T.; Nhan, V. D.; Quy, P. T.; Van Tat, P.; Dao, D. Q.; Trung, N. T.; Huynh, L. K.; Ai Nhung, N. T. A Density Functional Theory Study on Silver and Bis-Silver Complexes with Lighter Tetrylene: Are Silver and Bis-Silver Carbenes Candidates for SARS-CoV-2 Inhibition Insight from Molecular Docking Simulation. *RSC Adv.* 2020, 10, 30961–30974.
- (29) De Maio, F.; Palmieri, V.; Babini, G.; Augello, A.; Palucci, I.; Perini, G.; Salustri, A.; De Spirito, M.; Sanguinetti, M.; Delogu, G.; Rizzi, L. G.; Cesareo, G.; Soon-Shiong, P.; Sali, M.; Papi, M. Graphene Nanoplatelet and Graphene Oxide Functionalization of Face Mask Materials Inhibits Infectivity of Trapped SARS-CoV-2. *medRxiv* 2020, No. 102788.
- (30) Milewska, A.; Chi, Y.; Szczepanski, A.; Barreto-Duran, E.; Dabrowska, A.; Botwina, P.; Obloza, M.; Liu, K.; Liu, D.; Guo, X.; Ge, Y.; Li, J.; Cui, L.; Ochman, M.; Urlik, M.; Rodziewicz-Motowidlo, S.; Zhu, F.; Szczubialka, K.; Nowakowska, M.; Pyrc, K. HTCC as a Polymeric Inhibitor of SARS-CoV-2 and MERS-CoV. *J. Virol.* 2021, 95, e01622–e01620.
- (31) Lara, H. H.; Ayala-Nuñez, N. V.; Ixtepan-Turrent, L.; Rodriguez-Padilla, C. Mode of Antiviral Action of Silver Nanoparticles against HIV-1. *J. Nanobiotechnology* 2010, 8, 1–10.

- (32) Gaikwad, S.; Ingle, A.; Gade, A.; Rai, M.; Falanga, A.; Incoronato, N.; Russo, L.; Galdiero, S.; Galdiero, M. Antiviral Activity of Mycosynthesized Silver Nanoparticles against Herpes Simplex Virus and Human Parainfluenza Virus Type 3. *Int. J. Nanomed.* 2013, 8, 4303–4314.
- (33) Speshock, J. L.; Murdock, R. C.; Braydich-Stolle, L. K.; Schrand, A. M.; Hussain, S. M. Interaction of Silver Nanoparticles with Tacaribe Virus. *J. Nanobiotechnology* 2010, 8, 1–9.
- (34) Tremiliosi, G. C.; Simoes, L. G. P.; Mi, D. T.; Santos, R. I.; Vilela, D. C. B.; Durigon, E. L.; Machado, R. R. G.; Sales-medina, D. F.; Alexandre, C.; Ribeiro, L. K.; Rosa, I. L. V.; Assis, M.; Andrés, J.; Longo, E.; Freitas-junior, L. H. Ag nanoparticles-based antimicrobial polycotton fabrics to prevent the transmission and spread of SARS-CoV-2. *bioRxiv* 2020, DOI: 10.1101/2020.06.26.152520
- (35) Assis, M.; Simoes, L. G. P.; Tremiliosi, G. C.; Ribeiro, L. K.; Coelho, D.; Minozzi, D. T.; Santos, R. I.; Vilela, D. C. B.; Mascaro, L. H.; Andrés, J.; Longo, E. PVC-SiO₂-Ag Composite as a Powerful Biocide and Anti-SARS-CoV-2 Material. *J. Polym. Res.* 2021, 28, 361.
- (36) Ribeiro, L. K.; Assis, M.; Lima, L. R.; Coelho, D.; Gonçalves, M. O.; Paiva, R. S.; Moraes, L. N.; Almeida, L. F.; Lipsky, F.; San-Miguel, M. A.; Mascaro, L. H.; Grotto, R. M. T.; Sousa, C. P.; Rosa, I. L. V.; Cruz, S. A.; Andrés, J.; Longo, E. Bioactive Ag₃PO₄/ Polypropylene Composites for Inactivation of SARS-CoV-2 and Other Important Public Health Pathogens. *J. Phys. Chem. B* 2021, 125, 10866–10875.
- (37) Miller, J.; Ulrich, R. On the Analysis of Psychometric Functions: The Spearman-Kärber Method. *Percept. Psychophys.* 2001, 63, 1399–1420.
- (38) Reed, L. J.; Muench, H. A simple method of estimating fifty per cent endpoints. *Am. J. Epidemiol.* 1938, 27, 493–497.
- (39) Oliani, W. L.; Parra, D. F.; Fermino, D. M.; Riella, H. G.; Lima, L. F. C. P.; Lugao, A. B. Study of Gel Formation by Ionizing Radiation in Polypropylene. *Radiat. Phys. Chem.* 2013, 84, 20–25.
- (40) Akinci, A.; Akbulut, H.; Yilmaz, F. The Effect of the Red Mud on Polymer Crystallization and the Interaction between the Polymer Filler. *Polym. - Plast. Technol. Eng.* 2007, 46, 31–36.
- (41) Prasert, A.; Sontikaew, S.; Sriprapai, D.; Chuangchote, S. Polypropylene/ZnO Nanocomposites: Mechanical Properties, Photocatalytic Dye Degradation, and Antibacterial Property. *Materials (Basel)*. 2020, 13, 1–16.
- (42) Assis, M.; Pontes Ribeiro, R. A.; Carvalho, M. H.; Teixeira, M. M.; Gobato, Y. G.; Prando, G. A.; Mendonça, C. R.; de Boni, L.; Aparecido de Oliveira, A. J.; Bettini, J.; Andrés, J.; Longo, E. Unconventional Magnetization Generated from Electron Beam and Femtosecond Irradiation on α -Ag₂WO₄: A Quantum Chemical Investigation. *ACS Omega* 2020, 5, 10052–10067.

- (43) Lemos, P. S.; Silva, G. S.; Roca, R. A.; Assis, M. D.; Torres-Mendieta, R.; Beltrán-Mir, H.; Mínguez-Vega, G.; Cordoncillo, E.; Andrés, J.; Longo, E. Laser and Electron Beam-Induced Formation of Ag/Cr Structures on Ag₂CrO₄. *Phys. Chem. Chem. Phys.* 2019, 21, 6101–6111.
- (44) De Foggi, C. C.; De Oliveira, R. C.; Assis, M.; Fabbro, M. T.; Mastelaro, V. R.; Vergani, C. E.; Gracia, L.; Andres, J.; Longo, E.; Machado, A. L. Unveiling the Role of β -Ag₂MoO₄ Microcrystals to the Improvement of Antibacterial Activity. *Mater. Sci. Eng. C* 2020, No. 110765.
- (45) Báez, M. A.; Hendra, P. J.; Judkins, M. The Raman Spectra of Oriented Isotactic Polypropylene. *Spectrochim. Acta - Part A Mol. Biomol. Spectrosc.* 1995, 8539, 2117–2124.
- (46) Linares Veliz, A. B.; Jiménez García, J.; López, P.; de Gáscue, B. Biodegradability Study by FTIR and DSC of Polymers Films Based on Polypropylene and Cassava Starch. *Orbital Electron. J. Chem.* 2019, 11, 2117–2124.
- (47) Panthi, G.; Park, S. J.; Chae, S. H.; Kim, T. W.; Chung, H. J.; Hong, S. T.; Park, M.; Kim, H. Y. Immobilization of Ag₃PO₄ Nanoparticles on Electrospun PAN Nanofibers via Surface Oximation: Bifunctional Composite Membrane with Enhanced Photocatalytic and Antimicrobial Activities. *J. Ind. Eng. Chem.* 2017, 45, 277–286.
- (48) Jiang, X.; Liu, X.; Chen, Q.; Jin, R.; Lu, Y.; Yu, J.; Wu, Y.; He, Y. Preparation and Photocatalytic Activity of an Inorganic–Organic Hybrid Photocatalyst Ag₂WO₄/g-C₃N₄. *J. Inorg. Organomet. Polym. Mater.* 2017, 27, 1683–1693.
- (49) Mehraj, O.; Sofi, F. A.; Moosvi, S. K.; Naqash, W.; Majid, K. Synthesis of Novel Silver Chromate Incorporated Copper-MetalOrganic Framework Composites with Exceptionally High Photocatalytic Activity and Stability. *J. Mater. Sci.: Mater. Electron.* 2018, 29, 3358–3369.
- (50) Kaffashi, B.; Davoodi, S.; Oliaei, E. Poly(ϵ -Caprolactone)/ Triclosan Loaded Polylactic Acid Nanoparticles Composite: A Long-Term Antibacterial Bionanocomposite with Sustained Release. *Int. J. Pharm.* 2016, 508, 10–21.
- (51) Davachi, S. M.; Heidari, B. S.; Sahraeian, R.; Abbaspourrad, A. The Effect of Nanoperlite and Its Silane Treatment on the Crystallinity, Rheological, Optical, and Surface Properties of Polypropylene/Nanoperlite Nanocomposite Films. *Compos. B Eng.* 2019, 175, No. 107088.
- (52) Ashraf, M. A.; Peng, W.; Zare, Y.; Rhee, K. Y. Effects of Size and Aggregation/Agglomeration of Nanoparticles on the Interfacial/ Interphase Properties and Tensile Strength of Polymer Nanocomposites. *Nanoscale Res. Lett.* 2018, 13, 214.
- (53) Jo, Y.; Garcia, C. V.; Ko, S.; Lee, W.; Shin, G. H.; Choi, J. C.; Park, S.-J.; Kim, J. T. Characterization and Antibacterial Properties of Nanosilver-Applied

- Polyethylene and Polypropylene Composite Films for Food Packaging Applications. *Food Biosci.* 2018, 23, 83–90.
- (54) Kanmani, P.; Rhim, J.-W. Physicochemical Properties of Gelatin/Silver Nanoparticle Antimicrobial Composite Films. *Food Chem.* 2014, 148, 162–169.
- (55) Jang, M. W.; Kim, J.-Y.; Ihn, K. J. Properties of Polypropylene Nanocomposites Containing Silver Nanoparticles. *J. Nanosci. Nano technol.* 2007, 7, 3990–3994.
- (56) Chibowski, E.; Terpilowski, K. Applied Surface Science Surface Free Energy of Polypropylene and Polycarbonate Solidifying at Different Solid Surfaces. *Appl. Surf. Sci.* 2009, 256, 1573–1581.
- (57) Assis, M.; de Foggi, C. C.; Teodoro, V.; da Costa, J. P. D. C.; Silva, C. E.; Robeldo, T.; Caperucci, P. F.; Vergani, C. E.; Borra, R. C.; Sorribes, I.; Gouveia, A. F.; San-Miguel, M. A.; Andrés, J.; Longo, E. Surface-Dependent Photocatalytic and Biological Activities of Ag₂CrO₄: Integration of Experiment and Simulation. *Appl. Surf. Sci.* 2021, 545, No. 148964.
- (58) ISO. ISO 4892-2:2013 Plastics Methods of Exposure to Laboratory Light Sources Part 2: Xenon-arc Lamps; ISO: Geneva, Switzerland, 2013.
- (59) Longo, V. M.; De Foggi, C. C.; Ferrer, M. M.; Gouveia, A. F.; André, R. S.; Avansi, W.; Vergani, C. E.; Machado, A. L.; Andrés, J.; Cavalcante, L. S.; Hernandez, A. C.; Longo, E. Potentiated Electron Transference in α -Ag₂WO₄ Microcrystals with Ag Nanofilaments as Microbial Agent. *J. Phys. Chem. A* 2014, 118, 5769–5778.
- (60) Assis, M.; Ponce, M. A.; Gouveia, A. F.; Souza, D.; da Costa, J. P. d. C.; Teodoro, V.; Gobato, Y. G.; Andrés, J.; Macchi, C.; Somoza, A.; Longo, E. Revealing the Nature of Defects in α -Ag₂WO₄ by Positron Annihilation Lifetime Spectroscopy: A Joint Experimental and Theoretical Study. *Cryst. Growth Des.* 2021, 21, 1093–1102.
- (61) Foggi, C. C.; Fabbro, M. T.; Santos, L. P. S.; de Santana, Y. V. B.; Vergani, C. E.; Machado, A. L.; Cordoncillo, E.; Andrés, J.; Longo, E. Synthesis and Evaluation of α -Ag₂WO₄ as Novel Antifungal Agent. *Chem. Phys. Lett.* 2017, 674, 125–129.
- (62) Assis, M.; Robeldo, T.; Foggi, C. C.; Kubo, A. M.; Mínguez-Vega, G.; Condoncillo, E.; Beltran-Mir, H.; Torres-Mendieta, R.; Andrés, J.; Oliva, M.; Vergani, C. E.; Barbugli, P. A.; Camargo, E. R.; Borra, R. C.; Longo, E. Ag Nanoparticles/ α -Ag₂WO₄ Composite Formed by Electron Beam and Femtosecond Irradiation as Potent Antifungal and Antitumor Agents. *Sci. Rep.* 2019, 9, 9927.
- (63) Pimentel, B. N. A. S.; Marin-Sett, F. H.; Assis, M.; Carcugli, P. A.; Longo, E.; Vergani, C. E. Antifungal Activity and Biocompatibility of α -AgVO₃, α -Ag₂WO₄, and β -Ag₂MoO₄ Using a Three-Dimensional Coculture Model of the Oral Mucosa. *Front. Bioeng. Biotechnol.* 2022, 10, No. 826123.

- (64) Quinteros, M. A.; Cano Aristizábal, V.; Dalmasso, P. R.; Paraje, M. G.; Páez, P. L. Oxidative Stress Generation of Silver Nanoparticles in Three Bacterial Genera and Its Relationship with the Antimicrobial Activity. *Toxicol. Vitro*. 2016, 36, 216–223.
- (65) Liu, B.; Xue, Y.; Zhang, J.; Han, B.; Zhang, J.; Suo, X.; Mu, L.; Shi, H. Visible-Light-Driven TiO₂/Ag₃PO₄ Heterostructures with Enhanced Antifungal Activity against Agricultural Pathogenic Fungi *Fusarium Graminearum* and Mechanism Insight. *Environ. Sci. Nano* 2017, 4, 255–264.
- (66) Hamblin, M. R. Antimicrobial Photodynamic Inactivation: A Bright New Technique to Kill Resistant Microbes. *Curr. Opin. Microbiol.* 2016, 33, 67–73.
- (67) Gherasim, O.; Puiu, R. A.; Birca, A. C.; Burdusel, A. C.; Grumezescu, A. M. An Updated Review on Silver Nanoparticles in Biomedicine. *Nanomaterials* 2020, 10, 2318.
- (68) Hirayama, J.; Wagner, S. J.; Abe, H.; Ikebuchi, K.; Ikeda, H. Involvement of Reactive Oxygen Species in Hemoglobin Oxidation and Virus Inactivation by 1,9-Dimethylmethylene Blue Phototreatment. *Biol. Pharm. Bull.* 2001, 24, 418–421.
- (69) Yin, I. X.; Zhang, J.; Zhao, I. S.; Mei, M. L.; Li, Q.; Chu, C. H. The Antibacterial Mechanism of Silver Nanoparticles and Its Application in Dentistry. *Int. J. Nanomed.* 2020, Volume 15, 2555– 2562.
- (70) Slavin, Y. N.; Asnis, J.; Häfeli, U. O.; Bach, H. Metal Nanoparticles: Understanding the Mechanisms behind Antibacterial Activity. *J. Nanobiotechnology* 2017, 15, 65.
- (71) Akbarzadeh, A.; Kafshdooz, L.; Razban, Z.; Dastranj Tbrizi, A.; Rasoulpour, S.; Khalilov, R.; Kavetsky, T.; Saghfi, S.; Nasibova, A. N.; Kaamyabi, S.; Kafshdooz, T. An Overview Application of Silver Nanoparticles in Inhibition of Herpes Simplex Virus. *Artif. Cells, Nanomedicine, Biotechnol.* 2018, 46, 263–267.
- (72) Liao, C.; Li, Y.; Tjong, S. Bactericidal and Cytotoxic Properties of Silver Nanoparticles. *Int. J. Mol. Sci.* 2019, 20, 449.
- (73) Kumar, P.; Roy, S.; Sarkar, A.; Jaiswal, A. Reusable MoS₂- Modified Antibacterial Fabrics with Photothermal Disinfection Properties for Repurposing of Personal Protective Masks. *ACS Appl. Mater. Interfaces* 2021, 13, 12912–12927.
- (74) Basiron, N.; Sreekantan, S.; Akil, H. M.; Saharudin, K. A.; Harun, N. H.; Mydin, R. B. S. M. N.; Seeni, A.; Rahman, N. R. A.; Adam, F.; Iqbal, A.; Kumaravel, V. Effect of Li-TiO₂ Nanoparticles Incorporation in LDPE Polymer Nanocomposites for Biocidal Activity. *Nano-Struct. Nano-Objects* 2019, 19, No. 100359.
- (75) Liu, G.; Li, K.; Luo, Q.; Wang, H.; Zhang, Z. PEGylated Chitosan Protected Silver Nanoparticles as Water-Borne Coating for Leather with Antibacterial Property. *J. Colloid Interface Sci.* 2017, 490, 642–651.

- (76) Wu, Y.; Zang, Y.; Xu, L.; Wang, J.; Jia, H.; Miao, F. Synthesis of High-Performance Conjugated Microporous Polymer/TiO₂ Photo catalytic Antibacterial Nanocomposites. *Mater. Sci. Eng. C* 2021, 126, No. 112121.
- (77) Fiedot, M.; Maliszewska, I.; Rac-Rumijowska, O.; Suchorska-Wózniak, P.; Lewńska, A.; Teterycz, H. The Relationship between the Mechanism of Zinc Oxide Crystallization and Its Antimicrobial Properties for the Surface Modification of Surgical Meshes. *Materials* 2017, 10, 353.
- (78) Micochova, P.; Chadha, A.; Hesseloj, T.; Fraternali, F.; Ramsden, J. J.; Gupta, R. K. Rapid Inactivation of SARS-CoV-2 by Titanium Dioxide Surface Coating. *Wellcome Open Res.* 2021, 6, xxx.
- (79) Hewawaduge, C.; Senevirathne, A.; Jawalagatti, V.; Kim, J. W.; Lee, J. H. Copper-Impregnated Three-Layer Mask Efficiently Inactivates SARS-CoV2. *Environ. Res.* 2021, 196, No. 110947.
- (80) Hosseini, M.; Behzadinasab, S.; Chin, A. W. H.; Poon, L. L. M.; Ducker, W. A. Reduction of Infectivity of SARS-CoV-2 by Zinc Oxide Coatings. *ACS Biomater. Sci. Eng.* 2021, 7, 5022–5027.

Capítulo 4

Conclusões

- Compósitos de semicondutores a base de prata com PP foram desenvolvidos e otimizados pela primeira vez;
- Método de co-precipitação se mostrou eficiente para preparar rapidamente os semicondutores de Ag_3PO_4 , $\alpha\text{-Ag}_2\text{WO}_4$, $\beta\text{-Ag}_2\text{MoO}_4$ e Ag_2CrO_4 ;
- As quantidades de 0,5, 1 e 3% em peso de semicondutor em PP foram avaliadas, concluindo que a maior concentração possui mais potencialidades nas aplicações contra patógenos;
- Este composto tem a propriedade físico-química de oxidar bactérias (*S. aureus* e *E. coli*), fungos (*C. albicans*) e vírus SARS-CoV-2 por contato com a superfície.
- Os processos de adsorção de moléculas de H_2O e O_2 na superfície mais ativa do Ag_3PO_4 (110) foram modelados através de cálculos ab initio para explicar os primeiros eventos da formação do radical hidroxila $\bullet\text{OH}$ e do ânion do radical superóxido $\bullet\text{O}^{2-}$ como espécies reativas na atividade biocida, estes resultados levam a formação um passo importante para os entendimentos desses fenômenos na oxidação de patógenos nas superfícies dos semicondutores.

Capítulo 5

Perspectivas Futuras

Como produto desta pesquisa, propõe-se a confecção de compósito poliméricos para a produção de superfícies biocidas seguros, que podem ser aplicadas em equipamentos de proteção individual (EPI), embalagens para alimentos, tecidos (como máscaras e aventais), e outros dispositivos economicamente viáveis para lutar contra o aumento de pandemias virais e riscos fatais associados a vírus, bactérias e fungos

Apêndice A

Supplementary Information for “Bioactive Ag₃PO₄/Polypropylene Composites for Inactivation of SARS-CoV-2 and Other Important Public Health Pathogens”

SUPPORTING INFORMATION

A.1 Characterizations

The AP, PP and PP/AP composites were structurally characterized in a Rigaku X-ray diffractometer, model DMax2500PC. The equipment was operated at 40 kV and 150 mA using Cu-K α radiation ($\lambda = 1.5406 \text{ \AA}$) for the measurements. A scan rate of $2^\circ/\text{min}$ was used in the range of 10 to 80° . The powder diffractograms were compared with the diffraction patterns according to the JCPDS (Joint Committee on Powder Diffraction Standards) and ICSD (Inorganic Crystal Structure Database) crystallographic sheets. Raman spectroscopy was used as a complementary technique to XRD as it is more sensitive to changes in local parameters. The Raman spectroscopic data were obtained on an RFS/100/S Bruker FT-Raman device. Analysis by optical spectroscopy in the regions of ultraviolet and visible radiation (UV-Vis) is a very important topic for studying optical absorption bands. The UV-Vis

characterizations were performed on Cary equipment, model 5G, by the total diffuse reflectance method using an integrating sphere. SEM images were collected on a cold-field emission scanning electron microscope (FE-SEM; JEOL model 7500F) with the following operating conditions: accelerating voltage of 2 kV, emission current of 10 μ A, secondary electron image (SE) mode and magnification of 10,000x. All samples were placed directly onto carbon conductive tape and then gold-coated prior to SEM analysis. PP blank and all PP/AP nanocomposites were submerged in liquid nitrogen, and cryogenic fracturing was performed for the cross-section analysis of the samples. AFM images were obtained using a Flex-AFM controlled by EasyScan 2 software (Nanosurf, Switzerland) in Contrast Phase mode on active vibration isolation table (model TS-150, Table Stable LTD®). The cantilever used for image acquisition was silicon Tap190G (resonance frequency of 190 kHz, force constant of 48 N/m, Budget Sensors) in the setpoint of 50%. The complex viscosity (η^*), the storage modulus (G') and the loss modulus (G'') were determined in a parallel plate rheometer (Anton Paar MCR 305) as a function of frequency (ω). The tests were performed at 190 °C in oscillatory mode. The parameters used were 25-mm diameter plates and 1-mm gap. The range of frequency used was from 0.1 to 500 rad/s at 1% strain, which proved to be in the linear viscoelastic range according to a prior amplitude sweep test. The analyses allowed an evaluation of the degree of dispersion and interaction between polymers and semiconductors, as well as the determination of the rheological behavior in this regime.

The contact angle analyses were carried out using the method of sessile drop in static mode in a goniometer (Model 260 F4 Series Ramé-hart). A 5- μ L drop of distilled water was deposited on the surface of each sample, and the angle formed between the drop and the polymer surface was determined by DROPimage Advanced software. The analyses were performed in triplicate and the data were treated using harmonic media.

A.2. Evaluation of Bactericidal and Fungicidal Activity

Samples of *Escherichia coli* ATCC 25922, *Staphylococcus aureus* ATCC 29213 and *Candida albicans* ATCC 10231 from one or two over-night grown colonies from Mueller-Hinton (MH2) agar plates were suspended in a test tube containing Mueller-Hinton Broth. For the standardization of the inoculum, colonies were transferred to 0.9% saline until reaching 0.5 on the McFarland scale. The turbidity (expressed as optical density; OD) was obtained on a spectrophotometer ($\lambda = 620$ nm), representing approximately 1.5×10^8 CFU. From this solution, a 1:10 dilution in 0.9% saline was performed so that the initial test inoculum was 1.0×10^7 CFU/ml. A suspension-immersed sterilized cotton swab was applied to the entire surface of the Mueller-Hinton agar plates and a 4-mm diameter circle of the specimens was applied on top of the cultures, ensuring direct interaction with the agar and the culture itself. After the incubation of the samples at 37 °C for 48 h, the inhibition zones around the discs were measured and calculated. All tests were performed with five replicates.

Subsequently, the evaluation of the antimicrobial activity of the pure polymer and the composite with Ag_3PO_4 was carried out according to the standard test methodology described in ISO 21702 (Measurement of antibacterial activity on plastics and other non-porous surfaces). A volume of 100 μL of the microbial solution (in a concentration of 10^7 CFU/ml) was inoculated in triplicate on the surface of the samples and covered with a sterile plastic film to ensure its homogenic distribution through the tested area. Samples were incubated at 37 °C for 8 tested times: 4, 8, 16, 32, 64, 128, 256 and 512 min. After the completion of each time, the inoculum was recovered with 10 mL of SCDLP broth followed by serial dilution in PBS buffer. Each dilution was placed in Mueller-Hinton agar and incubated at 37 °C for 24 h. The CFU/cell amount was determined after the incubation time. All tests were performed with five replicates and three occasions

A.3. Evaluation of Antiviral Activity

The specimens (in triplicate) were subjected to immersion and/or spraying of fluid containing SARS-CoV-2 in the concentrations of 26500 copies/mL, 2650 copies/mL, 265 copies/mL and 26.5 copies/mL, seeking to mimic a real model. Then, the samples were incubated under temperature and humidity conditions similar to the environmental ones (25 °C, approximate humidity of 60 to 80%) for up to 8 h in intervals of 2 h (2, 4, 6 and 8 h). After the incubation period, each sample of each triplicate was carefully divided into two new samples: one for the detection of SARS-CoV-2 genetic material by RT-

qPCR (described in step B) and the other for carrying out plaque assay (described in step C) to determine the number of infectious viral particles. The portions of the specimens intended to detect viral genetic material were carefully transferred to 1.5-mL microtubes followed by RNA extraction using the Bio Gene DNA/RNA Extraction kit (Bioclin, Brazil), according to the manufacturer's recommendations. The RT-qPCR reactions for SARS-CoV-2 were performed in triplicate, and the averages obtained were used to determine the amount of viral RNA remaining in each specimen. RT-qPCR was performed for the E gene, as described in the SARS-CoV-2 detection protocol from the Institute of Virology at the Charite University, Berlin. To specify the amount of infectious viral particles, the plaque assay technique, widely used for virus cultivation, was employed using the Vero cell line. The portions of the specimens that were destined for this purpose were submerged and homogenized in physiological solution to release the viral particles and keep them in suspension. Afterwards, a serial dilution of each sample was performed at: 1:10, 1: 100, 1: 1000, 1: 10000; 1: 100000 and 1: 1000000. Each dilution was used to infect the monolayer of Vero cells previously grown in a culture dish. The test was performed in triplicate. After 1 hour of infection, the supernatant was removed and the culture medium suitable for plaque assay was added and incubated under optimal culture conditions. After 7 days, the plates were stained and fixed to count the halos of cell death and determine the number of infectious SARS-CoV-2 virus particles based on the dilution factor.

A.4. Computational methods

All DFT calculations were carried out using the Vienna Ab initio Simulation Package (VASP)^[1,2]. The exchange and correlation effects were treated within the generalized gradient approximation (GGA) by using the Perdew–Burke–Ernzerhof (PBE) functional^[3]. An on-site Coulomb repulsion term (Hubbard U)^[4] was added to treat the Ag d states ($U = 16.01$ eV) and O p states ($U = 10.93$ eV). The dispersion interactions were taken into account by applying the Grimme D3 approximation^[5,6].

The projector augmented-wave method (PAW) was employed to model the effect of the core electrons. The valence electrons were explicitly treated as $4d^{10}5s^1$ (Ag), $3s^23p^3$ (P) and $2s^22p^4$ (O) with a plane-wave basis set expansion converged using a kinetic energy cutoff of 550 eV. All geometry optimizations were converged using a residual force threshold of 0.005 eV/Å. The Gaussian smearing method was applied with a smearing width of 0.01 eV, and Gamma-centered Monkhorst-Pack k-meshes of (5x5x5) and (3x6x1) were used to sample the reciprocal space for the bulk and slab calculations, respectively.

We adopted the slab model to describe the (110) surface with a vacuum of 15 Å along the z-axis. A dipole correction along the z-axis was added to counter any spurious interactions between the periodic images, since the slab created had asymmetric terminations. The slab model was large enough (96 atoms), having a surface area of 102.66 Å² to avoid lateral interactions between molecules in neighboring periodic cells and a thickness of ~12.3 Å to model the bulk effect adequately.

For the water adsorption, three superficial silver atoms were considered potential sites due to their electronic charge deficiency identified through the Bader analysis. One relaxed water molecule was brought to a distance of 3 Å from each site. Thus, the molecule and the two topmost surface layers were allowed to relax freely, with the remaining layers being kept fixed to represent the bulk effect.

The relaxed adsorption system and the isolated molecule were subjected to an electronic density topological analysis following the quantum theory of atoms in molecules (QTAIM)^[7]. The bonding critical points (BCP) between two bonded atoms could then be identified, and the values of electron density (ρ) and its second derivative (Laplacian, $\nabla^2\rho$) at these points could provide valuable insights into the nature and strength of the bond. In the case of the free molecule, its covalent bonds were characterized by a high negative Laplacian (-56 a.u.) and a positive density value (2.45 a.u.) at both BCPs between oxygen and hydrogen atoms. After adsorption on the (110) facet, the same BCPs were assessed (**Figure A.1**). A significant weakening of the covalent bond between the oxygen and the hydrogen closer to the surface was verified, pointing to a drastic drop in the Laplacian and density values to -24 a.u. and 1.59 a.u., respectively, whereas the other covalent bond of the molecule remained unaffected.

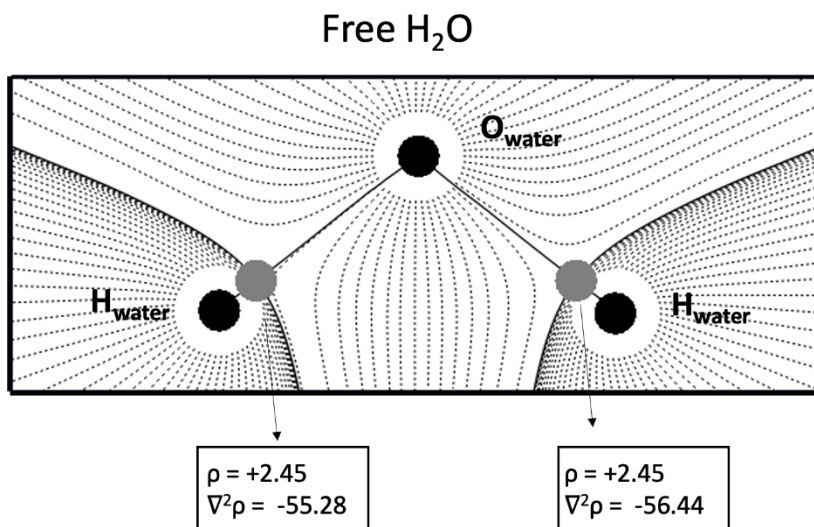


Figure A.1. Topological electronic density analysis of free H₂O molecule. Values of electron density (ρ) and Laplacian ($\nabla^2\rho$) in atomic units at the Bond Critical Points (BCPs) are reported. Contour lines are represented by dashed lines and gradient field by solid lines.

The Ag-O interaction between the water molecule and the surface was characterized as Van der Waals-type since its hallmark on this analysis is a positive Laplacian (+8.63 a.u.) with a low electron density value at the BCP (+0.62 a.u.)^[7]. Interestingly, the molecule also bonded to the surface through a hydrogen-oxygen link, being considered weakly covalent (with density and Laplacian values at the BCP of 0.76 and -0.23 a.u., respectively) (**Figures A.2-A.3**).

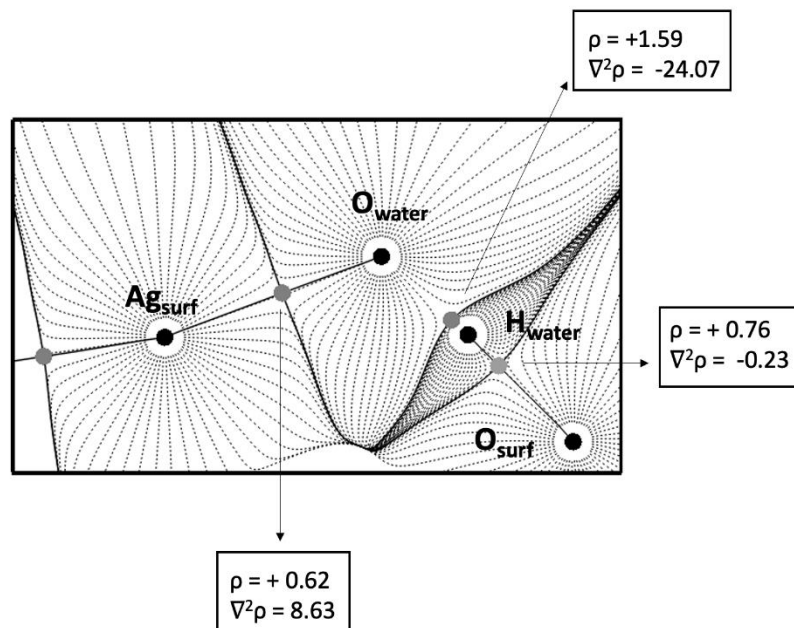


Figure A.2. Topological electronic density analysis of the interaction between the H₂O molecule and a surface Ag atom. Values of electron density (ρ) and Laplacian ($\nabla^2\rho$) in atomic units at the Bond Critical Points (BCPs) are reported. Contour lines are represented by dashed lines and gradient field by solid lines.

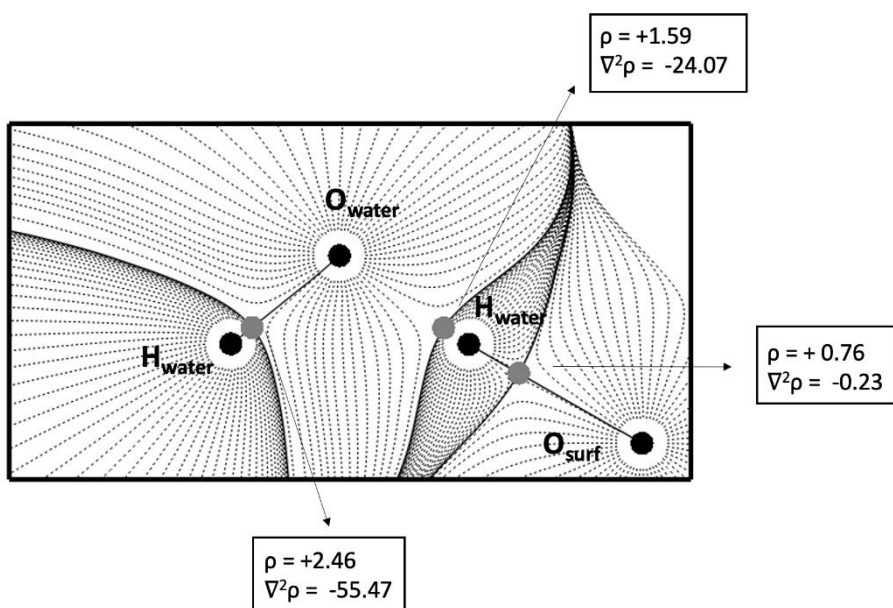


Figure A.3. Topological electronic density analysis of the interaction between the H₂O molecule and a surface O atom. Values of electron density (ρ) and

Laplacian ($\nabla^2\rho$) in atomic units at the Bond Critical Points (BCPs) are reported. Contour lines are represented by dashed lines and gradient field by solid lines.

Ab initio molecular dynamics (AIMD) simulations in the NVT ensemble were performed at low temperatures (10 and 50 K). The relaxed adsorption system was equilibrated for 750 fs, and the simulations were extended until 900 fs. To lower the computational cost, the slab was reduced and only the molecule and the first three layers were allowed to move along the simulations, keeping all other atoms fixed to represent the bulk.

A.5. Structural Analysis

The XRD patterns of the AP and PP samples and the PP/AP composites are shown in **Figure A.4**. **Figure A.4A** exhibits the diffraction peaks characteristic of AP at 20.9, 29.8, 33.4, 36.7, 42.7, 52.9, 55.0, 57.5, 61.9 and 63.9° attributed to the (110), (200), (210), (211), (310), (222), (320), (321), (400), and (411) diffraction planes, respectively, according to ISCD No. 14000.⁴⁰ These diffraction peaks show that the phase can be indexed to the cubic symmetry in which the bulk lattice is composed of regular [PO₄] and distorted [AgO₄] tetrahedral clusters.^{47,48} The X-ray diffraction peaks for the PP sample (**Figure A.4B**) identified at 14.24, 16.92, 18.58 and 21.42° can be attributed to the (110), (040), (130) and (131)+(041) diffraction planes, respectively⁴⁹. The corresponding (130) plane indicates the alpha phase of the PP since

polymorphism is a common phenomenon in crystalline polymers.^{49–51} In the alpha phase, the crystalline structure is characteristic of the monoclinic unit cell.⁵² The diffraction peaks of the PP/AP composites (0.5, 1 and 3%) are shown in **Figures A.4C-E**, respectively. The formation of the PP/AP composites is evidenced by the appearance of the most intense peaks of the AP due to the increase in the AP concentration in the PP matrix. It is possible to observe that the alpha structure of the PP was maintained, as well as the structure of the crystals of the AP, suggesting success in the formation of the PP/AP composites.

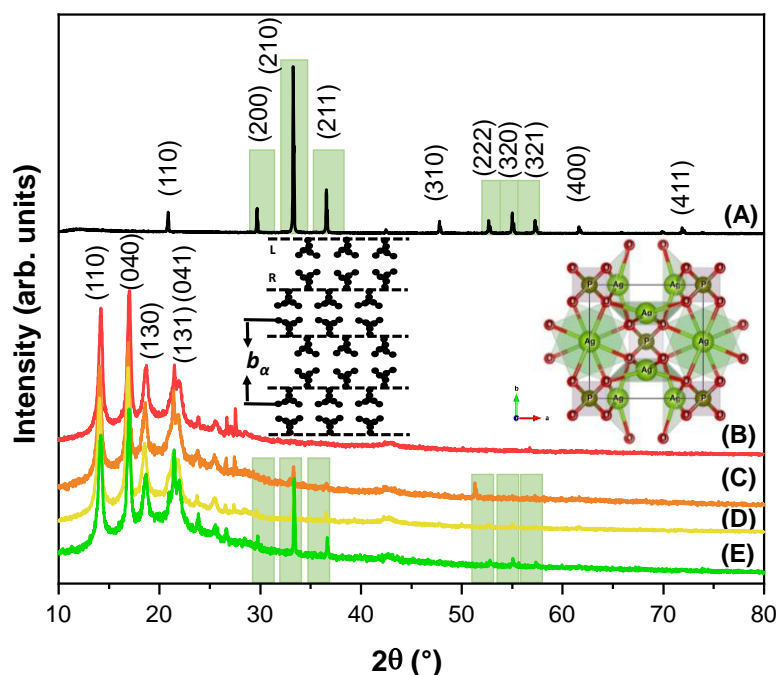


Figure A.4. X-ray diffractograms of (A) AP, (B) PP, (C) PP/05AP, (D) PP/1AP and (E) PP/3AP samples.

Micro-Raman measurements were performed to analyze the degree of order at the short range of the samples (see **Figures A.5A-E**). For the AP

crystals, it is possible to observe in the Raman spectrum a band at 908 cm^{-1} attributable to the symmetrical $(\text{PO}_4)^{3-}$ (A_1) stretching vibrations.³² For the PP matrix, the Raman spectrum indicates several peaks in two different regions. The first one, located between 800 and 1500 cm^{-1} , peaks around 1439 - 1457 cm^{-1} and can be assigned to vibration modes of CH_2 deformation groups. The peaks observed at approximately ~ 808 and $\sim 840\text{ cm}^{-1}$ reveal asymmetric stretching of CH_2 of the PP monomer, while that at 972 cm^{-1} is attributed to CH_3 vibrations. On the other hand, in the second region the vibration modes observed between 2700 and 3000 cm^{-1} are related to the CH_2 bending vibrations of the PP structure.⁵³⁻⁵⁶ Even though modes referring to the AP crystals in the PP/AP samples cannot be observed, it is possible to identify a small change in the intensity of the band at 972 cm^{-1} in the PP/1AP and PP/3AP samples, indicating the formation of the composite.

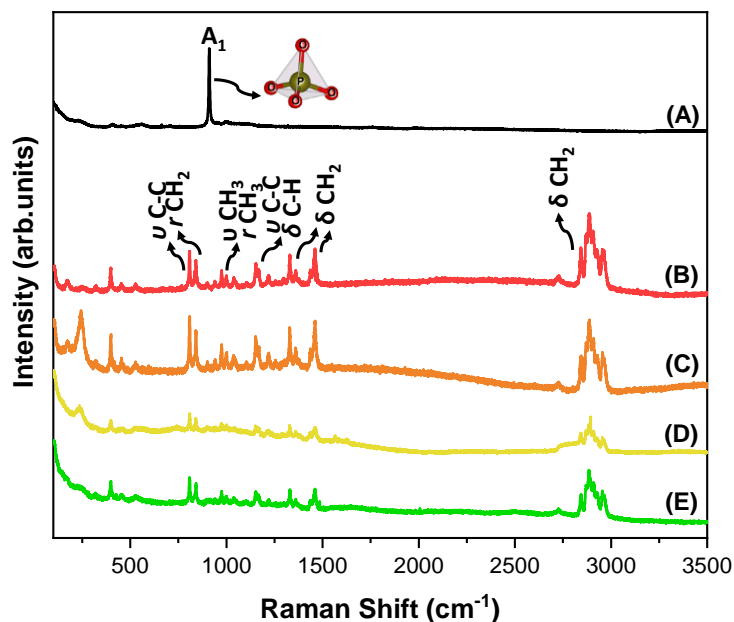


Figure A.5. Micro-Raman spectra of (A) AP, (B) PP, (C) PP/05AP, (D) PP/1AP and (E) PP/3AP samples.

The samples were characterized by FTIR to analyze the interactions between the PP and the AP, as expressed in **Figures A.6A-E**. The peaks around ~ 3350 , ~ 2941 and ~ 2722 cm^{-1} correspond to O-H stretching and CH_2 vibrations characteristic of asymmetric and symmetrical stretching of CH_3 , respectively.⁵⁷ The peaks around ~ 2350 and ~ 1670 cm^{-1} can be assigned to the C-O stretching vibration,⁵⁸ while those at ~ 2941 and ~ 2856 cm^{-1} are due to asymmetric and symmetrical stretching vibrations of CH_2 , in the main chain of the PP. The peak at ~ 1460 cm^{-1} is related to asymmetric deformations of CH_3 and shear vibrations of CH_2 . The peak at ~ 1369 cm^{-1} is due to vibrations of symmetrical deformation of CH_3 .^{54,59} The peak at ~ 1167 cm^{-1} can be attributed to the asymmetric stretching of C-C, asymmetric vibration of CH_3 and C-H vibrations,

while that at $\sim 990\text{ cm}^{-1}$ is due to vibrations of asymmetric balance of CH_3 . The peak at $\sim 977\text{ cm}^{-1}$ can be assigned to the asymmetric rocking of CH_3 and asymmetric stretching vibrations of C-C, whereas that at 466 cm^{-1} is related to the asymmetric rocking of CH_3 and asymmetric stretching vibrations of C-C.^{52,60} In the PP/AP composites, a difference in the peak located at 990 cm^{-1} can be seen, which widens as the percentage of AP increases in the PP matrix. This widening indicates the overlapping of the absorption band of the $[\text{PO}_4]$ clusters that occurs around at $\sim 1000\text{ cm}^{-1}$.^{32,61} However, the most notable difference between the PP and the PP/AP composite spectra can be seen at 530 cm^{-1} , which can be attributed to the vibrations of P-O bonds. These changes reveal the interaction between the PP at short and long ranges and the AP particles.

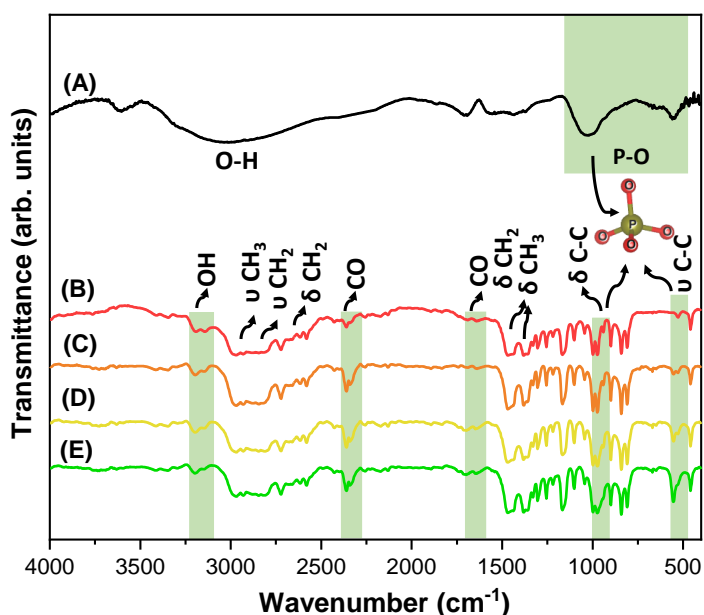


Figure A.6. FTIR spectra of (A) AP, (B) PP, (C) PP/05AP, (D) PP/1AP and (E) PP/3AP samples.

The AFM images in **Figure A.7** were obtained in tapping mode and exhibit changes in the topography after the modification of the polymer matrix with the addition of AP. The presence of AP on the surface of the polymer matrix is evidenced by the circular microparticles shown in **Figures A.7B-D**. However, both the dispersion of these microparticles and their size are not uniform, which could be the result of the agglomeration of nanoparticles during the mixing process within the polymer. The PP/05AP sample exhibits domains without detection of AP microparticles, while PP/1AP shows well dispersed microparticles but larger than in the other samples. Lastly, the PP/3AP sample presents the best dispersion of AP microparticles and fewer domains of agglomeration. These features are in agreement with the SEM images discussed below. Although the root mean square (rms) indicates changes in topography, a tendency in the rms and an increase in the AP mass added can be observed. The rms observed for PP, PP/05AP, PP/1AP and PP/3AP samples was 6.9, 15.3, 58.6 and 18.8 to, respectively. However, these changes in size and dispersion of microparticles seem not to change the optical properties of the sample on a large scale.

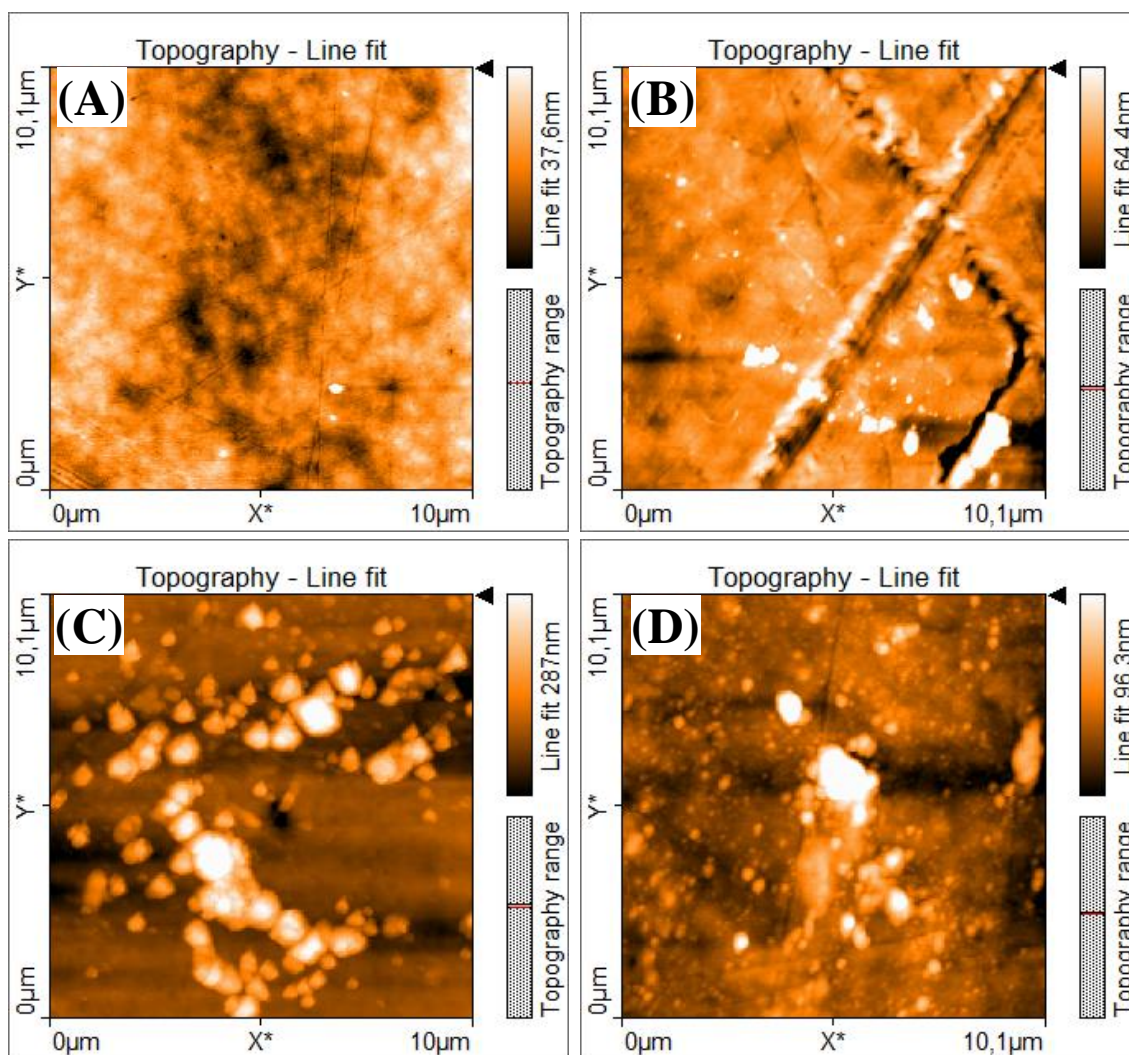


Figure A.7. AFM images of the (A) PP, (B) PP/05AP, (C) PP/1AP and (D) PP/3AP films.

The UV-Vis absorption spectra of the samples are shown in **Figure A.8** and indicate the incorporation of AP into the polymer matrix. A decrease in the diffuse reflectance spectra around 350 nm can be noted for the samples containing the polymer (**Figure A.8A**). Such characteristic irradiation absorptions are due to electronic transitions from HOMO to LUMO and are

associated with π - π^* transitions from the carbonyl groups originated by the oxidation of PP.^{62,63} Similar behavior was noticed by Sinha et al.⁶³ after submission of PP samples to gamma radiation and by Lee et al.⁶² after chemical oxidation of PP using Cr(VI) oxide in acetic acid/acetic anhydride solvent. It is worthwhile to note the agreement between the presence of absorption in 350 nm in the diffuse reflectance spectroscopy and the presence of CO stretching vibrations in the FTIR spectra (**Figure A.8**). The AP sample shows an absorption around 525 nm, which is expected for the BCC phase of Ag_3PO_4 .^{32,64-66} The band gap energy (E_g) of the samples was experimentally estimated by extrapolating the linear portion of the Tauc plot curves considering the background light scattering and an indirect allowed transition (**Figure A.8B**). The E_g calculated for the AP was 2.38 eV, while for the PP (the energy difference between HOMO and LUMO) this value was 3.55 eV. The E_g of the AP agrees with those reported by Wu et al.⁶⁴ and Yi et al.²⁹ After incorporation of AP into the polymer matrix, two band gaps can be observed for the films: one ascribed to the π - π^* transition of PP and another attributed to the presence of AP, which becomes more evident as the concentration of the latter increases. The E_g measured for the PP/05AP, PP/1AP and PP/3AP samples is shown in **Table SA.1**, where no significant deviation of the estimated values was observed when compared to the E_g for the same group of absorption.

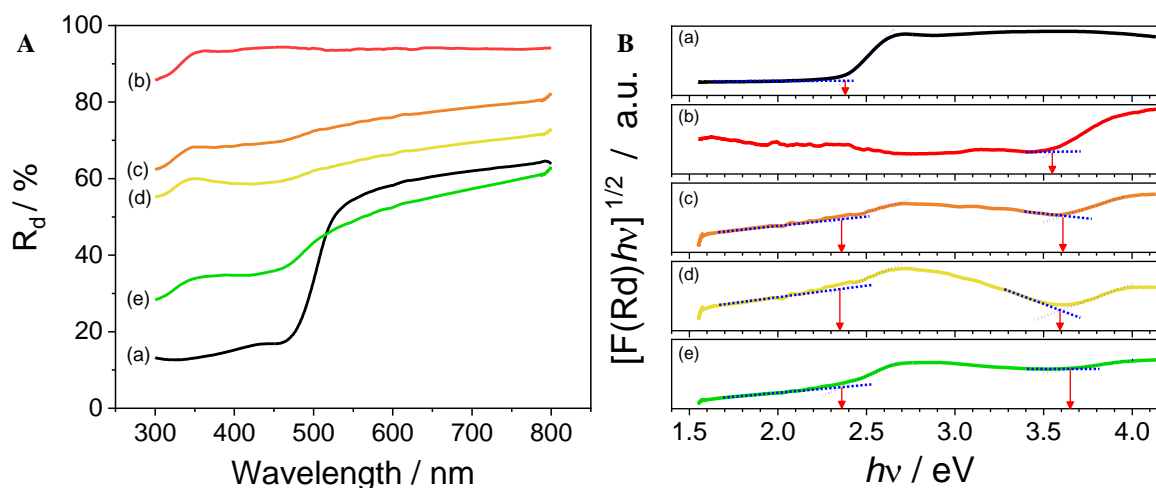


Figure A.8. (A) Diffuse reflectance spectrum and (B) Tauc plot for the (a) AP, (b) PP, (c) PP/05AP, (d) PP/1AP and (e) PP/3AP samples considering indirect allowed transition. The arrows indicate the band gap energy.

Table A.1 – Experimental band gap values for the samples.

Sample	<i>E_g</i> assigned to AP absorption (eV)	<i>E_g</i> assigned to PP absorption (eV)
AP	2.38	-
PP	-	3.55
PP/05AP	2.36	3.61
PP/1AP	2.35	3.59
PP/3AP	2.36	3.65

Figure A.9 shows the inhibition halos for *S. aureus* (Gram +), *E. coli* (Gram -) and *C. albicans* (fungi). It is observed that for *S.aureus* (**Figure A.9A**) the PP and PP/05AP samples do not present inhibition zones, and the PP/1AP and PP/3AP samples obtain inhibition zones of 0.6 and 0.9 cm respectively. For *E. coli* (**Figure A.9B**) only pure PP does not present a halo of inhibition, whereas for samples PP/05AP, PP/1AP and PP/3AP we obtain the inhibition

halos of 0.5, 0.7 and 0.9 cm respectively. For *C. albicans* (**Figure A.9C**) a similar result to *S. aureus* is obtained, with inhibition halos of 0.6 and 0.9 cm for the PP/1AP and PP/3AP samples, respectively. Thus, it is observed that the greater the concentration of AP within the PP matrix, the greater the halo of inhibition obtained.

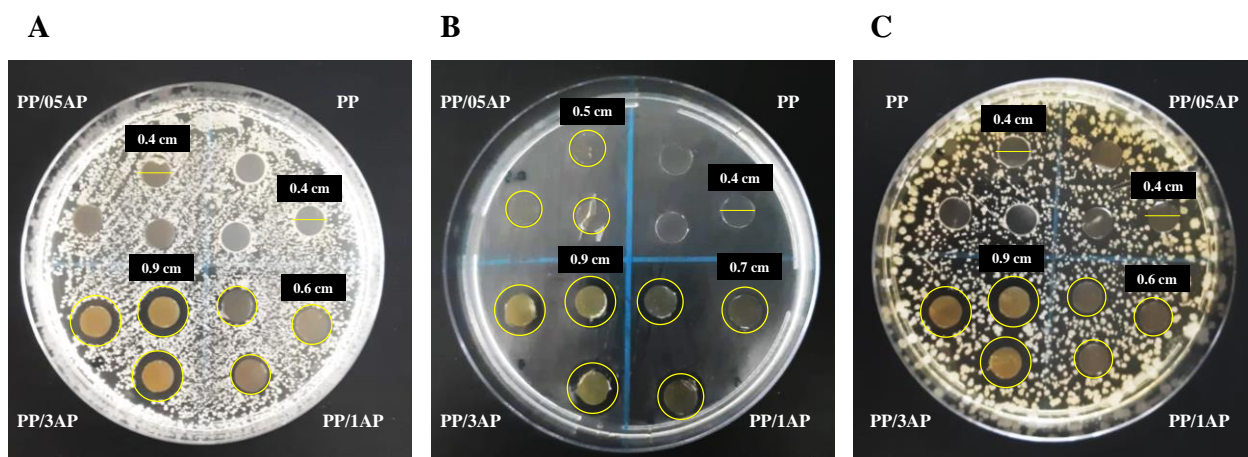


Figure A.9. Halo of inhibition tests for the microorganisms A) *S. aureus*, B) *E. coli*, and C) *C. albicans*.

A.6. References

- [1] G. Kresse, J. Furthmüller, *Comput. Mater. Sci.* **1996**, 6, 15.
- [2] G. Kresse, J. Furthmüller, *Phys. Rev. B - Condens. Matter Mater. Phys.* **1996**, 54, 11169.
- [3] J. P. Perdew, *Int. J. Quantum Chem.* **1985**, 28, 497.
- [4] B. Himmetoglu, A. Floris, S. De Gironcoli, M. Cococcioni, *Int. J. Quantum Chem.* **2014**, 114, 14.
- [5] S. Grimme, *J. Comput. Chem.* **2006**, 27, 1787.
- [6] S. Grimme, J. Antony, S. Ehrlich, H. Krieg, *J. Chem. Phys.* **2010**, 132, 154104.
- [7] P. S. V. Kumar, V. Raghavendra, V. Subramanian, **2016**, 128, 1527.

Apêndice B

Supplementary Information for “Polypropylene modified with Ag-based semiconductors as potential material against SARS-CoV-2 and other pathogens”

SUPPORTING INFORMATION

B.1. Synthesis of Ag-based Semiconductors

Silver Tungstate (α -Ag₂WO₄), Silver Molybdate (β -Ag₂MoO₄) and Silver Chromite (Ag₂CrO₄) was synthesized by the coprecipitation (CP) method (CP) in an aqueous medium at room temperature. Two solutions were made, adding 1×10^{-3} mol of the lattice former salt (Na₂WO₄·2H₂O (Sigma-Aldrich, 99.8%), Na₂MoO₄·2H₂O (Alfa-Aesar, 99%) and K₂CrO₄ (Alfa-Aesar, 99.9%)) to 50.0 ml of distilled water and 2×10^{-3} mol of AgNO₃ (Cenabras, 99.8%) to 50.0 ml of distilled water. Both solutions were kept at 70°C under constant stirring. The AgNO₃ solution was added to lattice former salt solution, then a precipitate appeared. The precipitate obtained was washed several times with distilled water and dried in an oven at 60 ° C for 12h.

B.2. Characterizations of Semiconductors/PP Composite Materials

These composite materials were characterized by using X-Ray Diffraction (XRD), Fourier Transform Infrared Spectroscopy (FTIR), absorption spectroscopy in the regions of Ultraviolet and Visible (UV-Vis) and contact angle. To XRD analysis a Rigaku X-ray diffractometer, model DMax2500PC. The equipment will be operated in the conditions of 40 kV and 150 mA, the radiation used for the measurements will be that of Cu-K α ($\lambda = 1.5406 \text{ \AA}$). A scan rate of $2^\circ/\text{min}$ were used in the range of 10° to 80° . The diffractograms were compared with the diffraction patterns according to the JCPDS (Joint Committee on Powder Diffraction Standards) and ICSD (Inorganic Crystal Structure Database) crystallographic sheets. FTIR was performed using a Jasco FT/IR-6200 (Japan) spectrophotometer operated in absorbance mode at room temperature in the range of $470\text{-}4000 \text{ cm}^{-1}$. After, analysis by UV-Vis were performed on a Cary equipment, model 5G by the method of total diffuse reflectance using an integrating sphere. Shortly thereafter, the composites were characterization by the AFM images. The characterization was obtained using a Flex-AFM controlled by Easyscan 2 software (Nanosurf, Switzerland) in Contrast Phase mode on active vibration isolation table (model TS-150, Table Stable LTD®). The cantilever used for image acquisition was silicon Tap190G (Resonant frequency 190 kHz, force constant 48 N/m, Budget Sensors) in setpoint of 50%. To finalize the structural surface characterizations, contact angle analyses were carried out using the method of sessile drop in static mode in a goniometer (Model 260 F4 Series Ramé-hart). On the surface of each sample, a $5\mu\text{L}$ drop of distilled water was deposited, and the angle formed between the drop and the polymer surface was determined by DROPimage Advanced software. The analyses were performed in triplicate and data were treated using harmonic media. The rheological behavior of composites, as well as the degree of dispersion and the interaction between PP and semiconductor

oxides, were evaluated by measures of complex viscosity (η^*) as a function of frequency (ω). in a parallel plate rheometer (Anton Paar MCR 305), The measurements were carried out at 190 °C, in oscillatory mode, using a 25 mm diameter plates, 1 mm gap and a frequency range of 0.1 to 500 rad/s. The deformation used was 1%, as it is in the linear viscoelastic range, defined according to a previous amplitude sweep test. Stress-strain curves were obtained in the EMIC DL3000 equipment with a load cell of 20N and a strain rate of 2.5×10^{-4} mm/min. The test was based on ASTM D 638: 2014 and rectangular samples, in film form, with approximate dimensions of 30x5 mm and approximate thickness of 0.13 mm were used. Differential scanning calorimetry (DSC) was performed in a DSC 203 F3-Maia (Netzsch) on samples of 5–10 mg under the following thermal programming: heating from -70°C to 200°C at a rate of 10°C/min. The degree of crystallinity of PP was calculated from melting enthalpy (ΔH_m), using Equation 1, where ϕ is the mass fraction of the Ag-based semiconductor (0, 0.5, 1, or 3 wt%) and ΔH_m^0 is the melting enthalpy for hypothetically 100% crystalline PP, equal to 207 J/g.

$$\%C = \frac{\Delta H_m}{(100 - \phi)\Delta H_m^0} \times 100$$

B.3. Evaluation of Microbicidal Activity

Samples of *Escherichia coli* ATCC 25922, *Staphylococcus aureus* ATCC 29213 and *Candida albicans* ATCC 10231 from one- or two-over-night grown colonies from Mueller-Hinton (MH2) agar plates were suspended in a test tube containing Mueller-Hinton Broth. For the standardization of the inoculum, colonies were transferred to 0.9% saline until reaching 0.5 on the Mc Farland scale. The turbidity (expressed as optical density; OD) was obtained in a

spectrophotometer ($\lambda = 620 \text{ nm}$), which represents approximately 1.5×10^8 CFU. From this solution, a 1:10 dilution in 0.9% saline was performed so that the initial test inoculum is 1.0×10^7 CFU/mL.

The antimicrobial activity of the pure polymer and the semiconductors/PP composites was carried according to the standard test methodology described in ISO 21702 - Measurement of antibacterial activity on plastics and other non-porous surfaces.^[1] A 100 μ L volume of the microbial solution (in a concentration of 10^7 CFU/ml) was inoculated in triplicate on the surface of the samples (2x2 cm) and covered with a sterile plastic film to ensure its distribution through the tested area. Samples were incubated at 37°C for 8 tested times: 1, 2, 4, 8, 16 and 24 h. After each completed time, the inoculum was recovered with 10 mL of SCDLP broth followed serial dilution in PBS buffer. Each dilution was plated in Mueller-Hinton agar and incubated at 37 °C for 24 h. The CFU/cell amount was determined after the incubation.

The semiconductors/PP composites were analyzed to determine the inactivation capacity of SARS-CoV-2 particles, according to ISO 21702:2019.^[2] The virucidal test was carried out to evaluate the potential of the treated material to inactivate viral particles, preventing them from infecting the host cells arranged on the plate (Vero ATCC ® CCL-81™). The tests were performed in three independent biological replicas, each containing a technical triplicate. Samples with standardized dimensions of 2x2 cm are individually placed in Petri dishes. The material is exposed to the viral solution, where the SARS-CoV-2 viral solution is added so that it meets the entire surface area of the material, after this contact, it is incubated for 10 minutes, then neutralized and diluted in series. The viral titer is then measured using the infectious Tissue culture dose50 (TCID₅₀) methodology. The reduction of SARS-CoV-2 particles was quantified after 10 minutes of contact of the plastic film samples (with the presence of semiconductors) and the plastic film sample without treatment. It is noteworthy that the results are expressed in comparison of the virucidal action against the reduction of viral particles from the SARS-CoV-2 stock solution with

a "non-virucidal" material (white/control) and the "active" material (treated), so that it is possible to calculate the percentage of viral inactivation, represented by Log₁₀ of TCID₅₀ reduction.

In this experiment we would also see if the material to be tested loses its efficiency after 5 times of use. For this, the same sample unit was tested equally five times, on the same surface. Having as an interval a sterilization procedure with 70% alcohol, mili-Q water and drying. This procedure occurs for all analyzed components, whether internal controls or different samples. To evaluate the cytopathic effect, analyzes are performed using an inverted microscope after an incubation period of 72 hours in an oven at 37 °C with 5% CO₂. In this way, visual confirmation of the cytopathic effect of the SARS-CoV-2 strains in relation to the Vero ATCC ® CCL-81™ cell is obtained. The interpretation is based on the method of Spearman & Karber^[3] and the viral titer quantification data obtained in the incubation process were applied to the limit-dilution methodology (end-point-dilution), in which the inoculation of successive decreasing dilutions in viral suspension applied to the cells is evaluated, thus, possible to identify the cytopathic effect in 50% of the inoculated cultures. Also, a correction factor related to the volume of virus dilution (SARS-CoV-2) used in each TCID₅₀ assay was applied.^[4] The result of virucidal efficacy is negative when there is visualization of cytopathic effects and positive when there is no cytopathic effect. To determine the viral inhibition index, the logarithmic difference between the control group and the group with treatments is used.

B.4. Optical Analyses of Semiconductors/PP Composite Materials

The UV-Vis-NIR diffuse reflectance of the pristine PP, silver-based ternary oxides, and PP modified with Ag-based ternary oxide are shown in Figure S1. In the Figure S1A and S1B, the samples containing the fillers of wide band gap do not exhibit clearly absorptions due to the presence of the additives α -Ag₂WO₄ and β -Ag₂MoO₄, respectively, but there are significant changes in the total diffuse reflectance of incident radiation and in the color of the samples (Table S1). On the other hand, the incorporation of the filler is evident to Ag₂CrO₄ (Figure S3C) PP modification, which show absorptions near to band gap of the pristine metal oxide. Furthermore, the band absorptions at 1200, 1400, and 1730 nm are characteristic of the 2nd overtone, 1st overtone combination, and 1st overtone due to the C-H single bond vibration absorption^[5], which is in agreement with the literature.^[6] The highest decrease in the total diffuse reflectance is observed in the samples containing 3% of fillers, in which are observed changes in the absorption attributed to the 2nd overtone and 1st overtone combination for C-H single bond vibration. It is believed that is due to the change in the chain structure of the polymer. Only the PP samples modified with β -Ag₂MoO₄ keep their structure.

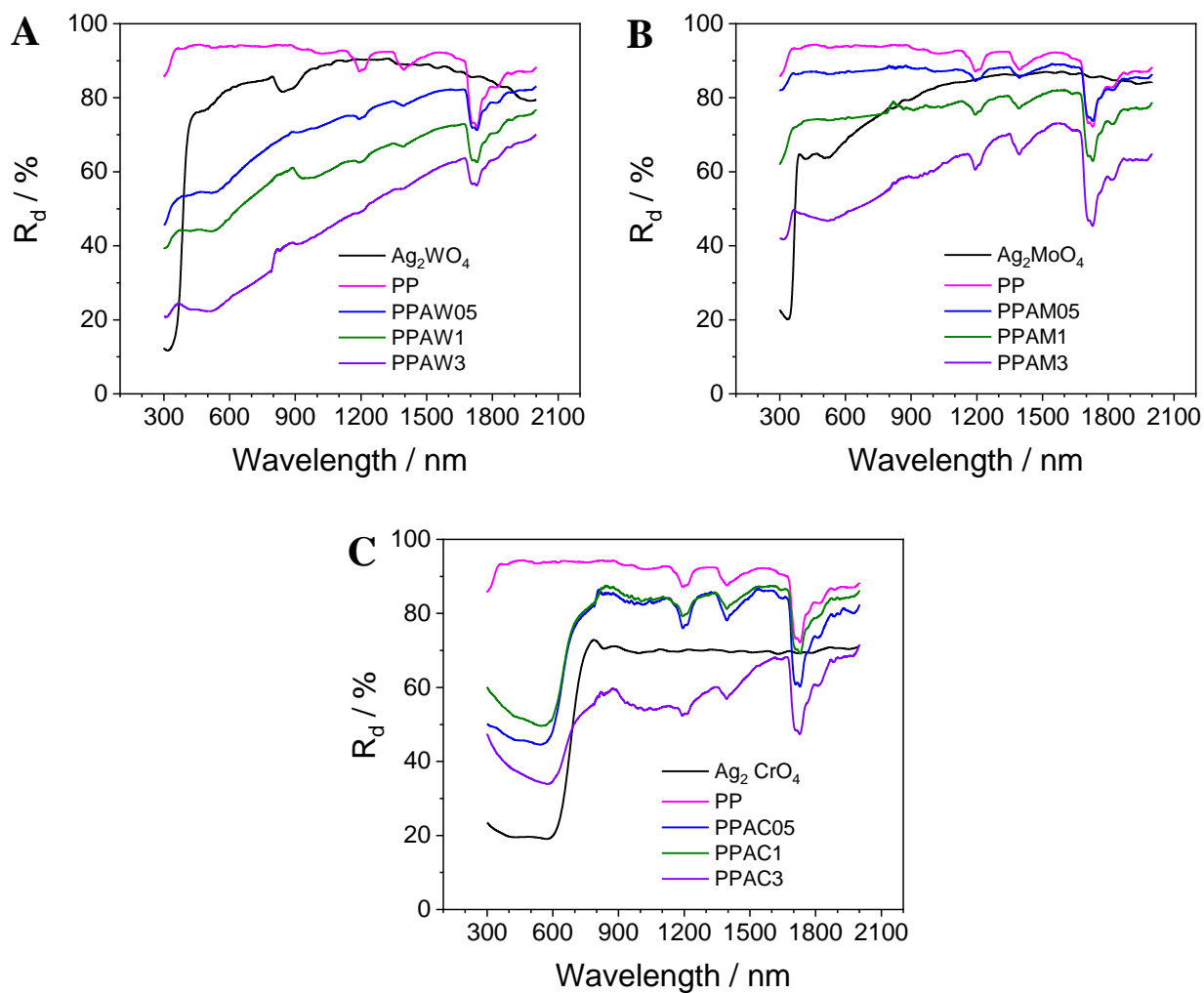
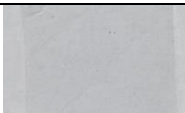






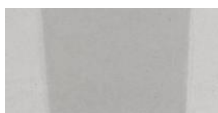
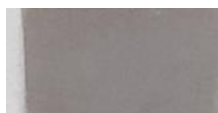






Figure B.1. Diffuse reflectance spectrum to the silver based ternary oxides, pristine PP and PP modified with (A) α - Ag_2WO_4 , (B) β - Ag_2MoO_4 , and (C) Ag_2CrO_4 .

Table B.1. Digital images for the PP, PPAW, PPAM and PPAC samples.

Composite	% Added to the polymer (in weight)			
	Pristine	0.5%	1.0%	3.0%
PP				
α -Ag ₂ WO ₄				
β -Ag ₂ MoO ₄				
Ag ₂ CrO ₄				

The radiation absorptions observed in the ultraviolet-visible spectrum can be ascribed to the transitions from HOMO to LUMO of polymer and from the valence to the conduction bands of the silver-based ternary oxides. In the Figure S1 it is observed that the polymer matrix shows a decrease in the total diffuse reflectance spectrum around 350 nm, which is associated with π - π^* transitions from the carbonyl groups originated by oxidation of PP.^[7,8] Further, the pristine silver-based ternary oxides display absorptions around 410, 380, and 740 to α -Ag₂WO₄, β -Ag₂MoO₄, and Ag₂CrO₄, respectively. The band gap energies (E_g) were experimentally estimated by extrapolating the linear portion of the Tauc plot curves, which are shown in Table S2 (The Tauc plots are shown in the Figure S2). Although the pristine α -Ag₂WO₄ and β -Ag₂MoO₄ have E_g

smaller than the transition HOMO-LUMO of the polymer, the modified PP samples with these materials' present values of E_g near to transition observed for pure PP. It can be associated with the indirect transition behavior of the mechanism of excitation of these metal oxides,^[9] which could bring a superposition of the interband transition of the metal oxide with the HOMO-LUMO transition of the polymer. In this way, the Tauc plot curve show just one transition. However, as the percentage of metal oxides increases in the polymer matrix, the bandgap decreases trending to the value of pristine metal oxides. Regarding the PP modified with Ag_2CrO_4 , the E_g values were similar to the metal oxides.^[9] In this latter case, the narrow E_g of the metal oxide does not overlap with the HOMO-LUMO transition of the PP, which allows the clear observation of the changes in the Tauc plot. It is noteworthy to mention that the values of the E_g estimated for the pristine metal oxide are in agreement with those reported in the literature.^[9]

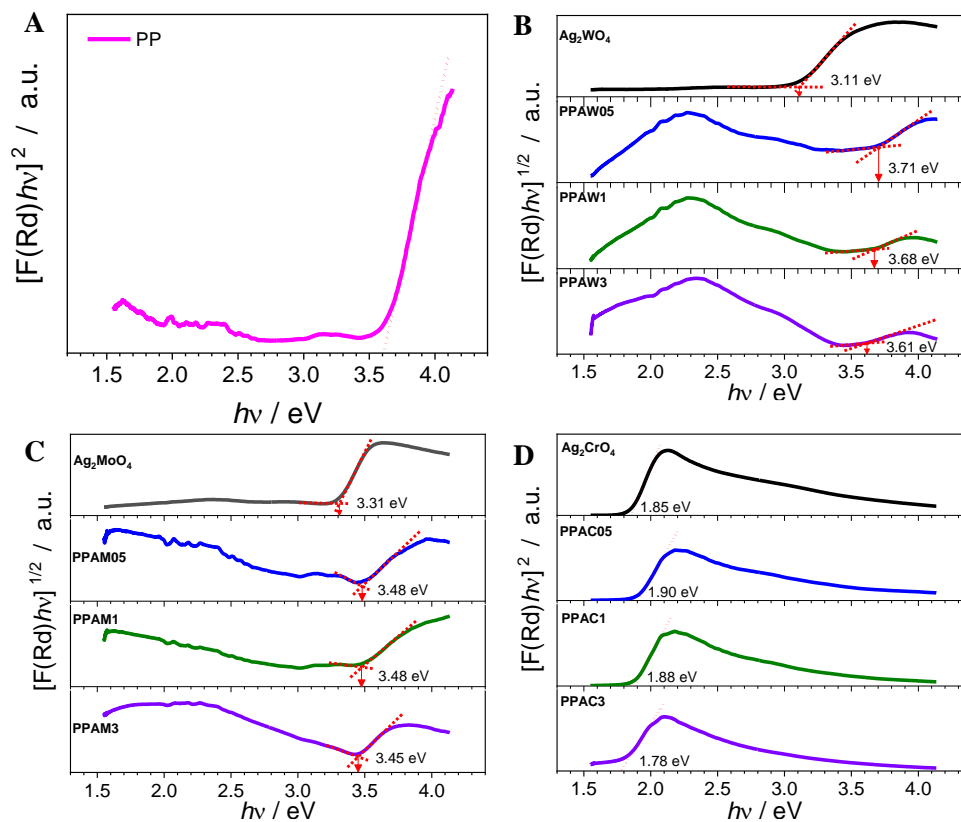


Figure B.2. Tauc plot to the (A) PP, (B) PPAW, (C) PPAM, and (D) PPAC. The arrows indicate the band gap energy in the materials with indirect band gap, while the band gap for direct transitions is the linear extrapolation crossing the X axis.

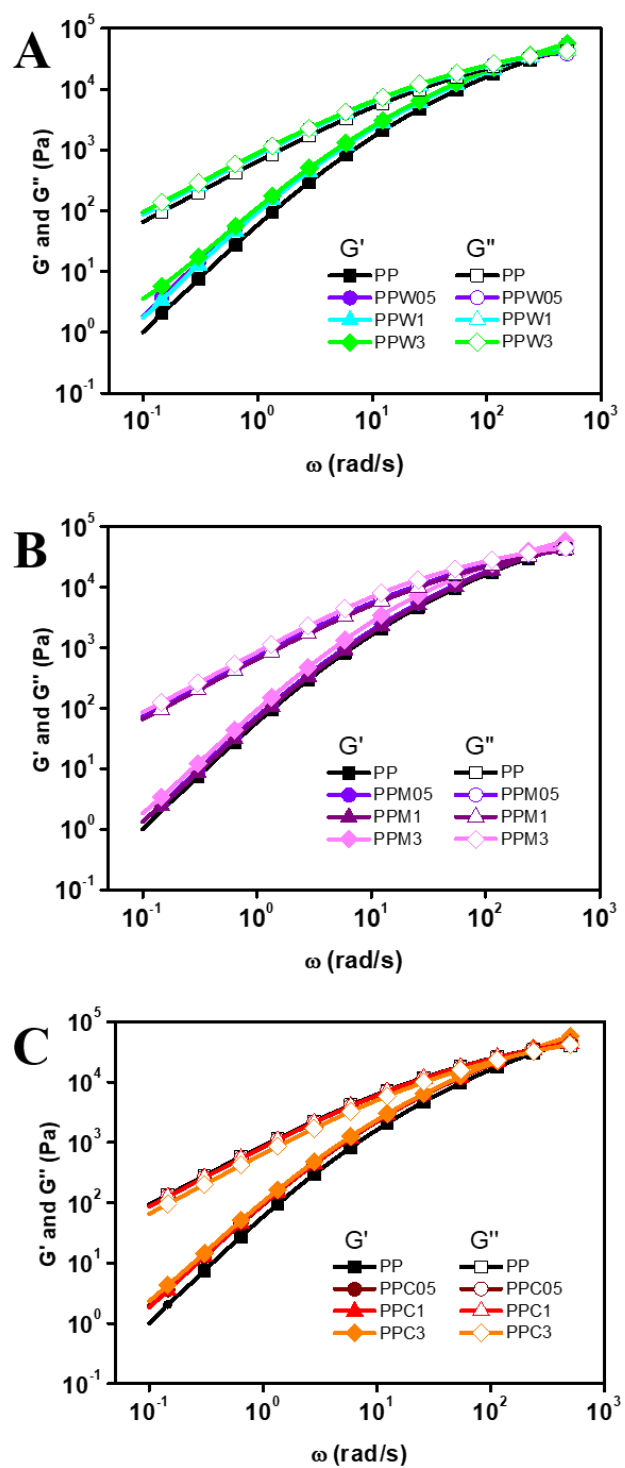


Figure B.3. Storage (G') and loss modulus (G'') of PPAW (A), PPAM (B) and PPAC (C) samples at 190° C as a function of frequency.

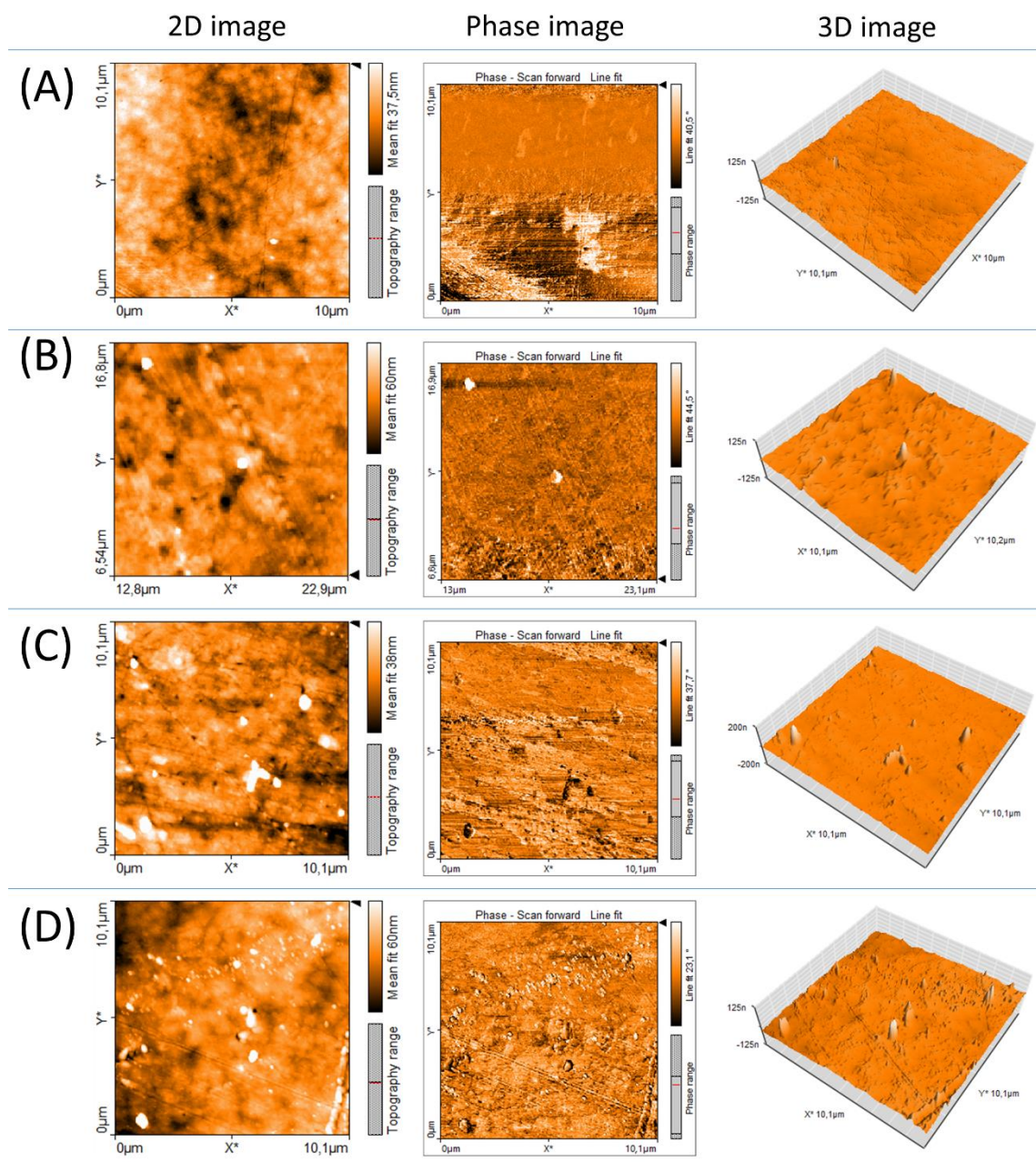


Figure B.4. AFM images of the (A) PP and PPAW containing (B) 0.5, (C) 1.0, and (D) 3.0% wt. of the α - Ag_2WO_4 .

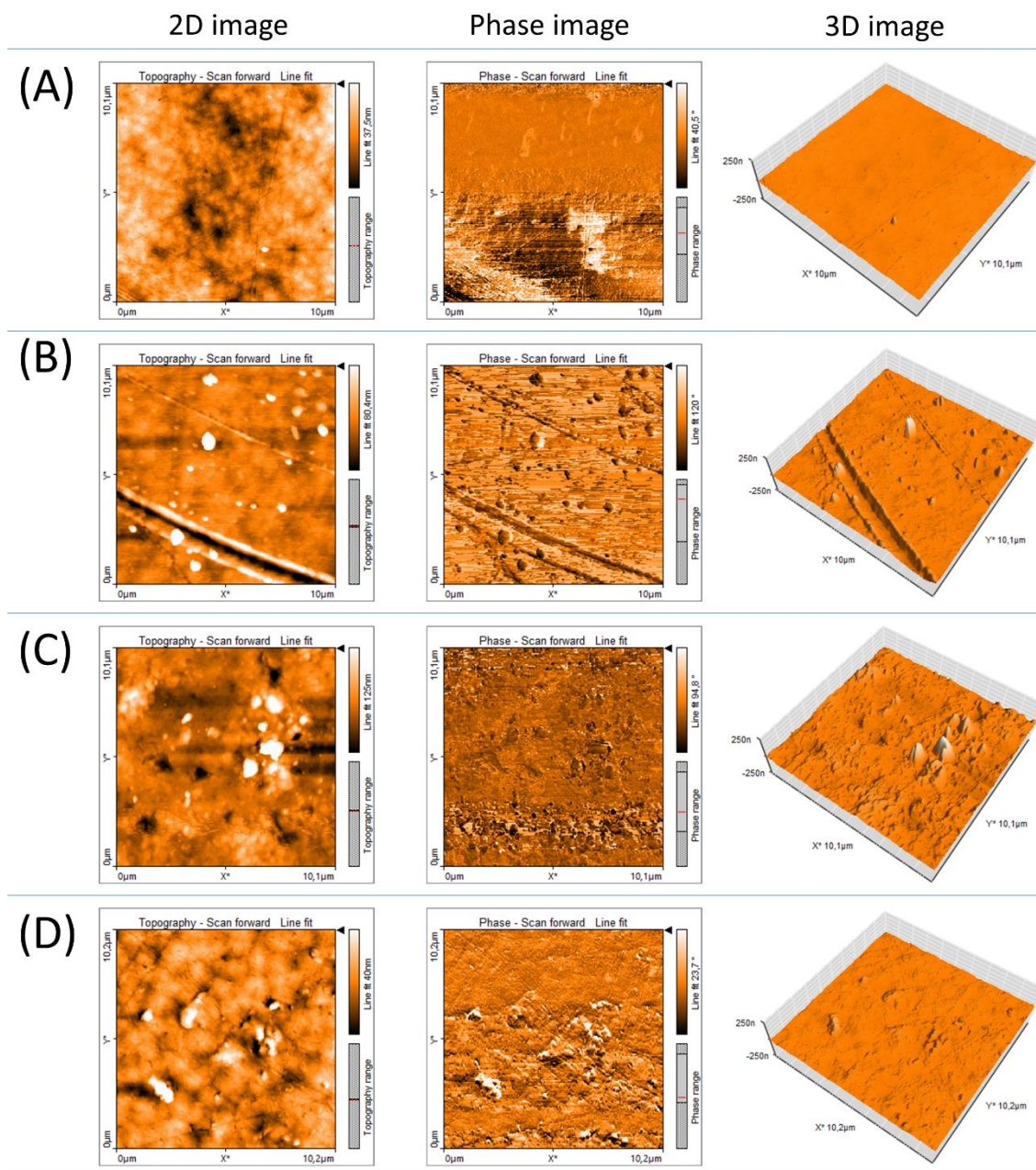


Figure B.5. AFM images of the (A) PP and PPAM containing (B) 0.5, (C) 1.0, and (D) 3.0% wt. of the β - Ag_2MoO_4 .

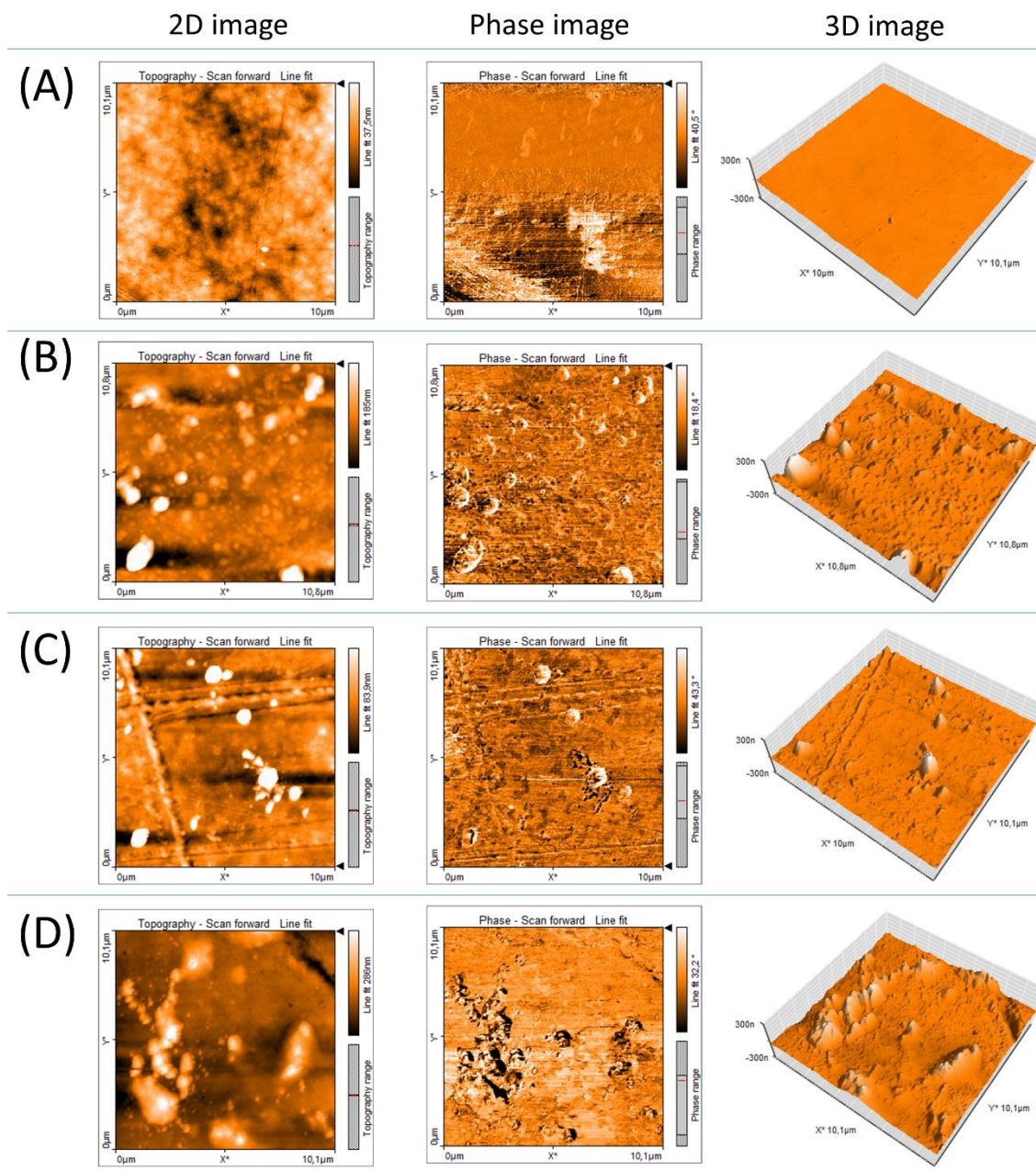


Figure B.6. AFM images of the (A) PP and PPAC containing (B) 0.5, (C) 1.0, and (D) 3.0% wt. of the Ag_2CrO_4 .

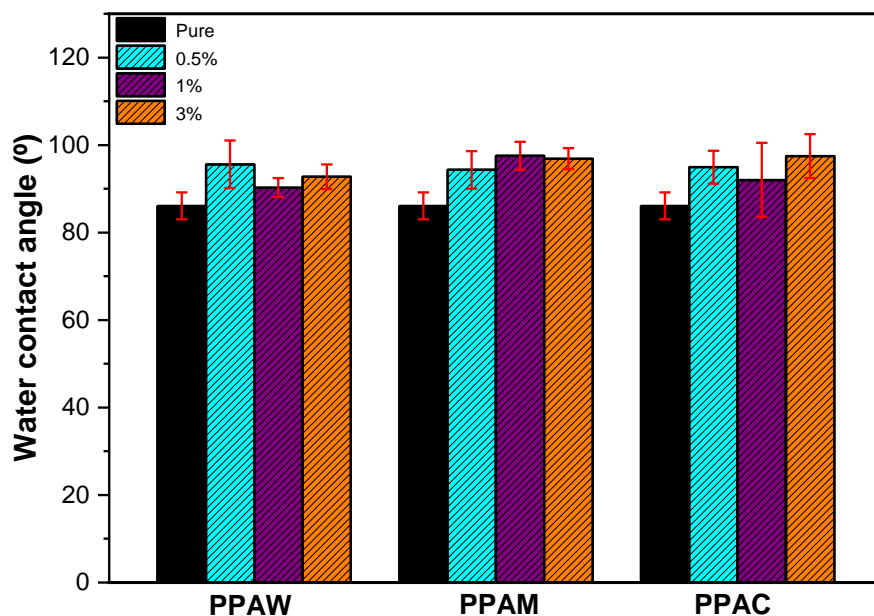


Figure B.7. Contact angle result of PPAW, PPAM and PPAC and their oxide concentrations 0% (PP pristine), 0.5%, 1% and 3%.

B.5. References

- [1] ISO. ISO 22196 - Measurement of antibacterial activity on plastics and other non-porous surfaces; ISO: Geneva, Switzerland, 2019.
- [2] ISO. ISO 21702:2019 - Measurement of antiviral activity on plastics and other non-porous surfaces; ISO: Geneva, Switzerland, 2019.
- [3] J. Miller, R. Ulrich. *Method. Percept. Psycho-phys.* 2001, 63 (8), 1399.
- [4] L. J. Reed, H Muench. *Am. J. Epidemiol.* 1938, 27 (3), 493.
- [5] N. Heigl, C. H. Petter, M. Rainer, M. Najam-ul-Haq, R. M. Vallant, R. Bakry, G. K. Bonn, C. W. Huck. *J. Near Infrared Spectrosc.* 2007, 15 (5), 269.
- [6] J. Kruenate, R. Tongpool, T. Panyathanmaporn; P. Kongrat, *Surf. Interface Anal.* 2004, 36 (8), 1044.
- [7] D. Sinha, T. Swu, S. P. Tripathy, R. Mishra, K. K. Dwivedi. *Radiat. Eff. Defects Solids* 2003, 158 (7), 531.